ULTRA-SMALL NANOCRYSTALS: SYNTHESIS, OPTICAL AND MAGNETIC PROPERTIES, ORIENTED ATTACHMENT, AND FILM ASSEMBLY

By

Weidong He

Dissertation

Submitted to the Faculty of the

Graduate School of Vanderbilt University

in partial fulfillment of the requirements

for the degree of

DOCTOR OF PHILOSOPHY

in

Interdisciplinary Materials Science

May, 2012

Nashville, Tennessee

Approved:

Professor James H. Dickerson

Professor Timothy P. Hanusa

Professor Kalman Varga

Professor Jason G. Valentine

Dedicated

to

My parents, Ms. Jiying Lou and Mr. Yuhou He,

and to my family members

for their support and inspiration to me throughout my life

ACKNOWLEDGEMENT

First, I am grateful to Professor James H. Dickerson, my advisor for providing me the opportunity to work in the exciting interdisciplinary area combining nanomaterials, optics, magnetism, and electrochemisitry. His patient guidance and inspiring encouragement have been invaluable sources facilitating all the fulfillments throughout my Ph.D. research period. I thank him for his insight and advice on my academic writing and career development, without which I would not have been so creative and productive in these years. I am grateful for his support for me to conduct research in national labs and present our research in renowned conferences.

I like to express my gratitude towards my co-advisor Professor Timothy P. Hanusa for his guidance and encouragement at various stages of my Ph.D. work. Without his input and support, the project would not have been so smooth, and the completion of the dissertation would not have been possible.

I am grateful to the other members of my Ph.D. committee: Professor Kalman Varga, and Professor Jason G. Valentine for their guidance and time during the development of the work.

I thank Dr. Ju-Hyun Park and Dr. Stephen A. McGill for their help and discussion during my stay at National High Magnetic Field Laboratory.

Special thanks go to my colleagues: Dr. Suseela Somarajan, Dr. Isabel Juan, Junhao Lin, Max E. Osmulski, and Alex Krejci for their assistance in the day-to-day laboratory activities, and Dr. Dmitry S. Koktysh, Dr. Tony Hmelo, and Dr. Bo Kyoung Choi for their help and trainings.

I thank Mrs. Sarah Ross-Satterwhite, Interdisciplinary Materials Science Program Coordinator, for her assistant and kind help during my work.

Lastly, I express my earnest thanks to my parents, my wife, and my sisters. Their support and belief in me have made my graduate studies in USA smooth and productive.

TABLE OF CONTENTS

LIST OF FIGURES

LIST OF SCHEMES

LIST OF TABLES

CHAPTER 1

INTRODUCTION

1.1 Overview

Ultra-small nanocrystals (NCs) are nanoscale materials. Since the size of ultra-small UCs is comparable to or even smaller than the Bohr exciton diameter of the materials, ultra-small NCs exhibit significant enhanced physical properties, such as magnetic, optical and electronic properties.[1-2] As the size of a NC becomes smaller quantum effects, increased astoichiometry, and defects can give rise to many interesting property transitions, including a metal to semiconductor transition, and a diamagnetic to ferromagnetic transition.[3-5]

Among interesting optical and magnetic materials, europium compounds are of special interest due to their optical or/and magnetic properties.[6] Europium is a rare earth element. As a metal, Eu is paramagnetic, and is unstable in air. The electronic configuration of Eu is shown in Figure 1.1.[7] Eu has two common oxidation states that form two types of compounds, Eu^{2+} compounds and Eu^{3+} compounds. Due to the energy transitions of multiple 4f electrons, both Eu^{2+} and Eu^{3+} compounds show optical properties under irradiation of light. Beside optical properties, Eu^{2+} compounds also have magnetic and magneto-optical properties due to the seven unpaired 4f electrons. Europium chalcogenides, are compounds that are composed of europium and group six elements. The spin configuration, and the 4f-4f and 4f-5d electronic transitions of europium compounds make these materials promising candidates for advanced magnetic, optical, and electronic applications.[8-10] Eu^{3+} compounds include Eu_2O_3 and Eu_2O_2S, and both compounds exhibit photoluminescent properties.[11-12]

$$1s^2 2s^2 2p^6 3s^2 3p^6 3d^{10} 4s^2 4p^6 4d^{10} 5s^2 5p^6 4f^7 5d^0 6s^2$$

Figure 1.1: Electronic configuration of europium.[7]

Due to their seven 4f unsaturated electron spins, all the europium monochalcogenides (EuX: X = O, S, Se, Te) are magnetic semiconductors. They have been studied for a number of years due to their optical and magneto-optical properties and for their robust ferromagnetic (FM) and antiferromagnetic (AF) properties, primarily in bulk crystalline form. The materials have potential for applications in optical insulator, optical switch and spintronics areas.[8-10] Among the europium compounds, EuO and EuS are ferromagnets with Curie temperatures (T_c) at 69.3 K and 16.6 K, respectively. EuSe is a metamagnetic semiconductor with a Néel temperature (T_N) at 4.6 K, and EuTe is a classical Heisenberg antiferromagnet with a T_N at 9.6 K. Europium oxysulfide (Eu_2O_2S), a ternary europium chalcogenide, is a diamagnetic insulator with a band gap at 4.4 eV. Eu_2O_2S is known to exhibit high-performance luminescence and exist as promising candidates for oxygen storage, medical imaging, and radiation intensifying screens.[11-12] Table 1.1 shows the physical properties of EuX and Eu_2O_2S.

Table 1.1. Physical properties of EuX

Materials	Magnetic Ordering	Lattice Constant (nm)	Ordering Temperature (K)	Bandgap (eV)
EuO	Ferromagnetic	0.5141	69.3	1.12
EuS	Ferromagnetic	0.5968	16.6	1.65
EuSe	Ferrimagnetic	0.6195	4.6	1.80
EuTe	Antiferromagnetic	0.6598	9.8	2.00

Interest in synthesizing nanoscale europium compounds has grown considerably during the past decade. Some synthetic methods were designed specifically to produce EuX NCs. For example, Stoll, Zhao and Dickerson have reported different synthetic routines of EuX nanoparticles (NPs) in the past few years.[13-16] The synthesis of anisotropic EuX nanostructures has also drawn special attention since EuO nanorods (NRs) were synthesized and showed interesting magnetic as well as optical properties.[17] In particular, the synthetic chemistry as well as the physical properties of EuS NCs were investigated in a number of reports.

Chen W. et al. [18] (2000): Luminescence enhancement of EuS nanoclusters in zeolite.

- Compared to bulk EuS powder, the intensity of photoluminescence was observed from EuS clusters.
- EuS clusters showed size-dependent photoluminescent properties.

Thongchant S. et al.[19] (2003): Liquid-phase synthesis of EuS nanocrystals and their physical properties.

- EuS NCs were synthesized using a colloidal method for first time.
- EuS NCs showed size-dependent magnetic properties.

Thongchant S. et al. [20] (2003): First observation of Faraday effect of EuS nanocrystals in polymer thin films.

- Pronounced Faraday effects were observed from EuS NCs-plastic films.
- Faraday rotation peaks showed blue shift as the size of EuS NCs decreases.

Redigolo M. L. et al.[14] (2006): Magnetization reversal in europium sulfide nanocrystals.

- Magnetic reversal was observed from EuS NCs for the first time.

Zhao F. et al.[16] (2006): Synthesis and size-dependent magnetic properties of monodisperse EuS nanocrystals.

- A facile colloidal method was developed to synthesize highly-monodispersed EuS NCs.
- Obvious blue shifts were observed as the size of EuS NCs reduces.
- Curie temperature decreased with the decrease in the diameter of EuS NCs
- Coercivity-versus-size curves showed maxima.

Redigolo M. L. et al.[21] (2009): Europium sulfide nanoparticles in the sub-2 nm size regime.

- The smallest EuS NCs were synthesized by thermolysis method.

Unlike EuS, the weak chemical bonding between Eu and Te makes EuTe the most unstable europium chalcogenide, and the synthesis of EuTe NCs is much more challenging than that of EuS NCs. Literature has mainly focused on the magnetic and optical properties of bulk EuTe crystals or epitaxial EuTe films.

I. N. Goncharenk. et al.[22] (1998): Ferromagnetic interactions in EuS and EuSe studied by neutron diffraction at pressures up to 20.5 GPa.

- The lattice parameters of EuS, EuSe and EuTe crystals were varied by applying high pressure.
- The ordering temperatures of EuTe were studied by neutron diffraction.
- A new model on the correlation between magnetic exchange constants and band gaps was proposed and analyzed for EuTe.

W. Heiss. et al.[23] (2001): Giant tunability of exciton photoluminescence emission in antiferromagnetic EuTe.

- Two dominant excitonic photoluminescence peaks were measured at low temperatures for epitaxial antiferromagnetic EuTe films.
- The peaks were efficiently shifted by varying the applied magnetic field at 1.7 K.

H. Kepa. et al.[24] (2003): Magnetic interactions in EuTe epitaxial layers and EuTe/PbTe superlattices.

- The magnetic properties of EuTe films and EuTe/PbTe superlattices were studied by magnetization and neutron-diffraction measurements.
- The Néel temperature of EuTe layers was changed by changing the film thickness and the strain state of EuTe crystal.
- A mean-field model was applied to analyze the enhanced Néel temperature as observed.

N.S. Gaikwad. et al.[25] (2003): Substrate dependent properties of electrodeposited EuTe thin films.

- EuTe thin films were obtained by electrodeposition technique.

- The structural and morphological properties of as-deposited EuTe films were found to be substrate-dependent.

E. Schierle. et al.[26] (2008): Antiferromagnetic order with atomic layer resolution in EuTe(111) films.

- Individual atomic layers of epitaxial antiferromagnetic EuTe nano-films were made and the temperature dependences of the magnetizations of EuTe films were studied.
- The Néel temperature of EuTe thin films in EuTe/PbTe heterostructure was enhanced to 12.8 K from the bulk value 9.8 K by a 5.0 % compressive strain.

B. Diaz. et al.[27] (2010): Growth of EuTe islands on SnTe by molecular beam epitaxy.

- EuTe nano-islands were grown on SnTe by molecular beam epitaxy and a relaxation of EuTe lattice parameter was observed as EuTe grew thicker.
- A model was applied to analyze the formation mechanism of distortions caused by EuTe islands on SnTe.

W. Söllinger. et al.[28] (2010): Exchange interactions in europium monochalcogenide magnetic semiconductors and their dependence on hydrostatic strain.

- Hydrostatic pressure experiments were conducted to obtain bulk EuO, EuS, EuSe and EuTe single crystals with different compressive lattice strains.
- The correlation between nearest-neighbor and next-nearest-neighbor exchange constants and the lattice constants was analyzed.
- Mathematical models were applied to analyze the strain-induced change in the ordering temperatures of EuTe crystal.

A. B. Henriques. et al.[29] (2011): Zero-phonon emission and magnetic polaron parameters in EuTe.

- A zero-phonon emission structure of 1 μm epitaxial EuTe films was discovered and analyzed by photoluminescence measurements.

The reports on EuS were mainly on the synthesis and size-dependent properties of EuS quantum dots. The optical and magnetic properties of the EuS NCs were found to be closely correlated with their size according to these reports. In these reports, anisotropic EuS NCs were not achieved, and synthetic method of 1D EuS NCs is still lacking. Synthetic routes, such as colloidal syntheses that yield 1D EuS NCs, are highly-favorable because two-dimensionally confined NCs typically show interesting physical properties dramatically different from those of quantum dots and bulk materials.[30-32] Due to the lack of a synthetic route to EuTe quantum dots, most of the work on EuTe had been on the magnetic and optical properties of EuTe films and bulk crystals. The photoluminescent properties and magnetization were shown to be variable by changing the thickness and surface strain and Néel temperature enhancement was obtained by introducing 2D compressive lattice strains in EuTe films.[26] A facile route to EuTe quantum dots will allow us to explore the size-dependent optical, magnetic, and magneto-optical properties of this classical antiferromagnetic material at the nanoscale, and more importantly enable us to study the correlation between Néel temperature and 3D lattice strain in EuTe crystals.

As a Eu^{3+} compound, Eu_2O_2S exhibits high-performance room-temperature photoluminescence properties in visible wavelengths. To explore the correlation between shape and optical properties, europium oxysulfide nanoparticles, nanoplates, and nanowires, were recently synthesized using different colloidal methods.[33-35] Size-dependent photoluminescent properties were observed from the synthesized nanostructures. However, little size control was achieved in the synthesis by using these synthetic methods. To improve the size-dependent optical properties of europium oxysulfide NCs, a colloidal synthetic route with precise size control is highly favorable.

To develop facile colloidal routes to synthesize EuTe, EuS and Eu_2O_2S NCs, we need to understand the growth mechanism of colloidal synthesis. There are two steps in crystal growth of NCs: nucleation and growth.[36] In a colloidal synthesis, nucleation occurs at the initial stage of a reaction, where precursors are decomposed and very small objects start to form as nuclei for further growth.[37] The size of nuclei is typically no larger than 2 nm. Once nuclei are present in a colloidal system, they will grow larger by diffusion of precursors and surface reaction on their surface. This step is called growth. The synthesis of monodispersed NCs requires appropriate precursors, solvent, surfactants and reaction temperatures.[1, 37]

In colloidal chemistry, a precursor is a material that reacts in a chemical reaction to produce a target material. For example, in a typical EuS nanoparticle synthesis, europium oleate is used as precursor to provide Eu source. The selection of precursors is crucial to a NP synthesis since different precursors have different reactivities, giving rise to different activation energies for a synthesis.[38] If a precursor has a small decomposition activation energy, nucleation will occur very rapidly, which suppresses the growth stage of nuclei, yielding small NCs. With a large decomposition activation energy, a precursor tends to produce larger NCs.[39] In general, with inorganic precursors a colloidal synthesis tends to own fast growth kinetics, and large size distribution is typically generated by fast growth kinetics. To improve the size distribution of a colloidal synthesis, organic precursors containing resultant elements are employed.[40] The disadvantage of using large organic precursors is that large precursors require high decomposition energy, and, thus, high reactions temperatures are required. The selection of appropriate precursor directly determines whether the synthesis of NCs will occur and whether the synthesis will yield a desired size distribution.[41-42] Before synthesizing a new NC, synthesis of a precursor is often neccessary because such a precursor is often not available for the synthesis of a new nanomaterial. After the synthesis of precursors, the synthetic system has to be designed based on the properties of the new precursor, which requires a careful selection of other parameters associated with the synthesis.

Besides precursors, other important factors have to be taken into consideration in a colloidal synthesis. These important factors include solvents, surfactants and reaction temperatures. In a colloidal synthesis, surfactants are compounds that are used to reduce surface tension between functioning agents in the system in order to facilitate the synthesis.[43] When the synthesis ends, the surfactants can serve as surface ligands, which can then form surface charges by ionization and dissolvation to prevent aggregation and protect the NCs from oxidation if they are reactive in ambient conditions. During the synthesis, the size of NCs is closely related to the amount of surfactants used. Addition of some surfactants can reduce the size of as-synthesized NCs while addition of others may increase their size. For example, in our previous report on the synthesis of EuS NPs, we found that the size of NPs increased with the amount of phenanthroline that was added as reaction surfactant.[44] Phenanthroline was found to be able to facilitate the aggregation-mediated growth of EuS NPs by its electronegative repulsion with negatively-charged oleate ligands on the surface of the NPs. Figure 1.2 shows the TEM images of EuS NPs with different size distributions achieved by changing the ratio of europium: phenanthroline (E:P) in the synthesis.

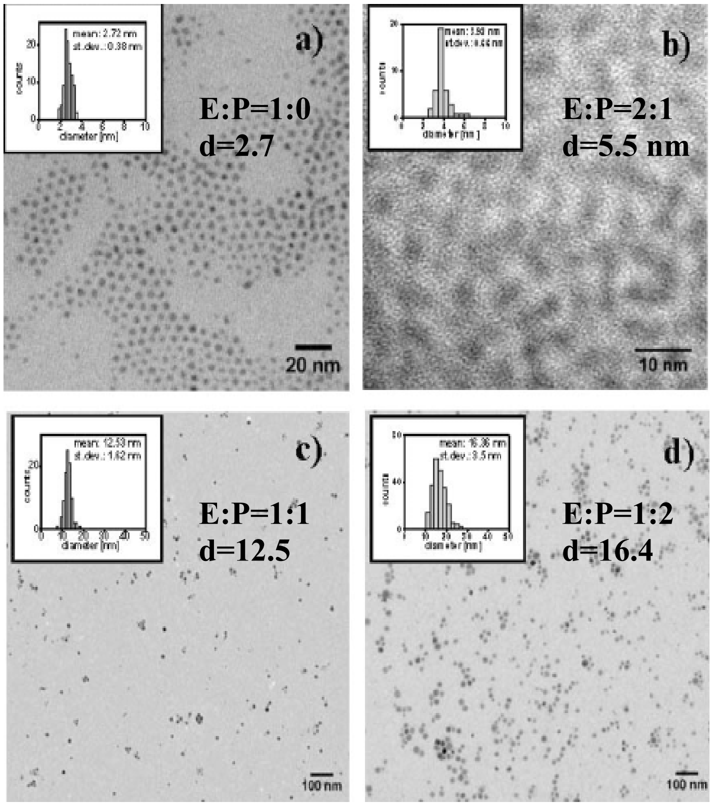

Figure 1.2: HR-TEM images of EuS nanocrystals grown at different synthetic conditions.[44]

As colloidal synthesis becomes an important route to ultra-small NCs, more and more research has been focusing on the development of green chemistry methods to synthesize these NCs.[45-47] The burgeoning interest in novel green synthetic routes in nanocrystal colloidal chemistry have been motivated by employing the materials as building blocks for real-life applications as well as the sense of environment protection.[45] The development of such efficient and environmentally-friendly colloidal synthetic methods has to be based on a pronounced understanding on the growth mechanisms of the NCs. By varying one or more of synthetic conditions, such as reaction temperature, concentration of precursor and solvent, the growth mechanism of NCs can be tuned, typically varying between Oswald ripening (OR) and oriented attachment (OA) mechanisms, which will be introduced in a latter session of this chapter.[48]

Facile colloidal synthesis of ultra-small NCs allows one to explore the interesting optical, magnetic, and electrical properties of these materials with extremely small sizes at the nanoscale. The research on the synthetic chemistry as well as the physical properties of these ultra-small greatly helps to enhance the applicability of these NCs in device applications. A necessary step towards the application of these NCs is their uniform film assembly.[49-51] An efficient film deposition technique greatly facilitates the application of the NCs as building blocks in device fabrication. Among deposition methods, such as spin-coating, Langmuir-Blodgett method, and chemical vapor deposition, electrophoretic deposition (EPD) has been regarded as an efficient route to NC films.[52-54] Compared to other deposition techniques, EPD is a highly efficient assembly technique because of its high rate of deposition, high controllability, scalability, uniform film casting capabilities, and the engendered low surface roughness of the films.[54] Reports have shown the possibility of fabricating functional nanoparticle devices from the casts while maintaining the intrinsic quantum-confined characteristics of NPs.[55] The technique has been widely employed with colloidal NPs and has been demonstrated to be an efficient way to test whether nanocrystals can serve as effective building blocks of device fabrication.[56]

1.2 Electronic structure and optical properties of Eu compounds

As a rare earth element, Eu has sixty-three electrons, fifty-four of which comprise the saturated Xenon configuration, and nine 4f and 6d electrons of which have a configuration of $4f^7 5d^0 6s^2$. In EuX, 6s electrons saturate the p orbitals of X to make Eu a Eu^{2+} cation and a X^{2-} anion.[7] With saturated p orbitals, the valence band of EuX is built up with the p states of X, and the 5d and 6s states form the lower level and higher level of conduction band of EuX. In EuX crystal, the 5d states of Eu are split into two energy levels, i.e., lower energy level $5dt_{2g}$ and higher energy level $5de_g$. The electronic structures of EuX compounds are shown in Figure 1.3. Due to the energy gaps, 4f electrons in the valence band can jump to the conduction band in various paths. Figure 1.3 shows these energy states as the 4f electrons of EuS are excited from the valence band to different energy states of the conduction band.[57]

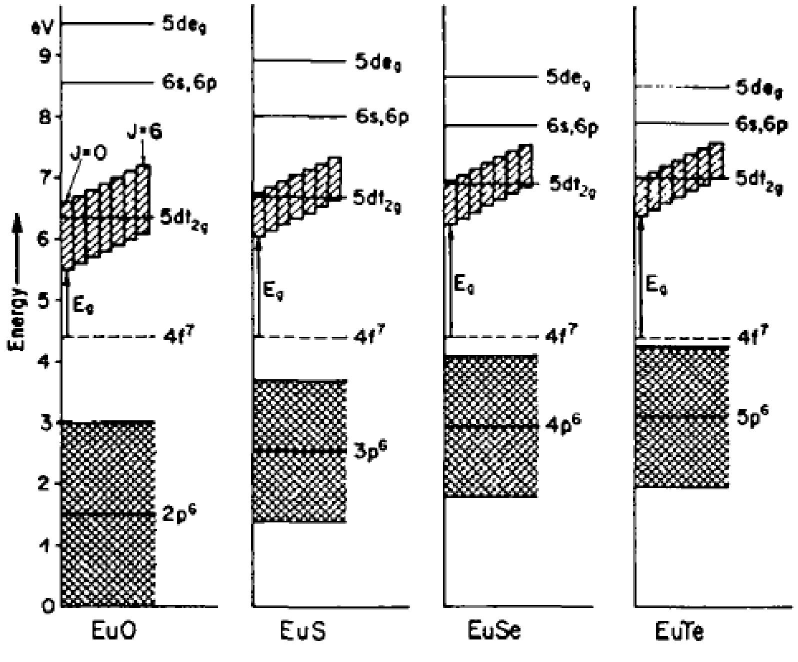

Figure 1.3: Energy states of EuX at room temperature.[57]

EuX are optically active because their seven 4f electrons have different transitions upon excitation of incident light. Despite their different band gaps, all four EuX materials have two kinds of absorption peaks, as shown in Figure 1.4: low-energy peaks corresponding to $^4f_7(^8S_{7/2})–^4f_6(^7F_J)5d(t_{2g})$ transition of europium electrons, and high-energy peaks corresponding to from 4f levels to 5d states.[57] The correlation between band gaps and optical properties of EuX has been studied both theoretically and experimentally in the literature. The optical properties of EuX can be tuned by size due to quantum confinement leading the change in the band gaps of EuX. That is because in general, the band gap of a NC increases as its size decreases. The correlation between band gap and the size of a spherical NC is expressed in Equation 1.1, where α is a negative constant, E_g is band gap, and V is the volume of the sphere.[2]

$$\alpha = \frac{\partial E_g}{\partial(\ln V)} \tag{1.1}$$

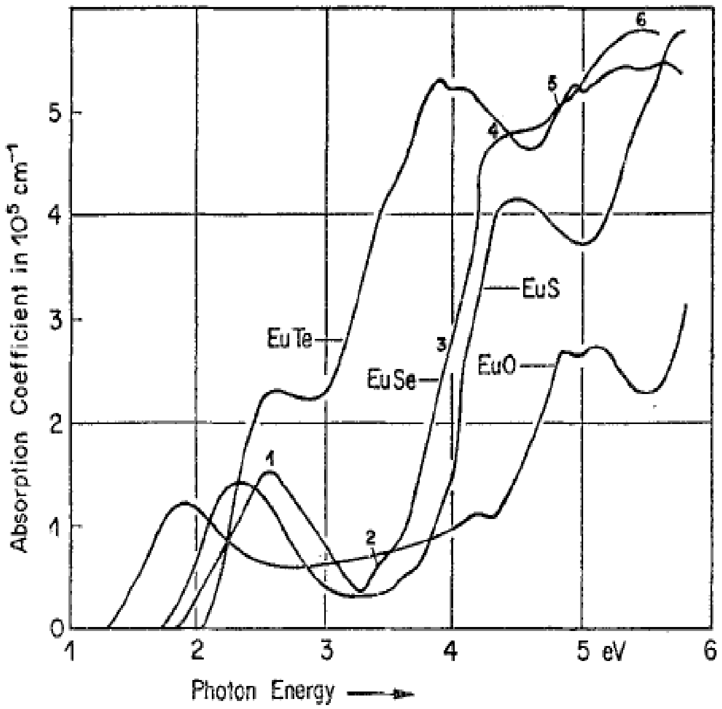

Figure 1.4: Absorption coefficient of the europium chalcogenides at room temperature.[57]

A recent optical absorption study on EuS NPs shows that EuS NPs have two absorption peaks corresponding to high-energy and low-energy electronic transitions of the material, as shown in Figure 1.5.[44] In Figure 1.5, the absorption spectra of 2.5, 5.0, and 12.0 nm EuS NPs all have two absorption peaks. The low-energy peak at ~500 nm is due to $4f^7$-$4f^6 5d^1$ transition, and the high-energy peak corresponds to $4f^7$-$4f^6$ transition. As the size decreases from 12.0 nm to 2.5 nm, the absorption peaks show a blue shift, which can be due to the enhanced quantum confinement as the size of EuS NPs decreases. Figure 1.6 shows the photoluminescence spectra of 4.0 and 12.0 nm EuS NPs. As shown in the figure, a clear blue shift in the luminescent peaks is observed as the size of EuS

NPs decreases. The peaks are due to $4f^65d^1(t_{2g})$-$4f^7$ of Eu^{2+}. The absorption and photoluminescent results of EuS NPs, indicate that the desirable optical properties of EuS NPs can be achieved by finely tuning the size.

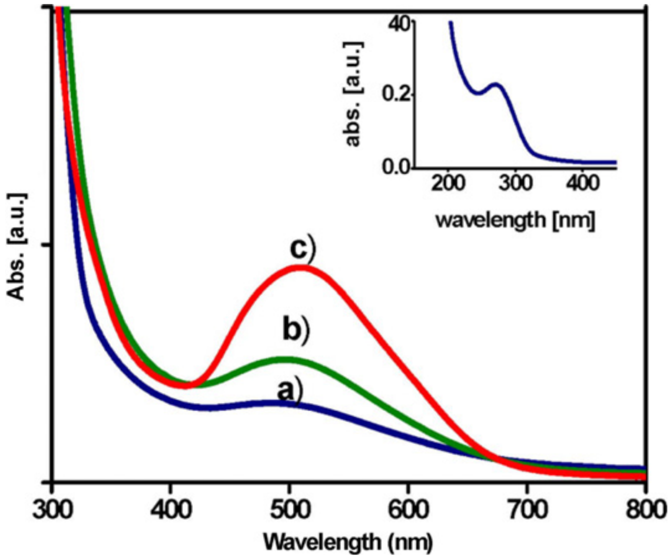

Figure 1.5: Optical absorption spectra of 2.5 nm (a), 5 nm (b), 12 nm (c) EuS nanocrystals in chloroform. Inset: high-energy absorption peak of 2.5 nm EuS NCs.[44]

In Eu^{3+} compounds, the size-dependent optical properties have also been observed. At room temperatures, due to the multiple energy states of 4f electrons, the absorption spectra show multiple peaks due to high-energy and low-energy electronic transitions. As the size of Eu_2O_2S varies, the photoluminescence peaks show dramatic changes due to surface-to-core ratio of Eu_2O_2S atoms.[35]

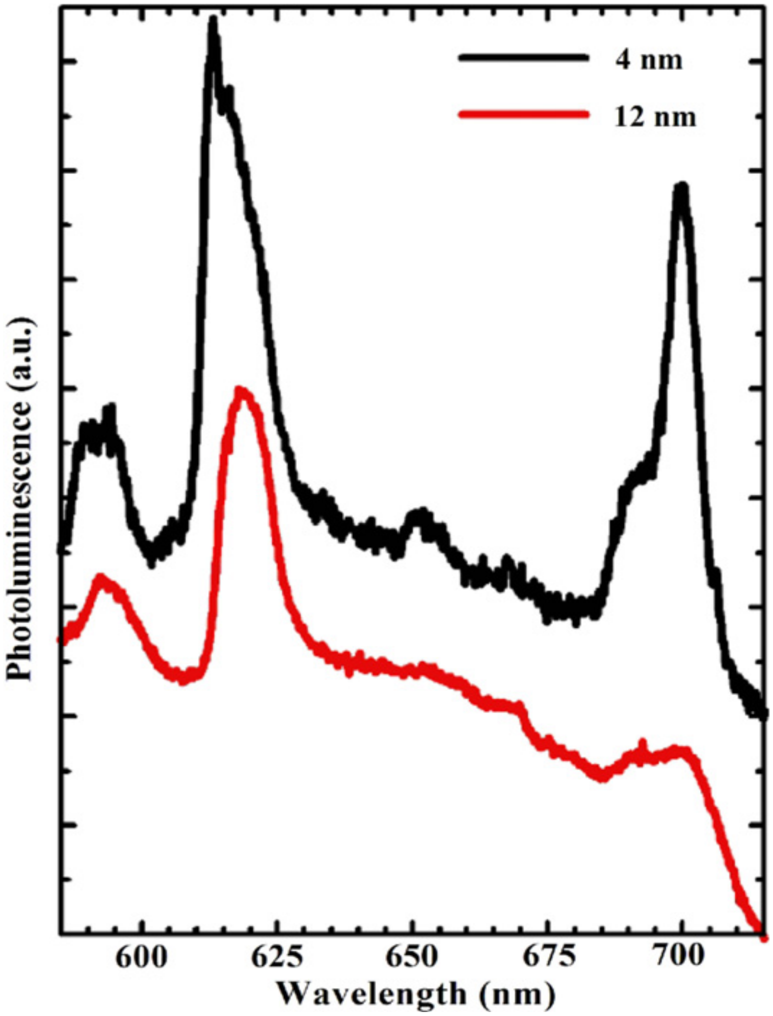

Figure 1.6: Room temperature photoluminescence spectra of 4 nm (Black) and 12 nm (Red) EuS nanocrystals.[44]

Figure 1.7 shows the photoluminescence spectra of bulk and nanoscale Eu_2O_2S. Compared to bulk Eu_2O_2S, the photoluminescent peaks correspond to Eu^{3+} transition from $5D^J$ (J=0, 1) to $7F^J$ (J=0-4). As shown in the figure, the main emission peaks of both Eu_2O_2S samples are broadened compared to the bulk sample. The peak at ~620 nm for the NR sample is more intense than that for bulk sample. When the size of Eu_2O_2S

samples is reduced in the nanoscale regime, the surface-to-core ratio of Eu_2O_2S atoms is much enhanced. The enhanced surface area lowered the crystal field symmetry, gave rise to the observed broadening and enhancing phenomena from the Eu_2O_2S NCs.[35]

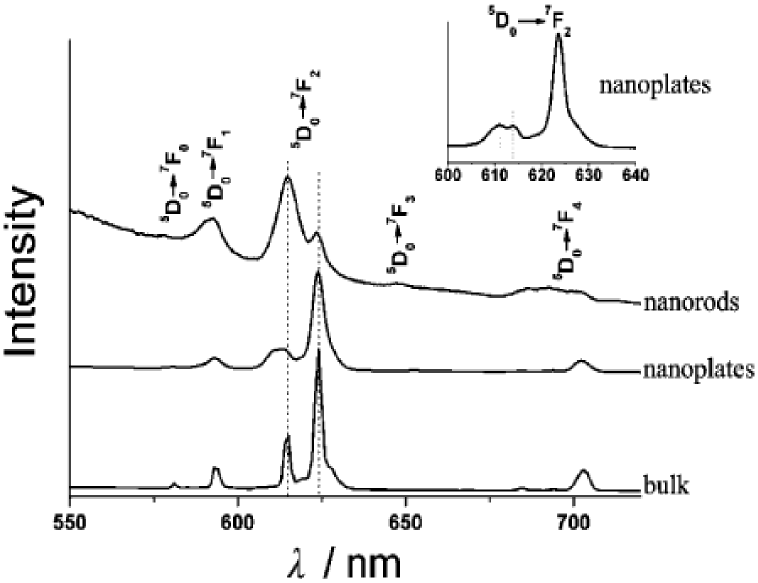

Figure 1.7: Room temperature photoluminescence spectra of different Eu_2O_2S nanocrystals.[35]

1.3 Magnetic properties of solids

1.3.1 General theory of magnetism

The magnetic properties of materials are caused by angular momenta of electrons and the electronic spins. The two contributions are shown in Figure 1.8.[58]

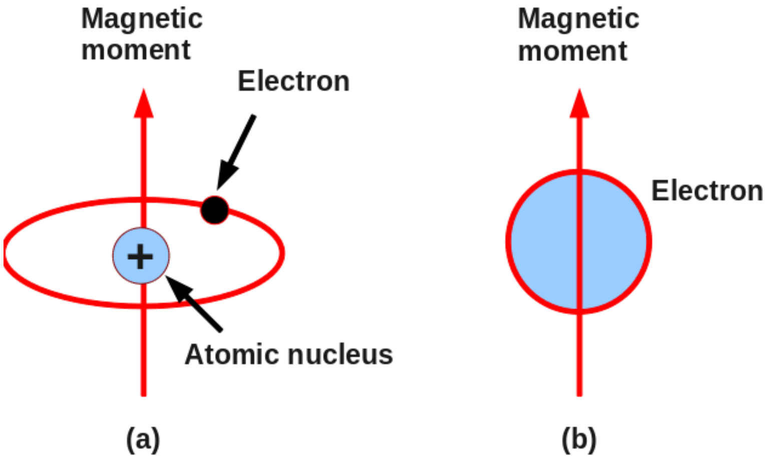

Figure 1.8: Schematic of orbital (a) and spin (b) magnetic moments.[58]

With the angular momentum and spin, each electron behaves as a magnet, and the magnetic moment associated with an electron is known as Bohr magneton μ_B, which is equal to $\frac{eh}{4\pi m}$ (e -charge of an electron, m -mass of an electron, and h -Planck constant).[59] The orbital magnetic moment of an electron and the spin magnetic moment are expressed by Equation 1.2 and Equation 1.3.

$$\mu_l = -g_l \mu_B \frac{2\pi \vec{L}}{h} \tag{1.2}$$

$$\mu_s = -g_s \mu_B \frac{2\pi \vec{S}}{h} \tag{1.3}$$

The sum of $\vec{S}$ and $\vec{L}$ is the total angular momentum, which is labeled as $\vec{J}$. Therefore, the total dipole moment of an electron can be expressed by Equation 1.4. In Equations 1.2-1.4, g is g-factor, and g_j is Lande g-factor.

$$\mu_j = -g_j \mu_B \frac{2\pi\vec{J}}{h} \tag{1.4}$$

When a magnetic material is placed in a magnetic field, the material is magnetized. The magnetization, magnetic field and magnetic flux density are related by Equation 1.5, where μ_0 is free space permeability, $\vec{H}$ is applied magnetic field, and $\vec{M}$ is magnetization.

$$\vec{B} = \mu_0(\vec{H} + \vec{M}) \tag{1.5}$$

The magnetic moment induced by the applied magnetic field per mass is defined as magnetic susceptibility χ, which is given by Equation 1.6.[60]

$$\chi = \frac{\vec{M}}{\vec{H}} \tag{1.6}$$

A material can be diamagnetic, paramagnetic, ferromagnetic, antiferromagnetic, or ferrimagnetic. In a diamagnetic material, all the electrons are paired, and the material shows no magnetic moments without a magnetic field. Under an applied magnetic field, a net dipole moment is induced in diamagnetic material according to Lenz's law. The sign of the induced magnetic moment is opposite to the external magnetic field. The moment is given by Equation 1.7, where Z is atomic number, and $< r^2 >$ is the mean square distance of the electron to the nuclei.

$$\mu = -\frac{e^2 BZ}{6m} < r^2 > \tag{1.7}$$

Therefore, the induced susceptibility is expressed in Equation 1.8, where N is the number of atoms per mass.

$$\mu = -\frac{NZe^2}{6m} < r^2 > \tag{1.8}$$

With the opposite sign, the susceptibility of a diamagnetic material under an applied magnetic field is always negative. The spin and susceptibility schematics of a diamagnetic material with and without external magnetic fields are shown in Figure 1.9a and Figure 1.9b.

With paired electrons, most materials show some diamagnetism, although the magnetic properties of a material can be dominated by ferromagnetism, antiferromagnetism, or paramagnetism.

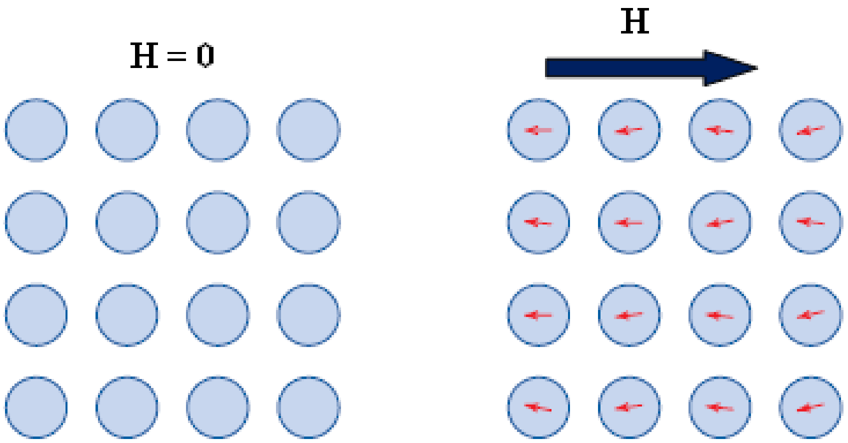

Figure 1.9: Atomic dipole configuration of a diamagnetic material with and without the field.[58]

A paramagnetic material has unpaired electrons that gives rise to a net magnetic moment. The magnetic moment due to the unpaired electrons in paramagnetic material points in random orientations, and the net moment is negligible without an external magnetic field present. If a magnetic field is applied, the magnetic moments can be aligned along the orientation of the magnetic field, which induces a large magnetic moment. However, a thermal variation can randomize the magnetic moment, and due to this thermal effect, a paramagnetic material does not show a magnetic transition as temperature increases. The correlation between temperature and the susceptibility of a paramagnetic material is described by Curie's law as shown in Equation 1.9, where C is Curie temperature and T is external temperature.[61]

$$\chi = \frac{C}{T} \tag{1.9}$$

Langevin built a model based on the assumption that the magnetic moment of a paramagnetic material is only contributed by the interaction between electrons and magnetic field, not by the exchange interaction between electrons. The model is expressed by Equation 1.10, where k_B is Boltzmann constant.[62]

$$\chi = \frac{N\mu^2}{3k_B T} \tag{1.10}$$

With a single parameter T in the denominator of Equation 1.9, Curie law fails to explain a large number of other magnetic materials since in these paramagnetic materials, besides the impact of applied field and external temperature, the magnetic spins interact with each other. Curie's law was developed into Curie-Weiss law by adding an additional parameter in the denominator, which is a measure of the strength of spin-spin interaction. The improved law is then given by Equation 1.11, where θ is Curie-Weiss constant.[60]

$$\chi = \frac{C}{T - \theta} \tag{1.11}$$

The material becomes ferromagnetic when θ is positive, and it becomes antiferromagnetic when θ is negative. The magnetization of a material with $J+1$ energy states can be described by Equation 1.12, where $B_J(x)$ is Brillouin function, which is expressed with Equation 1.13. In Equation 1.13, J is total angular momentum quantum number, which is a sum of orbital quantum number (L) and spin quantum number (S).[62]

$$M = NgJ\mu_B B_J(\frac{gJ\mu_B H}{k_B T}) \tag{1.12}$$

$$B_J(x) = (\frac{2J+1}{2J})\coth(\frac{(2J+1)x}{2J}) - (\frac{1}{2J})\coth(\frac{x}{2J}) \tag{1.13}$$

In ferromagnetic and antiferromagnetic materials, spins can interact with each other, and the exchange interaction between two localized spins can be described by Heisenberg model, as shown in Equation 1.14, where J_{ij} is the exchange constant between the i^th^ and j^th^ ion sites, and S_i is the spin of ion i.[63]

$$H = -\sum_{i,j} J_{ij}\vec{S}_i \cdot \vec{S}_j \tag{1.14}$$

When the exchange interaction results in a parallel alignment of the moments, the exchange constant is positive, and the exchange interaction contributes a ferromagnetic ordering. As the resulted alignment of the moments is antiparallel, the exchange constant is negative, and the exchange interaction contributes an antiferromagnetic ordering.[63]

The wave functions of spinning electrons have two types of overlaps: direct and indirect. When the wave functions have a large overlap, the exchange interaction between magnetic moments is direct.[63] A direct magnetic exchange typically induces a strong ferromagnetic ordering in a ferromagnetic material, such as nickel and cobalt. An indirect exchange is typically realized by the overlap between conduction electrons or itinerant electrons. If the indirect exchange induces a parallel alignment of electrons, the material is ferromagnetic, and if the induced alignment is antiparallel, the material is antiferromagnetic. The ferromagnetic ordering and antiferromagnetic ordering of EuX are caused by indirect exchange coupling. Detailed magnetism of the coupling will be covered in a latter part of this chapter.

Because of the strong parallel exchange interaction between unpaired electrons, a ferromagnetic material has a large magnetic moment with and without an applied magnetic field. The same parallel alignment in a ferromagnetic material occupies a large region in the crystal, which is magnetic domain. The strong parallel alignment can be randomized by thermal motion as the temperature increases above a limit, and the material starts to act paramagnetically. The transition between ferromagnetism and paramagnetism is called Curie transition, and the transition temperature is called Curie temperature. Figure 1.10b shows such a Curie transition of a typical ferromagnetic material.

As an applied magnetic field increases and decreases, the two magnetizations of a ferromagnetic material show irreversibility, and the irreversibility is called hysteresis.

Due to the hysteresis, the magnetization vs. magnetic field curve of a ferromagnetic material has both x-axis and y-axis intercepts. The x intercept is called coercivity and the y intercept is called remnant magnetization. Above a certain magnetic field, the magnetization of a ferromagnetic material reaches its maximum value. The certain magnetic field is called saturated magnetic field.

In an antiferromagnetic material, the unpaired electrons align antiparallel to each other, so the net magnetic moment of an antiferromagnetic material is zero. As temperature increases, increased thermal energy can randomize the antiparallel alignment, and the material starts to have a net magnetic moment. Such an antiferromagnetic-paramagnetic transition is called Néel transition, and the transition temperature is Néel temperature.[60]

In a ferrimagnetic material, the unpaired electrons also align antiparallel to each other.[60] However, the magnitudes of the antiparallel electrons are different. Therefore, unlike an antiferromagnetic material, a ferrimagnetic material has a large net magnetic moment. Like a ferromagnetic material, a ferrimagnetic material also has hysteresis and saturation as changing magnetic field is applied. Figure 1.10 shows an atomic configuration of a ferromagnetic material, and the dependences of magnetization on temperature and applied magnetic field.

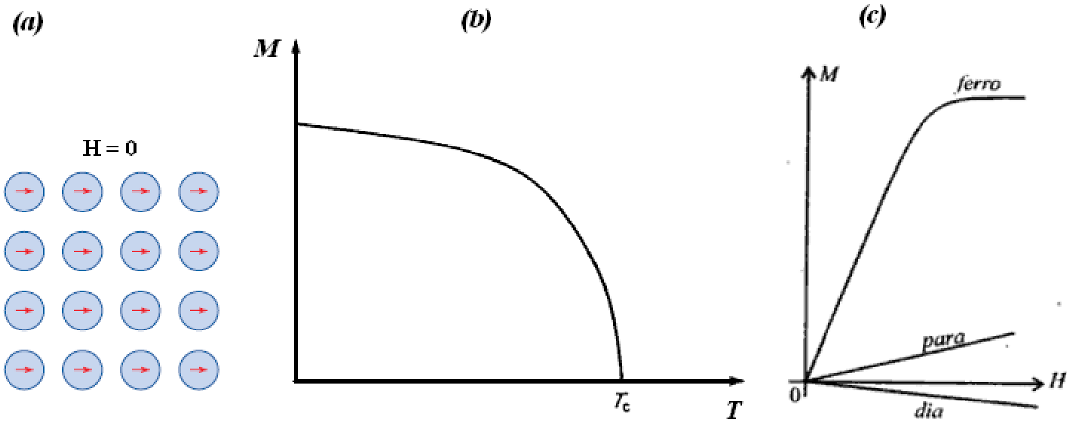

Figure 1.10: (a) Atomic configuration of a ferromagnetic material, (b) dependence of magnetization on temperature for a ferromagnetic material, and (c) dependences of magnetization on applied magnetic field for ferromagnetic, paramagnetic and antiferromagnetic materials.[58]

1.3.2 Superferromagnetism and superantiferromagnetism

When the size of a magnetic material reduces to nanoscale, its magnetic properties can change dramatically. One interesting change is the change from multi-domain to single-domain based on Brown's theorem, which states that magnetic domain formation is entirely suppressed in NCs because of the competition between magnetostatic energy and quantum mechanical exchange energy.[64] Such a transition causes a material to change from normal magnetic to super-magnetic.

Superparamagnetism is a phenomenon by which ferromagnetic and paramagnetic materials exhibit paramagnetic properties even below their Curie temperatures. This phenomenon occurs only within a small length scale, typically when the materials are ~10 nm in size, with significant spins on their surface.[64-65] When a material is superparagmagnetic, the energy barrier of aligning the magnetic moment of a particle is comparable to thermal energy. This makes the particles flip their magnetic moments much more randomly than would a bulk magnetic material. In this case, the interparticle magnetic interaction is weak, and the blocking temperature (below blocking temperatures, thermal energy becomes small, and the magnetic spins are bound in the ferromagnetic or antiferromagnetic sublattices with parallel or antiparalell alignment) is related to Equation 1.15, where K is anisotropy constant, V is the volume of the particles, k_B is Boltzmann constant and T_B is blocking temperature.[16]

$$KV = 25k_BT_B \tag{1.15}$$

The energy barrier to align a particle along the direction of an applied magnetic field is expressed by Equation 1.16, where θ is the angle between the easy axis (an energetically favorable direction of magnetization) and magnetization direction.

$$E_A = KV\sin^2\theta \tag{1.16}$$

As the size of a material reduces from bulk to nanoscale, the material changes from multi-domain to single-domain and then to sub single-domain. More energy is required to align the material as the material becomes single-domain, ending up with a higher coercivity due to a higher anisotropy constant. However, as the size is smaller than the critical single-domain size, due to the change in V, E_A will decrease, which will reduce the coercivity.

Similar to superparamagnetism, superantiferromagnetism occurs when the size of an antiferromagnetic material decreases below the single-domain size.[66-67] Due to large anisotropy energy (compared to Zeeman energy), the magnetization in superantiferromagnetism is significantly related to the uncompensated surface spins of the material, and for small applied magnetic fields, it follows a non-Langevin dependence on the applied field as well as temperature, as shown in Equation 1.17. μ_{nc}(T, V) is the uncompensated moment of particle with volume V and f (V) is the volume distribution function of the particles, m (H, T) is magnetization, H is applied magnetic field, χ_{AF}(T) is antiferromagnetic susceptibility from cores of particles, k_B is Boltzmann constant, and T is temperature. The second sum term on the right of Equation 1.17 represents the magnetization from uncompensated surface spins of the particles. The G function is expressed by Equation 1.18.[66]

$$m_{nc}(H,T) = \chi_{AFM}(T)H + \int_{V_{\min}}^{V_{\max}} \frac{dV}{V} f(V)\mu_{nc}(V,T)G(\frac{\mu_{nc}H}{k_B T}) \qquad (1.17)$$

$$G(x) = \frac{1}{2}\int_0^{\pi} d\theta \sin\theta \cos\theta \tanh(x\cos\theta) \qquad (1.18)$$

There are two significant differences between superparamagnetism and superantiferromagnetism. First, superparamagnetism is characterized by the monotonous paramagnetic behavior of a material around the Curie point, for which the material in bulk form changes from paramagnetic to ferromagnetic as the temperature decreases. Superantiferromagntism is characterized by an extra increase of magnetization as temperature decreases below the Néel point where the material in bulk form changes from paramagnetic to antiferromagnetic. In a normal antiferromagnetic material, such an increase of magnetization is absent as the material becomes antiferromagnetic from paramagnetic below Néel temperature.[68] Second, similar to the difference between paramagnetism and antiferromagnetism, the magnetization in superparamagnetism is several orders of magnitude larger than that in superantiferromagnetism in which the susceptibility is on the order of 10^{-5} emu/Oe·g.[69-70] The two differences between superparamagnetism and superantiferromagnetism, as stated above, are used to distinguish the two phenomena.

1.3.3 4f electrons and magnetic properties of EuX

The magnetic properties of EuX are caused by the 4f electrons in the shell of Eu^{2+} cation. According to Hund's rule, the lowest energy multiplet of the seven 4f electrons have their spin parallel has $S = 7/2$, $L = 0$ and $J = 7/2$. Since the atomic energy levels are characterized by ${}^{2S+1}L_J$, the ground state of Eu^{2+} in EuX is ${}^{8}S_{7/2}$.[71] In EuX, most 4f electrons are within 5s and 5p shells of Eu and these closed electrons are screened by the electron shells. Due to the screened 4f-4f overlap, the direct exchange interaction of nearest–neighbor sites is weak. However, in 4f ferromagnetic EuO and EuS, indirect coupling between conduction electrons or the ligands takes place and creates ferromagnetic ordering in the materials. Compared to direct coupling, the indirect exchange coupling is weak, require lower thermal energy for magnetic transitions, and the Curie temperatures are typically lower than those of the 3d ferromagnetic materials, such as nickel, cobalt and iron. Due to the localized 4f electrons in the Eu^{2+}, EuX are regarded as classical Heisenberg magnets. The magnetic interaction for EuX is given by Equation 1.19.[63]

$$H = -\sum_{i,j} J_{ij} \vec{S}_i \cdot \vec{S}_j = -\sum_{nn} J_1 \vec{S}_0 \cdot \vec{S}_{nn} - \sum_{nnn} J_2 \vec{S}_0 \cdot \vec{S}_{nnn} \qquad (1.19)$$

In the indirect exchange, J_1 is mainly contributed by the cation wave functions. The cation wave functions are due to the nearest neighbor of cations, and, thus, the magnetic properties of ferromagnetic EuO and EuS are mainly caused by J_1. This indirect exchange is realized by the virtual transfer of a 4f electron to the empty 5d of the Eu^{2+} ion. Therefore, compressive strain by suppressing the lattice constants can increase the effective indirect overlap of 5d orbitals in Eu^{2+} cations.[63]

In antiferromagnetic super exchange mechanism, magnetic moments are contributed by the wave functions of localized spins by exchange coupling between next nearest neighbors, and p electrons of the anion in EuX play an important role. The anion wave function in the rock salt structure of EuX connects two next nearest cation sites.[26] The two cations connected by an anion are next nearest neighbor to each other. Different from J_1, J_2 is contributed by the next nearest neighbor superexchange between d-f electrons. In the superexchange, the p electrons from X move to 5d states of Eu^{2+} cations, and then interact with the 4f electrons in Eu^{2+}. If J_1 is dominant in the magnetic exchange in a EuX, the EuX is ferromagnetic, such as EuO and EuS. When J_2 is dominant in EuX, the EuX is antiferromagnetic or ferromagnetic, such as EuSe and EuTe.

An important direction of research on magnetism is tuning the transition temperatures of ferromagnetic and antiferromagnetic materials to applicable temperature ranges so that the materials can be made into devices. An efficient method of decreasing or increasing the transition temperatures is varying the size of magnetic NCs. As reported by Zhao et al, the TC of EuS can be tuned from its bulk value 16.6 K to 4.6 K as the size of EuS NPs is changed from 20 nm to 2.6 nm.[72] $\chi.T$ vs. T plots for EuS NPs are shown in Figure 1.11.[16] The temperatures at the peaks correspond to the TC of EuS NPs.

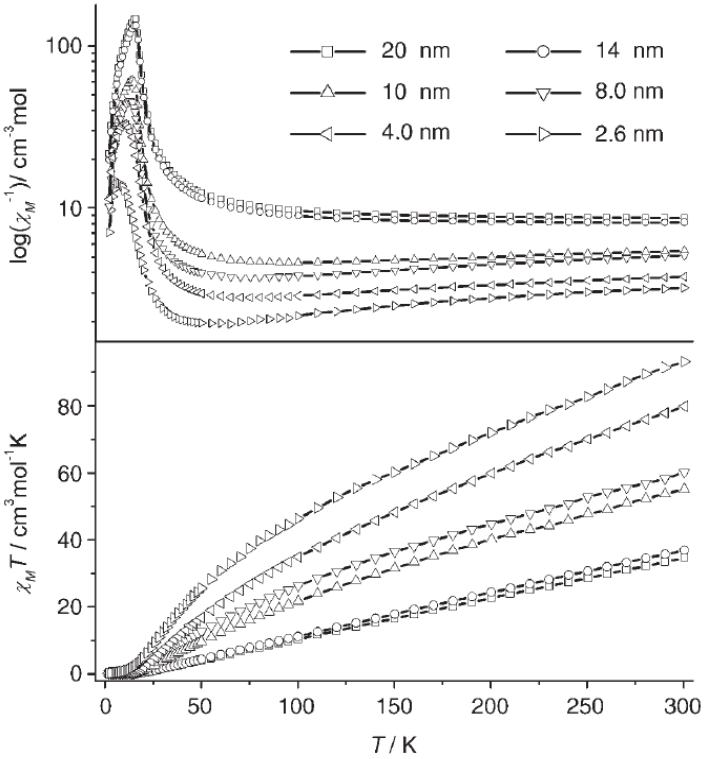

Figure 1.11: $\chi \cdot T$ vs. T and log (χ^{-1}) vs T plots for EuS nanoparticles of different sizes.[16]

Another efficient method of tuning the transition temperature of magnetic materials is introducing lattice strain. In W. Söllinger et al's report, the ordering temperatures of EuO, EuS, EuSe and EuTe crystals were changed by introducing compressive lattice strain on the crystals.[73] Figure 1.12 shows the correlation between lattice constant with the Curie temperature, exchange constants for EuO crystals.

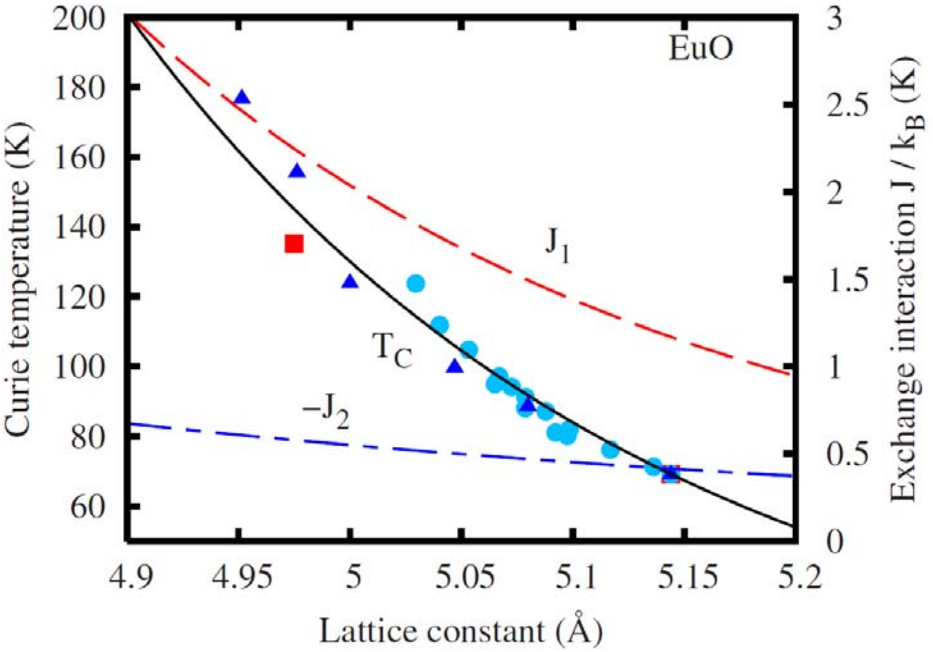

Figure 1.12: Dependences of Curie temperature and exchange constant on lattice constant of EuO crystal.[73]

1.4 OR and OA growth

To achieve desirable properties from NCs, we need to have pronounced control on the size and morphology of these NCs since the physical properties are directly related to their size and morphology.[74] To control these important parameters, we need to understand the growth mechanism of colloidal NCs. There are two important growth mechanisms in colloidal chemistry: Ostwald ripening (OR) and oriented growth (OA) mechanisms.[48] Ostwald-ripening mechanism is an observed growth mechanism that dominates the growth of colloids. In such a mechanism, small particles dissolve as a result of higher dissolvability and surface energy, and redeposit onto larger particles. In an OR growth controlled by volume diffusion, the kinetics model is shown in Equation

1.20, where d_o is the diameter of precursor NPs, d_t the diameter of NPs at time t and k (m^3/min) reaction constant.[75]

$$d_t = \sqrt[3]{d_0^3 + kt} \tag{1.20}$$

Oriented-attachment growth, directly from individual NPs, has been found to be an effective way to synthesize nanomaterials. In OA growth, NP monomers tend to attach to each other along a certain crystal orientation. Oriented attachment (OA) growth directly from individual NPs has been found to be an effective way to produce 1D nanomaterials. OA mechanism is complicated considering its various kinetic models caused by the participation of multilevel particles in the reaction. Assuming reaction occurs between primary nanoparticle monomers, its kinetic model can be explained by Equation 1.21.[75]

$$d_t = \frac{d_0(\sqrt[3]{2}kt + 1)}{kt + 1} \tag{1.21}$$

Comparing Equation 1.20 and Equation 1.21, we easily find that d_t tends to reach a maximum in the OA model while it monotonously increases with time in the OR model. Therefore, combining time-evolved experimental data, the models can help to evaluate the growth mechanism of NR growth. Figure 1.3 shows the evolution of NCs via OR and OA growths.

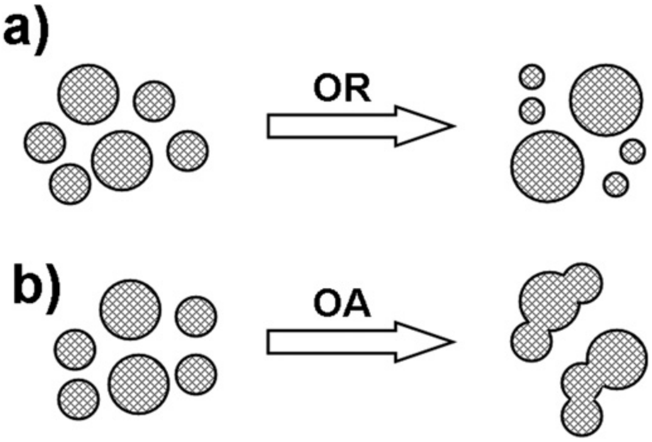

Figure 1.13: Schematics of OR and OA growths.[75]

1.5 Electrophoretic deposition of NCs

Once NCs are synthesized, we can either study their physical properties to explore their new scientific phenomena or use them as building blocks in device applications. For many applications, we need to assemble these NCs into uniform films which can then be integrated into devices. As an efficient film deposition technique, EPD has recently drawn much attention.[76-78]

1.5.1 Essentials of EPD

An EPD process contains two steps: electrophoresis and deposition. During electrophoresis, ligated colloids in a solvent are driven by electric field to move apart from one electrode to the other. Once the colloids reach target electrodes, the colloids start to form deposition on the electrodes. Accordingly, there are some important factors determining whether a good EPD will occur or not. First of all, well-ligated colloidal NCs have to be chosen as depositing units before deposition. Colloids have to be ligated in order for them to move under an electric field. Charges induced by the electrical field can come from the following resources: surface ligands, deviations in stoichiometry, ions from the particle, and ions from the solvent. In typical EPD processes, surface ligands are used to charge colloids. During the synthesis of colloids, functional groups such as carboxylic acids, amines and thiols, can ligate the synthesized colloids, resulting in charged moieties.[79]

An efficient EPD also requires a good solvent. The colloids need to be well-dispersed in the solvent. In such a solvent, the aggregation of colloids is detrimental to the deposition or cause a bad deposition. Whether or not a solvent can disperse the colloids well depends upon the compatibility of the solvent with both the colloids and their surface ligands.[80]

Another key factor is the electric field applied. This is again determined by both ligands and solvents. If the induced charge is large enough, a polar solvent, such as methanol and water, need small voltages, such as several volts, to drive the colloids while a non-polar one requires much larger voltages. For example, hexane-based deposition usually requires voltages up to several hundred volts. There are also some other important factors, such as electrodes, deposition time, PH of the colloidal system and temperature, etc.[81] Figure 1.14 shows a schematic of an EPD process.

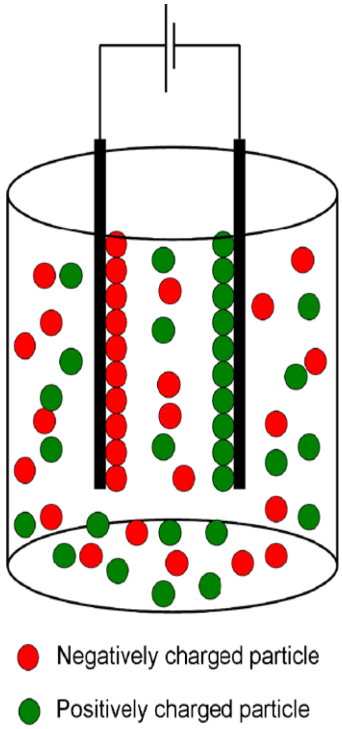

Figure 1.14: Schematic of EPD process. (Sources from Professor James Dickerson's group)

1.5.2 Materials deposited via EPD

A variety of materials can be assembled into films using EPD. EPD has become a popular method of depositing ceramic, metallic, and semiconducting nanomaterials as well as polymers into fine films. In our group, we have successfully accomplished the deposition of linear and star polymers, various quantum dots, carbon nanotubes, and graphene sheets.[76, 78, 81] In particular, our group successfully deposited a Eu^{3+} compound, 4 nm Eu_2O_3 NCs, into uniform EPD films.[82] The optical microscopic and Scanning Electron Microscopic (SEM) images of Eu_2O_3 NC films deposited for different times are shown in Figure 1.15. The successful electrophoretic deposition of Eu_2O_3 NC films shows that the synthesized Eu_2O_3 NCs are easy to assemble, and, thus, are highly-applicable for optical applications due to their photoluminescence properties. The successful deposition of such a Eu compound indicates that other Eu compounds could also be deposited into uniform NC films via EPD. The deposition of other Eu compounds will be discussed in later chapters.

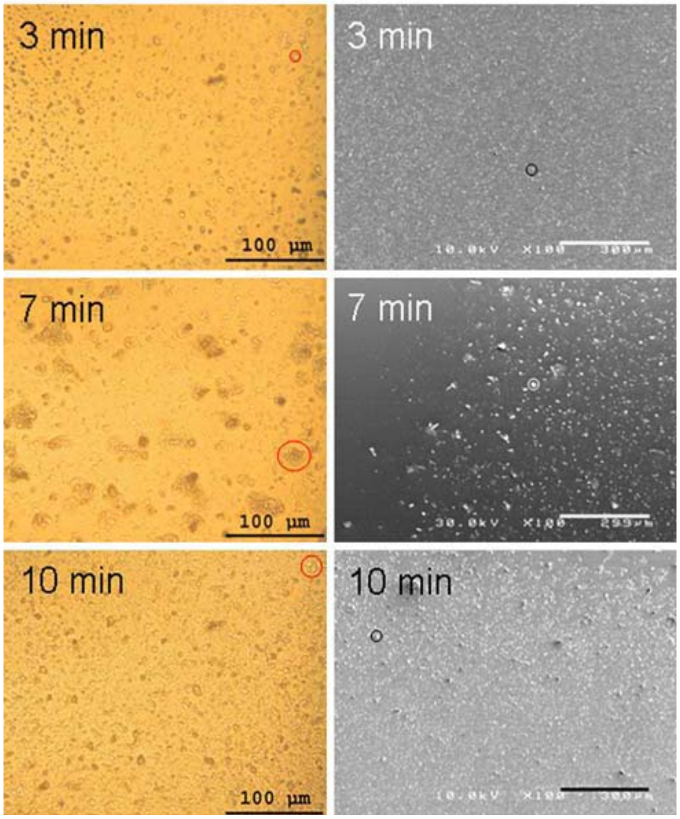

Figure 1.15: Optical microscopic (left) and SEM images (right) of the Eu_2O_3 nanocrystal films, deposited for different times.[82]

Summary: Europium compounds were introduced, and the optical and magnetic properties of europium compounds were summarized. The concepts of diamagnetism, ferromagnetism, antiferromagnetism, superparamagnetism, and superantiferromagnetism were discussed in depth. A review of recent study on EuTe crystals was given and the research challenges associated with europium compound were presented. Colloidal synthesis oriented-attachment growth, and EPD of NCs were also discussed.

Following the introduction in Chapter I, the other chapters will represent and discuss the theoretical and experimental findings associated with the synthesis and property characterizations of the NCs, growth mechanism, and electrophoretic deposition of the materials.

Chapter II presents the colloidal synthesis of EuS, EuTe, Eu_2O_2S, and Te NCs. Colloidal routes to 1D structures and quantum dots of these NCs are described and discussed. A number of important synthetic parameters, such as precursor concentration, surfactant, and temperature, are analyzed. X-ray diffraction (XRD) and Fourier transform infrared spectroscopy (FTIR) are applied to study the structural properties of as-synthesized NCs.

Chapter III studies the size-dependent optical and magnetic properties of ultra-small EuS, EuTe and Eu_2O_2S NCs. Gilles' model is applied to analyze the superantiferromagnetic properties of EuTe NPs. Absorption and photo-luminescent properties of these NCs are characterized and investigated.

Chapter IV talks about the growth mechanism of EuS NPs and nanorods (NRs). The analytical expression of a significant controlling parameter, van der Waals interaction (vdW), is derived for the OA growth of 1D NRs.

Chapter V investigates the electrophoretic assembly of as-synthesized colloidal NCs. The composition and surface morphology are characterized and analyzed. In addition, the aggregation growth of deposited Te and Eu_2O_2S NCs as well as dimensionality-dependent deposition of Te NCs are described and discussed.

Chapter VI summarizes the research presented in this dissertation and discusses the research opportunities on the materials and techniques associated with this work.

CHAPTER II

COLLOIDAL SYNTHESIS AND STRUCTURAL CHARACTERIZATIONS OF EuS, EuTe, Eu_2O_2S AND Te NANOCRYSTALS

2.1 Introduction

Among EuX (X=O, S, Se, or Te), EuS nanocrystals have been synthesized by different groups using different methods, the most common ones of which are thermolysis and colloidal methods.[16, 21] In thermolysis synthesis of EuS NPs, a Eu precursor, such as Eu diethyldithiocarbamate complex with 1, 10-phenanthroline ($Eu(ddtc)_2Phen$), is synthesized. The Eu precursor is mixed with diethyldithiocarbamic acid diethylammonium (DEDTC) salt with vigorous stirring in glove box.[83] The mixture is then transferred to a tube furnace and annealed at reaction temperatures. During reaction, the reaction system needs to be purged with inert gases, such as nitrogen. The schematic of a tube furnace is shown in Figure 2.1.

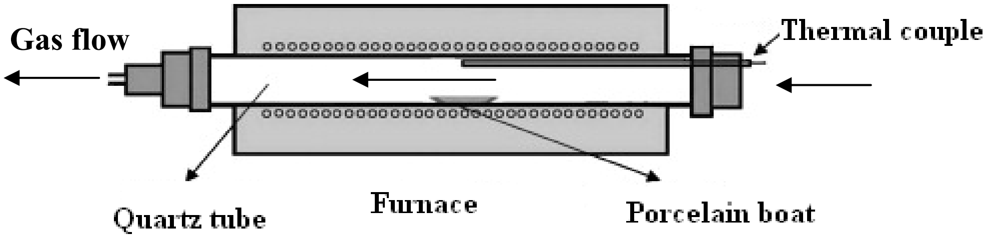

Figure 2.1: A tube furnace setup for thermolysis reaction of EuS NCs.[83]

The biggest disadvantage of thermolysis synthesis is that the size and morphology of EuS NCs are not uniform. To solve this problem, Gao, Stoll, Hasegawa and Dickerson groups developed high-controllable colloidal methods for the synthesis of EuS NPs. Colloidal EuS NPs are monodisperse and well-ligated with organic ligands, which allow the NPs to form a stable suspension in a solvent.[15-16, 44, 84] The synthesis of EuO NCs has also been achieved by different groups using different methods. For example, the Song group synthesized EuO nanorods via a chemical vapor deposition method. Compared to EuO and EuS NC, the synthesis of EuSe and EuTe NCs are not as straightforward due to the lack of stable Se and Te precursors. Hasegawa et al reported the first synthesis of EuSe NCs in 2008, and they observed remarkable magnetic-optical properties on the EuSe NCs.[102] However, their colloidal method failed to control the shape and size of EuSe NPs. Among the four Eu monochalcogenides, EuTe NCs are the most difficult to synthesize due to the weak chemical bonding between Eu and Te. The weak bond between Eu and the semimetal Te makes EuTe NCs the most unstable among the four materials. Till 2010, there had been no report the synthesis of EuTe NCs. Compared to the synthesis of EuTe NCs, the syntheses of Eu^{3+} compound, Eu_2O_2S and, semimetallic chalcogen Te NCs have been done by many groups using different colloidal methods or chemical vapor deposition methods.[35, 85] Eu_2O_2S nanowires, nanoplates and nanorods have been synthesized using colloidal methods.[34-35] Although most of the synthetic routes produce monodisperse Eu_2O_2S NCs, they fail to synthesize ultra-small NPs and ultra-thin NRs with diameters of several nm. Te NCs have also been synthesized by various groups. However, due to the hexagonal crystallinity, most of the syntheses are on 1D Te NCs.

In this chapter, a colloidal method for EuTe NCs is introduced and analyzed. The size and shape control using this newly-developed method is discussed. A facile method of using ultra-thin Eu_2O_2S NRs is discussed with a focus on the diameter and aspect ratio control on the NRs. The colloidal synthesis of Te NPs with binary size is also covered in this chapter. For each material, their size, shape, crystallinity, and ligand information are characterized with TEM, SEM, XRD and FTIR, respectively.

2.2 Colloidal synthesis of EuTe NCs

2.2.1 Experimental details

Synthesis of 6.6 nm EuTe Nanoparticles (Sample 1). All synthetic steps were carried out in a nitrogen filled, moisture-free glove box at room temperature.[87] In a typical synthesis, $EuCl_2$ (0.0446 g) was dissolved in a mixture solution of 15 mL ethylene glycol (EG) and 4 mL triethanolamine (TEA) under vigorous stirring. 2 mL of 0.1 M solution of anhydrous Na_2Te in EG was added dropwise into the vigorously stirred anhydrous $EuCl_2$ solution. The resulting 0.025 g black-colored EuTe nanoparticles were separated out via centrifugation and washed with methanol four times and stored in methanol for further measurements.

Synthesis of 7.3 nm EuTe Nanoparticles (Sample 2). The synthesis is the same as that for 6.6 nm EuTe nanoparticles except that the concentrations of $EuCl_2$ and Na_2Te were 0.1 M.

Synthesis of 5.5 nm EuTe Nanoparticles (Sample 3). The synthesis is the same as that for 6 nm EuTe nanoparticles except that the concentrations of $EuCl_2$ and Na_2Te were 0.4 M.

2.2.2 Characterization techniques

High resolution transmission electron microscopy and selected area electron diffraction (SAED) pattern images were obtained using a Philips CM 200 TEM operating at 200 kV. HR-TEM samples were made by drop-casting the EuTe nanoparticle suspensions on carbon-coated copper grids. The UV-Vis spectra were recorded with a Varian Cary 5000 UV-VIS-NIR spectrophotometer. Powder XRD measurements were made using a Scintag X1 powder diffractometer. A Bruker Tensor 27 FTIR spectrometer was used to measure FTIR spectra of EuTe NPs. Energy dispersive X-ray (EDS) analysis was performed using a Hitachi S-4200 Scanning Electron Microscope operated at a 20 kV acceleration voltage.

2.2.3 Results and discussion

The ease of TEA bonding to Eu^{2+} ions in the EG solution facilitated the formation of a chelate compound $[Eu(TEA)n]Cl_2$ in the early stages of the synthesis. Upon injection of the EG solution of Na_2Te, EuTe NPs were formed, which readily precipitated in the reactor. Two reaction steps are associated with the formation of EuTe, as described in Scheme 2.1, which is consistent with the report from Xu et al on SnS.[86]

$$EuCl_2 + nTEA \xleftrightarrow{Stirring} [Eu(TEA)_n]Cl_2 \qquad (1)$$

$$[Eu(TEA)_n]Cl_2 + Na_2Te \longrightarrow EuTe\downarrow + 2NaCl + nTEA \qquad (2)$$

Scheme 2.1: Reaction schematic of EuTe colloidal synthesis.[86]

Synthesized EuTe NPs were capped by groups of TEA, which was confirmed by Fourier transform infrared spectroscopy, shown in Figure 2.2.[87]

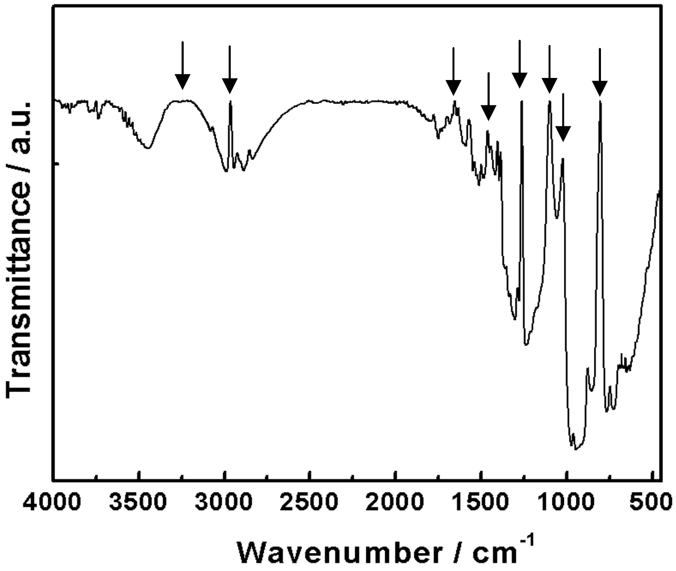

Figure 2.2: FTIR spectrum of 6.5 nm EuTe nanoparticles. Peaks identification: O–H vibration, 3500-3000 cm^{-1}; C–H stretching band, 3000-2800 cm^{-1}; C–C and C–H bending, 1460-1130 cm^{-1}; C–O and C–N stretching, 1100-890 cm^{-1}; C–C–O vibrations, 880-690 cm^{-1}. Physisorbed and chemisorbed water, 3500 to 3000 cm^{-1} and 1800-1500 cm^{-1}.[87]

The ligands largely helped prevent EuTe oxidation in an oxygen rich environment. Typical transmission electron microscope images of EuTe NPs are shown in Figure 2.3. As seen from the images, the NPs were nearly spherical. Clear lattice fringes in Figure 2.3 corresponding to the (200) plane of EuTe, confirmed the crystallinity of the sample. The NP size distribution is given in the histogram; the average size of the NPs, 6.5 nm ± 1.7, corresponded to $EuCl_2$ and Na_2Te concentrations of 0.20 M. Similarly, we synthesized NP samples from 0.10 M and 0.40 M concentrations that yielded average diameters of 7.3 nm ± 1.7 nm and 5.5 nm ± 1.5 nm, respectively, evidenced by the size distribution histograms of the two samples, as shown in Figure 2.3. The fact that high concentrations of starting materials tend to yield smaller EuTe NPs is consistent with

Reiss's prediction on the size-distribution of particles.[88] The electron diffraction in Figure 2.3 showed well-resolved lattice planes that correspond to the (111), (200), (220), and (222) planes of cubic EuTe.

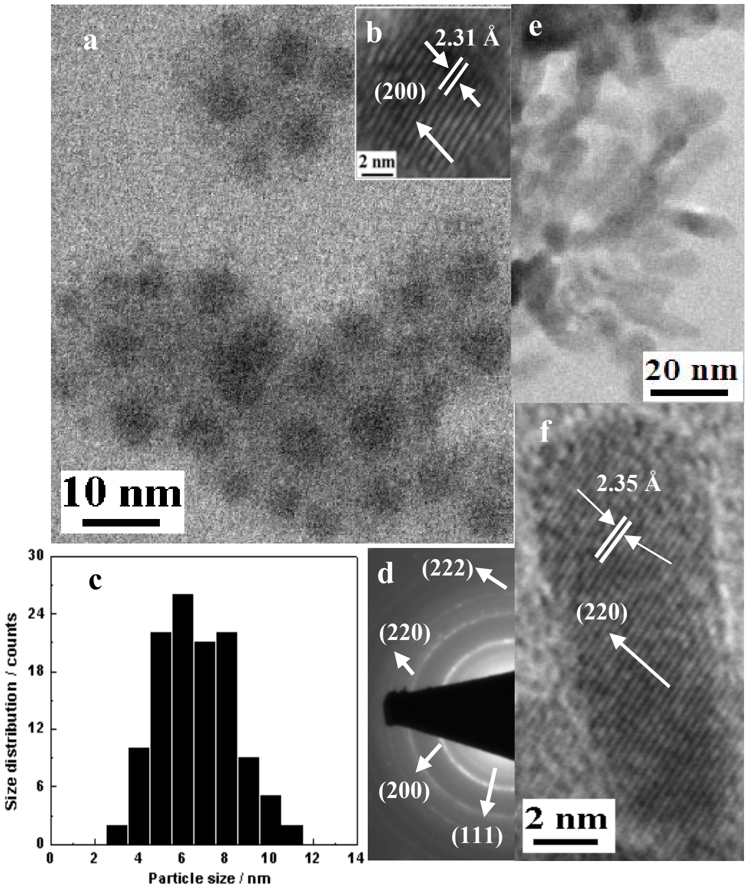

Figure 2.3: (a, b) TEM images of 6.5 nm crystalline EuTe NPs. Average diameter is 6.5 nm. Circles are to guide the eye; (c) Histogram of NP size distribution; (d) Electron diffraction pattern of FCC EuTe NPs; (e, f) TEM images of EuTe NSs.[87]

From the TEM images of as-synthesized EuTe NSs, the NSs are 6.8 nm in diameter and 20.4 nm in length. The observed lattice spacing was 2.34 Å, which corresponds to the (220) plane. These lattice planes are further confirmed by the strong electron diffraction ring, as confirmed by Figure 2.4. The formation of as-synthesized anisotropic EuTe NSs was driven by the surface packing of phenanthroline. Before or during nucleation, electron-rich phenanthroline self-organized into an elongated micelle-like structure and then the formed elongated structure served as template for the formation of 1D EuTe NCs, similar to what were proposed on the formation of Au and CdSe NRs.[89-90] The elongated nuclei resulted in different packing densities of phenanthroline on different lattice planes of EuTe crystals, which resulted in the different growth rates along different crystal orientations and facilitated the anisotropic growth.

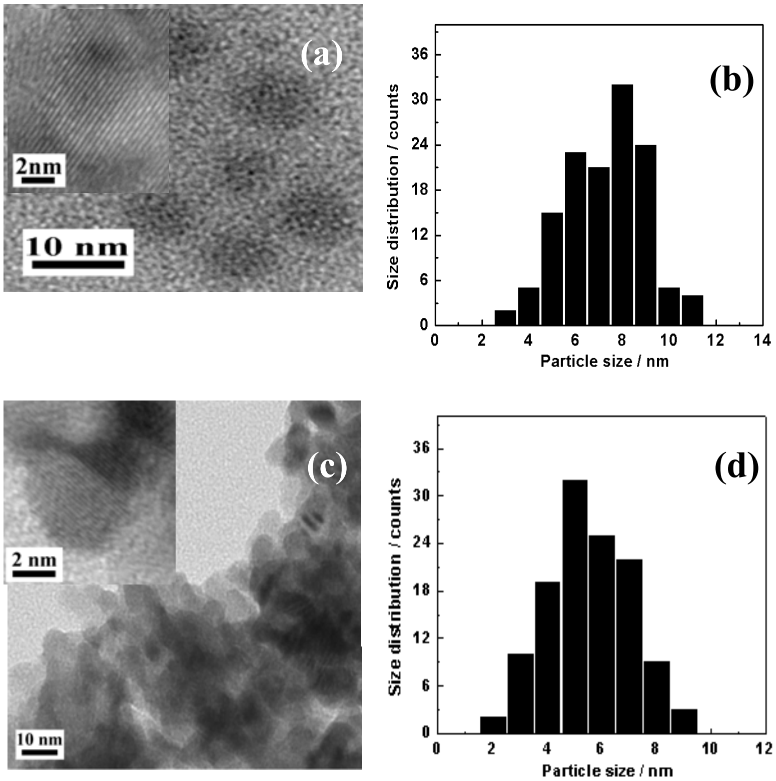

Figure 2.4.: HR-TEM images of EuTe nanoparticles: (a). 7.3 ± 1.7 nm and (c) 5.5 ± 1.5 nm. The corresponding histograms of size distributions for 8 nm and 5 nm nanoparticles showing in (b) and (d).[87]

X-ray diffraction spectra of the colloidal EuTe NPs and NSs provide complementary affirmation of the formation of highly crystalline EuTe nanocrystals, as shown in Figure

2.5. All four samples have the dominant peak at 2θ = 27.7º, which is assigned to the (200) lattice of NaCl-type EuTe. Two smaller peaks are observed at 2θ=40.0º and 2θ=49.6º; we attributed those peaks to metallic tellurium that formed on the surface of the EuTe nanocrystals through the oxidation of EuTe when exposed to air. By evaluating the full width at half-maximum of the (200) peak and applying the Scherer equation, the diameters of the 7.3 ± 5.0 nm, 6.5 ± 5.3 nm and 5.5 ± 4.5 nm NPs (determined by TEM) were calculated to be 9.5 ± 5.6 nm, 7.2 ± 4.8 nm and 6.5 ± 5.2 nm, respectively. The 20 nm long EuTe NSs was calculated to be 16.3 nm. The difference in the sizes from TEM and XRD could be due to the increased inaccuracy of size estimation using XRD data as the size of NCs is only several nm in size.

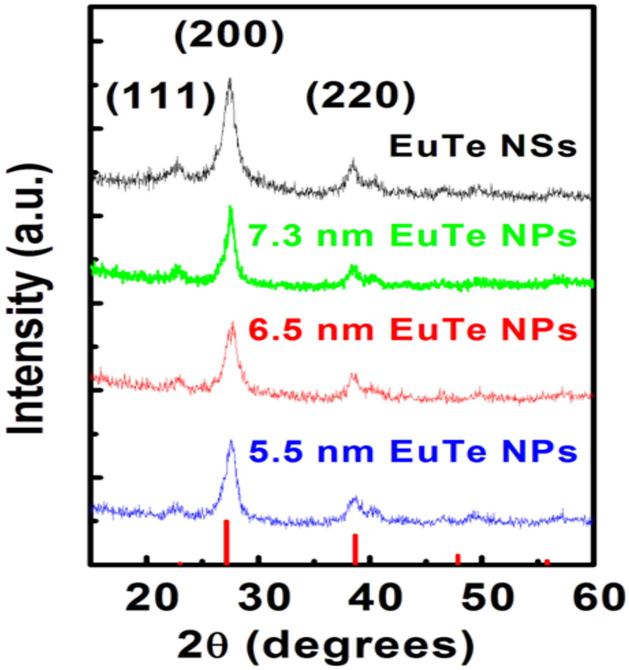

Figure 2.5: XRD spectra of EuTe NPs and NSs. Red bars represent primary diffraction peaks of EuTe from its JCPDF file.[87]

2.3 Colloidal synthesis of Eu_2O_2S NCs

2.3.1 Experimental details

All chemicals used in this experiment were used without further purification. The sodium oleate (95%) was acquired from TCI America, while the other chemicals (europium (III) chloride hexahydrate (99.99%), oleylamine (70%), n-hexane, acetone, isopropanol, diethylammonium diethyldithiocarbamate (98%), 1-dodecanthiol (98%), and phenanthroline (99%)) were purchased from Sigma-Aldrich. The syringe pump was purchased from Razel Scientific Instruments. Prior to the synthesis of the nanorods, europium oleate was synthesized using the europium (III) chloride hexahydrate, the sodium oleate, ethanol, hexane, and deionized water via a previously reported procedure.[44] Eight mmol of europium (III) chloride hexahydrate and 24 mmol of sodium oleate were combined along with 16 mL of ethanol, 12 mL of deionized water, and 28 mL of hexane in a three-mouth flask. The substance was heated to 60°C and left for about three hours. Afterwards, a separatory funnel was used to segregate the europium oleate in a layer of hexane from the unnecessary products. Deionized water was added to the substance and after waiting several minutes, the bottom layer was drained again. This was repeated four times to clean the resulting substance.

The nanorods themselves were synthesized in a Schlenk line. A mixture of 0.2 mmol of europium oleate, 0.2 mmol of phenanthroline, 0.1 mL of dodecanthiol, and 10 mL of oleylamine was vacuumed and heated to 80°C in a three-neck flask, after which the mixture was left for 40 minutes to allow the mixture to purify prior to increasing the temperature to 320°C, all while being constantly stirred. Meanwhile, 0.2 mml of DEDTC was mixed with 5 mL of oleylamine and degased with argon. Once the desired temperature of 320 °C was reached, the syringe pump was used to inject the previously de-gassed mixture of DEDTC and oleylamine into the heated flask at the desired rate (0.5 mL/min to 25 mL/min). The substance reacted for an hour before being inserted into a vial, using acetone as a solvent. After several hours passed to allow the nanorods to precipitate, the liquid was poured out of the vial slowly before being refilled with acetone. This process was repeated four times in order to clean the samples. After cleaning, 0.015 m sample was produced for one synthesis.

2.3.2 Characterization techniques

High resolution transmission electron microscopy and selected area electron diffraction (SAED) pattern images were obtained using a Philips CM 200 TEM operating at 200 kV. X-ray diffraction measurements were obtained using a Scintag X1 powder diffractometer. Fourier transform infrared spectroscopy measurements were obtained using a Bruker Tensor 27 Fourier Transform Infrared spectrometer. Atomic force microscopy measurements were obtained using a Digital Instruments Nanoscan III Atomic Force Microscope.

2.3.3 Results and discussion

Ultra-thin europium oxysulfide NRs were synthesized by the hot injection of the sulfur precursor diethylammonium diethyldithiocarbamate into a europium oleate, oleylamine, and phenanthroline mixture at 320 °C. We chose europium oleate because the oleate was shown to be an effective precursor for the preparation of europium compound NPs with precise size control, as our previous research demonstrated. Hot injection facilitates the rapid formation of nuclei, which is correlated with the growth kinetics of NCs, and is frequently applied to synthesize colloidal NCs through various growth mechanisms, such as Ostwald ripening, oriented attachment, and ion exchange. With proper surfactants, rapid nucleation and growth can occur along the most active lattice orientations, which are not heavily passivated by the surfactants. Therefore, the hot-injection technique is often regarded as the preferred approach to synthesize 1D NCs with great control over their AR. In our synthesis, the europium oxysulfide NR diameters could be adjusted in a range from 1.5 nm to 3.5 nm, with controllable ARs ranging from 3 to 20, by varying the injection rate and the amount of phenanthroline. Interestingly, the absence of phenanthroline led the formation of europium oxide (Eu_2O_3) NRs. This demonstrates a possible avenue for their implementation in the aforementioned imaging and lighting applications. The diameter, AR, and lattice structure of the europium oxysulfide NRs were characterized by high resolution transmission electron microscopy and selected area electron diffraction (SAED) using a Philips CM 200 TEM operating at 200 kV. As shown in Figure 2.6, the diameter and AR of the synthesized europium oxysulfide NRs are highly uniform. In syntheses, the amount of phenanthroline and the injection rate were varied while the amount of sulfur precursor diethylammonium diethyldithiocarbamate was kept at 0.2 mmL. With the amount of phenanthroline kept constant at 0.2 mmol, the injection rate was increased from 0.5 to 25 mL/min. Although the AR of the NRs remained constant at 5, the diameter decreased from 3.5 to 1.5 nm (see Figure 2.7). Faster injection rates facilitate the rapid nucleation and growth of NRs with growth-terminating surfactants at a fixed AR of 5. With the injection rate fixed at 5 mL/min, the diameter of the NRs decreased from 3.5 nm to 1.5 nm as the amount of phenanthroline increased from 0.1 to 0.4 mmol. In the meantime, the AR of the NRs decreased from 3 to 20 as the amount of phenanthroline increased. In contrast to that observed for the synthesis of EuS NPs, the increase of phenanthroline decreased the diameter of europium oxysulfide NRs.

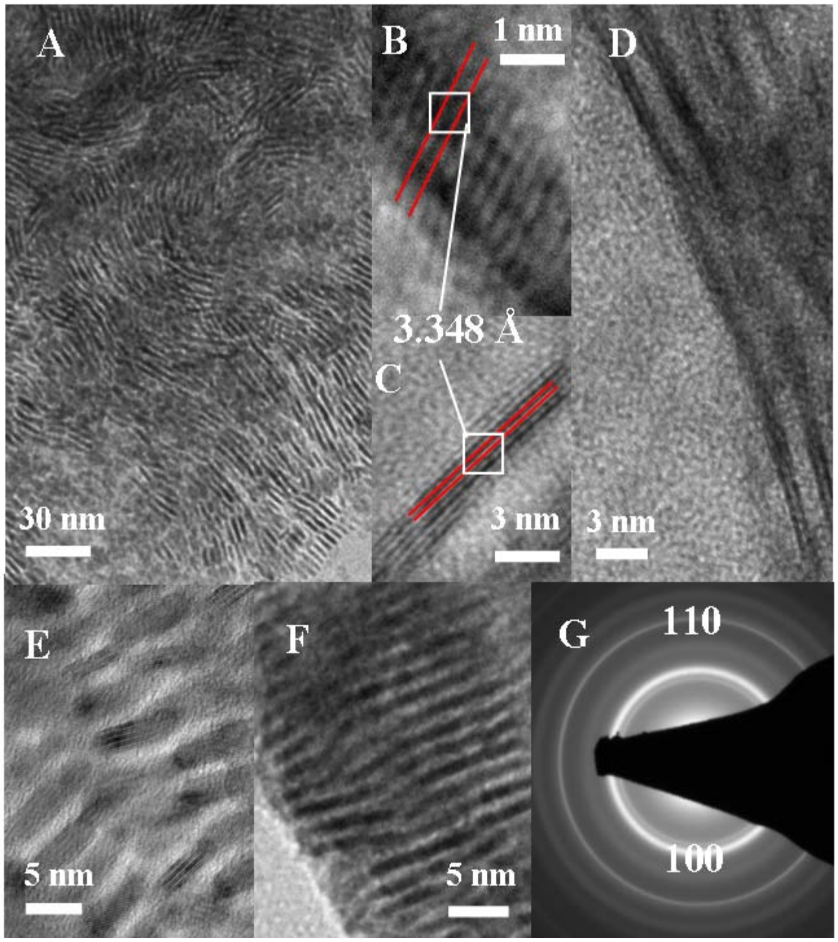

Figure 2.6: (a-e) TEM images of $Eu_2O_{2-x}S$ NRs with different diameters and different aspect ratios: (A) D=3.5 nm and AR=5, (b-c) D=3.0 nm and AR=5, (d) D=1.5 nm and AR=20, and (e) D=3.0 nm and AR=3. (f) TEM image of Eu_2O_3 NRs with D=1.5 nm and AR=10. (g) Selected area electron diffraction patterns of $Eu_{2-x}O_2S$ NRs with D=3.5 nm and AR=5.

A plausible explanation for this is that the hot injection induced the rapid nucleation and that the increased amount of phenanthroline facilitated the rapid 1D growth of europium oxysulfide nuclei into long NRs with small diameters. Phenanthroline likely lowered the activation energy associated with the formation chemical reaction of europium oxysulfide NRs since Eu_2O_3 NRs were formed instead of europium oxysulfide NRs in the absence of phenanthroline. The formation of europium oxysulfide NRs with phenanthroline could possibly be facilitated by anion exchange between S and O, followed by recrystallization. This mechanism has been observed and well explained by the various reports.[91-93] The TEM image of Eu_2O_3 NRs is shown in Figure 2.7.

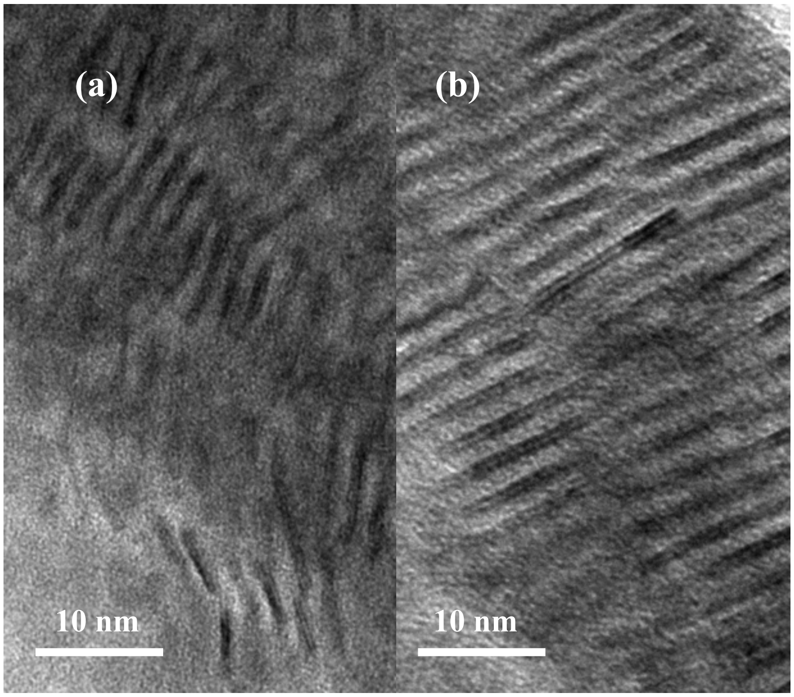

Figure 2.7: (a) TEM image of $Eu_2O_{2-x}S$ NRs with a diameter of 1.5 nm and an aspect ratio of 5. (b) TEM image of Eu_2O_3 NRs with a diameter of 1.5 nm and an aspect ratio of 10.

The lattice spacings shown in Figure 2.6, correspond to the (100) lattice plane of the hexagonal europium oxysulfide. The SAED pattern in Figure 1G show pronounced diffractions patterns from (100) and (110) planes. The relative intensity of the (100) ring suggests that this is the preferred orientation for growth of the NRs. These results are consistent with the lattice spacing in Figure 2.6.

XRD spectra of the colloidal $Eu_2O_{2-x}S$ NRs were taken to assess their crystallinity. As shown in Figure 2.8, five peaks were observed for the NRs, which were indexed to be (100), (101), (102), (110), and (200) lattice planes based on the JCPDS file (# 26-1418) of hexagonal europium oxysulfide.

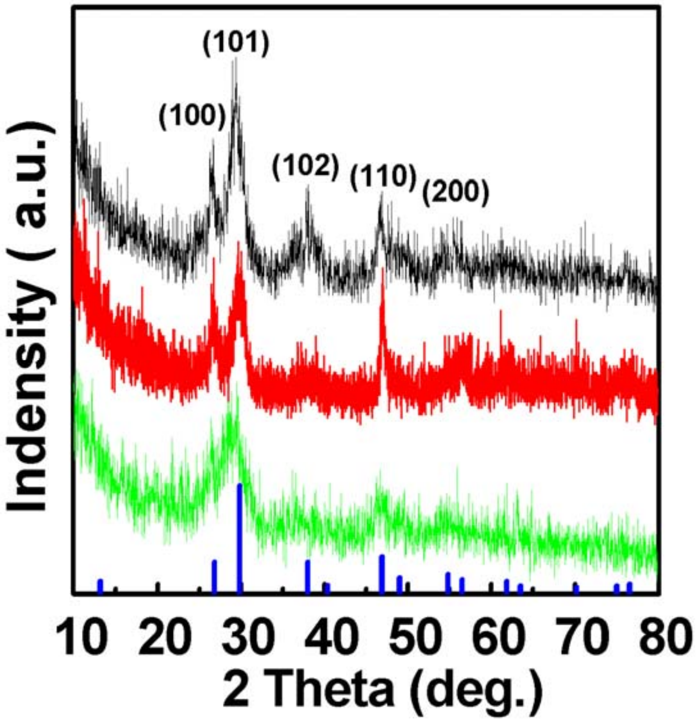

Figure 2.8: XRD spectra of europium oxysulfide NRs with a fixed AR of 5 and different diameters: D=3.5nm (top, black), D=3.0 nm (middle, red), and D=1.5nm (bottom, green). Primary peak locations for crystalline $Eu_{2+x}O_2S$, provided by the JCPDS file (# 26-1418) of hexagonal europium oxysulfide, are indicated for clarity (bottom, blue).

This means the NRs were well crystallized with a hexagonal structure. As the diameter decreases, the half width of the major peak (101) increases, which is consistent with Scherrer's equation. Energy dispersive X-ray analysis (see Figure 2.9) was performed on the samples using a Hitachi S-4200 Scanning Electron Microscope, which confirmed the elemental composition of the NRs. Based on both EDS and XRD, the chemical composition of the synthesized NRs was confirmed to be $Eu_{2+x}O_2S$ with x=0.11 ± 0.3 for all the NRs.

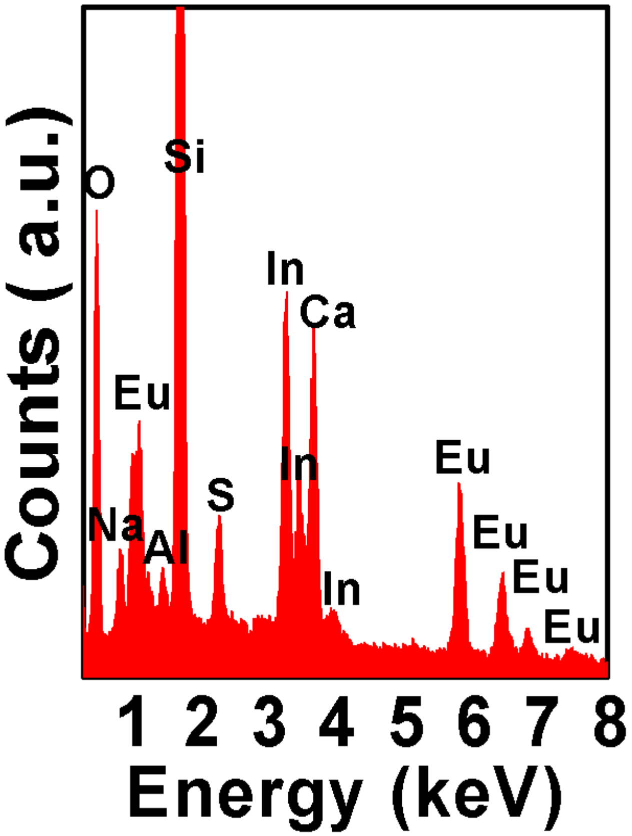

Figure 2.9: EDS spectrum of europium oxysulfide NRs with a fixed AR of 5 and a D=3.5nm.

2.4 Colloidal synthesis of Te nanoparticles

2.4.1 Experimental details

All synthetic steps were carried out in nitrogen filled, moisture free glove box at room temperature.[56] In a typical synthesis, 3.5 mL oleic acid (OA) was dissolved in a mixture solution of 15.0 mL ethylene glycol (EG) and 4.0 mL triethanolamine (TEA) under vigorous stirring. 2.0 mL of 0.1 M solution of Na_2Te in EG was added drop-wise into the vigorously stirred OA solution. The resulting black-colored Te nanoparticles were separated by centrifugation, were washed with methanol, and were stored in methanol for further eletrophoretic depositions and measurements. This procedure produced the two size distributions described in the main text: 1.5 nm and 27.5 nm Te nanoparticles. To achieve other binary size distributions, one can modify the concentration of Te precursor, or change synthetic temperatures.

2.4.2 Characterization techniques

A Bruker Tensor 27 Fourier Transform Infrared Spectroscopy (FT-IR) was employed to measure the liganding of Te nanoparticles after cleaning. Atomic force microscope images were collected using a Nanoscope III Atomic Force Microscope.

2.4.3 Results and discussion

Tellurium nanoparticles (NPs) were synthesized in a one-step fashion at room temperature by using sodium telluride (Na_2Te) as a precursor and oleic acid (OA) as an oxidizing agent in the presence of triethanolamine (TEA) dissolved in ethylene glycol (EG). Since all employed chemicals are environmentally friendly, this synthetic approach can be accomplished by green chemistry. Further, the synthesis yielded two distinct NP size distributions simultaneously: one diameter centered at 1.5 ± 0.5 nm and one centered at 27.5 ± 5 nm. We also discovered that the NPs were well ligated, which facilitates both their suspension in organic solvents. This electric field-assisted casting scheme allowed us to fabricate films of Te NPs of thicknesses ranging up to several hundred nanometers.

In the synthesis, Na_2Te was highly possibly oxidized by OA due to the oxidative capacity of its carboxylic acid group and the fact that all the synthetic steps were carried out with anhydrous chemicals in an oxygen-free glove box. Oxidized Te immediately nucleated into 1.5 nm Te NPs, some of which grew into sizes as large as 30 nm. Carboxylic acid oxidation balances the nucleation and growth steps, facilitating the formation of nuclei to promote surface reaction-limited kinetics at a low temperature once the nucleation of Te had completed. The Te nuclei grew into 27.5 nm NPs possibly through classical Ostwald ripening either by: a) the bulk phase diffusion of Te from the dissolution of 1.5 nm Te NPs due to their higher dissolvability compared to larger size NPs; or b) the rapid diffusion and recrystallization of multiple Te nuclei shortly after their formation. The growth showed a rapid kinetics in our synthesis, which reached equilibrium for both NP sizes right after injection of Te precursor into OA solution. Both 1.5 nm and 27.5 nm NPs were ligated by TEA, as confirmed by Fourier transform infrared spectroscopy (see Figure 2.10). The surface ligand reduced the surface tension of both NPs and, thus, prevented 1.5 NPs from completely dissolving and maintained the balance between the two sizes.[94-96] Hexagonal Te NPs (space group $P3_121$, no. 152) were well ligated by TEA throughout the synthesis, passivating the primary [001] growth orientation observed in nanowires and, thus, facilitating the uniform growth of the material along all lattice orientations.

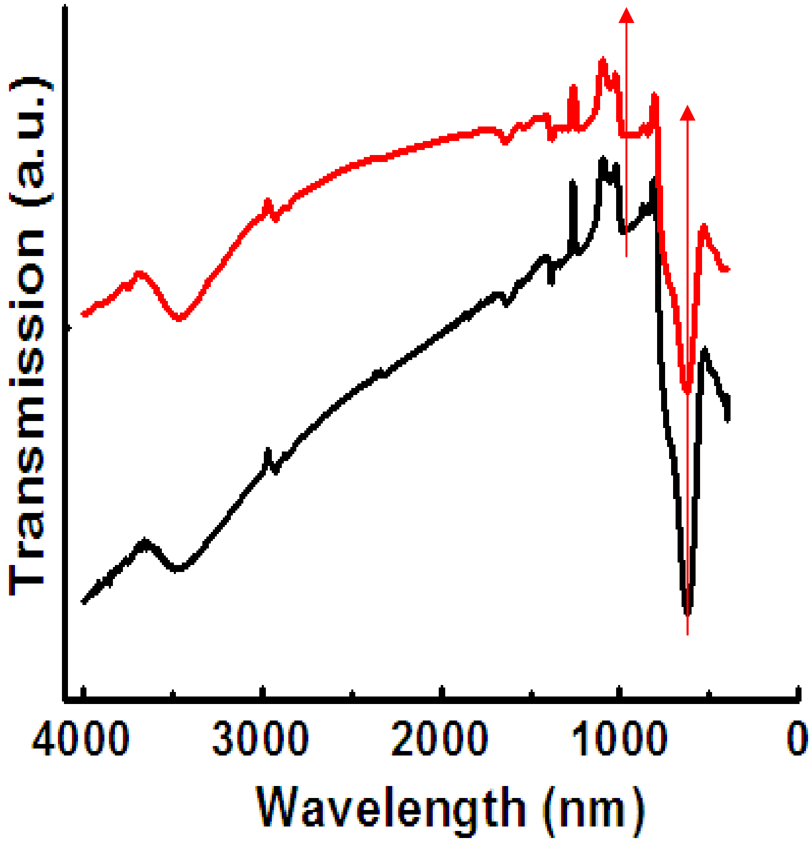

Figure 2.10: FTIR spectrum of Te nanoparticles cleaned once (black, bottom) and twice (red, top). The primary peaks correspond to triethanolamine. Peaks identification: O–H vibration, 3500-3000 cm^{-1}; C–H stretching band, 3000-2800 cm^{-1}; C–C and C–H bending, 1460-1130 cm^{-1}; C–O and C–N stretching, 1100-890 cm^{-1}; C–C–O vibrations, 880-690 cm^{-1}. Physisorbed and chemisorbed water, 3500 to 3000 cm^{-1} and 1800-1500 cm^{-1}. Red arrows demarcate the decreases in FTIR peaks.[56]

Since the surface ligands contain –OH groups, Te NPs tended to aggregate so that NPs with the 2 diameters were not well separated after synthesis. We found that the number of times that methanolic suspensions of the NPs were cleaned, which comprised a sonication step followed by a centrifugation step, determined how well we could separate the two NP size distributions (Figure 2.11a-b). As the figure demonstrates, the cleaning process allowed us to precipitate the larger NPs while keeping the smaller ones in suspension. The cleaning procedure removes a portion of the surface ligands, asconfirmed by a decreasing FTIR signal for the C–C–O vibrations as well as C–O and C–N stretching as the number of cleaning times increased (see Figure 2.10), weaken the van der Waals attraction between NPs, and eventually make smaller NPs dispersed in solvent. For example, 1.5 ± 0.5 nm NPs and 27.5 ± 5 nm NPs were optimally isolated by cleaning the samples three times, verified later by a Philips CM 200 Transmission Electron Microscope operated at 200 kV and X-ray diffraction. As seen in Figure 11c, 1.5 nm Te NPs were quasi-spherical with a slight elongation, which can be explained by the total number of hexagonal Te unit cells within a single 1.5 nm NP (approximately five). As-dissolved Te from these small NPs diffused into other NPs through collision-based Ostwald ripening to grow into 27.5 nm Te NPs, the volume of which is approximately 8000 times that of 1.5 nm Te NPs. Despite aggregation, some individual 27.5 nm spherical Te NPs can be seen in the TEM image (Figure 2.11b). The increased aggregation as Te NPs grew implies that the liganding might be a dynamic process and interacted with NP growth until the growth of all lattice facets reached equilibrium.

XRD profiles of the colloidal Te NPs were taken to assess the crystallinity of Te NPs (Figure 2.11d). The XRD data of 27.5 nm Te NPs confirmed the presence of the primary Te crystal orientations. This demonstrates that the materials were well crystallized with hexagonal structure with space group of $P3_121$. By evaluating the full width at half-maximum of the (101) peak and applying Scherer equation analysis, we determined the diameter of the larger NPs to be 28.3 ± 2.3 nm. This size was consistent with that assessed from TEM images.

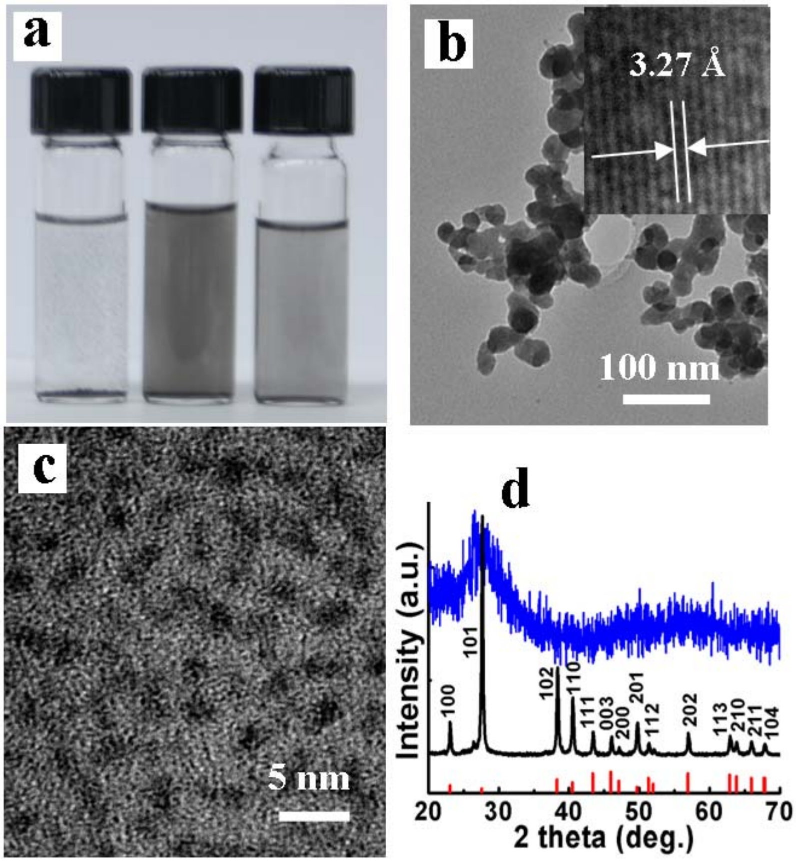

Figure 2.11: (a) Suspensions of Te NPs in methanol cleaned (left to right) once, twice, and thrice. (b) HTEM image of 27.5 nm Te NPs. Inset: HTEM image of (101) lattice spacings. (c) HTEM image of 1.5 nm Te NPs. (d) XRD spectra of 1.5 nm (top, blue) and 27.5 nm (middle, black) Te NPs. Primary peak locations for crystalline Te, provided by the JCPDS file (# 36-1452) of hexagonal tellurium, are indicated for clarity (bottom, red).[56]

2.5 Colloidal synthesis of Te nanrods

2.5.1 Experimental details

Te NR/NP mixtures were synthesized using a colloidal method similar to the one we recently reported.[56] All the samples were synthesized at room temperature in a moisture-free glove box filled with nitrogen. In the synthesis, oleic acid and TEA were dissolved in ethylene glycol, and the resulting solution was then mixed with Na_2Te solution in ethylene glycol under vigorous stirring. The as-synthesized NCs were then cleaned by centrifugation and suspended in methanol after cleaning.

2.5.2 Characterization techniques

Scanning electron microscope (SEM, Hitachi S-4200) and transmission electron microscope (TEM, Philips CM 200 at 200 kV) were used to characterize the size and shape of the Te NCs. Electron diffraction (ED) was used to measure the crystallinity of the Te NCs and Fourier transform infrared spectroscopy (FTIR) measurements were conducted to confirm their surface ligand information.

2.5.3 Results and discussion

With 4 mL or more TEA, Te NPs with binary size distribution were synthesized, as previously reported.[56] And here, we found that without TEA only ~100 nm irregularly-shaped Te NPs were synthesized, and that with up to 3 mL of TEA, more TEA resulted in more NRs in the NR/NR mixtures, as shown in the SEM images in Figure 2.12. With TEA, the NPs were ~29.5 ± 4.5 nm in diameter, and the NRs were ~103.5 ± 11.0 nm in diameter and 800.0 ± 50.0 nm in length. Since no obvious oriented attachment between individual nanocrystals was observed in the synthesis, the NPs and NRs synthesized with or without TEA, were highly possibly grown via Ostwald ripening through rapid bulk phase diffusion and recrystallization of Te nuclei NPs. With TEA, the growth of Te NCs tended to reach reaction equilibrium with a steady pace, resulting in a uniform size distribution. Without TEA surfactant, the dissolution and diffusion of Te nuclei formed at the initial stage of the synthesis were abrupt and tended to facilitate the rapid formation of NCs. This abrupt rapid growth was evidenced by the irregular shape and large size of Te NPs, as shown in Figure 2.12b.

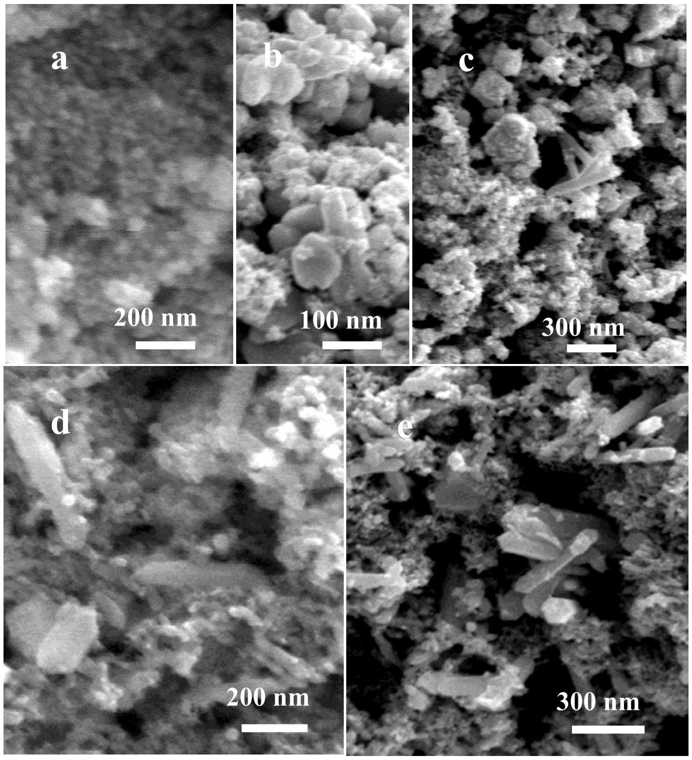

Figure 2.12: SEM images of Te NCs synthesized with 4.0 mL (a), 0 mL (b), 1.0 mL (c), 2.0 mL (d) and 3.0 mL (e) TEA.

Organic agents, especially those that are served as surfactants used in a colloidal synthesis, are of essential significance for controlling the shape and size of resulting NCs. For example, 1D gold NCs were synthesized with CTAB and DTAB as surfactants.[97-98] Another example is that adding phenanthroline to the reaction system in EuTe NC synthesis directly produced crystalline EuTe nanospindles.[87] In our synthesis of Te NR/NP mixtures, the ligand information was studied with FTIR for high NR-to-NP ratio samples as well as pure NP samples. Te NCs synthesized with TEA were well ligated by TEA, as confirmed by Figure 2.13. Adding 3.0 mL or less TEA into the reaction system facilitated the growth of Te NRs.

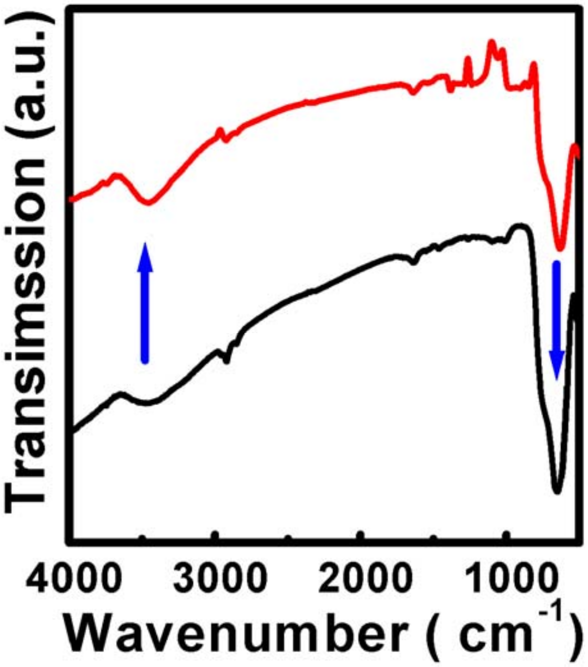

Figure 2.13: FTIR spectra of Te NCs synthesized with 4.0 mL (red), and 3.0 mL (black) TEA. Blue arrows demarcate the increases in FTIR peaks.

Furthermore, as shown in Figure 2.13, compared to the FTIR spectrum of Te NPs synthesized with 4 mL TEA, the peak of OH vibration (3500-3000 cm^{-1}) for Te NR/NP synthesized with 3 mL TEA is less pronounced while its peak of C-C-O vibration (880-690 cm^{-1}) is much more pronounced. The obvious change of liganding groups from OH to C-C-O could induce the change of passivation energy of TEA on different lattice planes of Te NCs. As a result, the growth along some lattice orientations were preferred to that along others with more passivation, and the growth along a certain lattice orientation produced facilitated the anisotropic growth of Te NCs.[99] This surfactant-change-induced 1D growth was confirmed by the TEM image and electron diffraction pattern of Te NRs (Figure 2.14), both of which were indexed to the (100) lattice plane of Te crystal. The anisotropic growth of Te NRs can be terminated by the absence of TEA or a large amount (> 3.0 mL) of TEA.

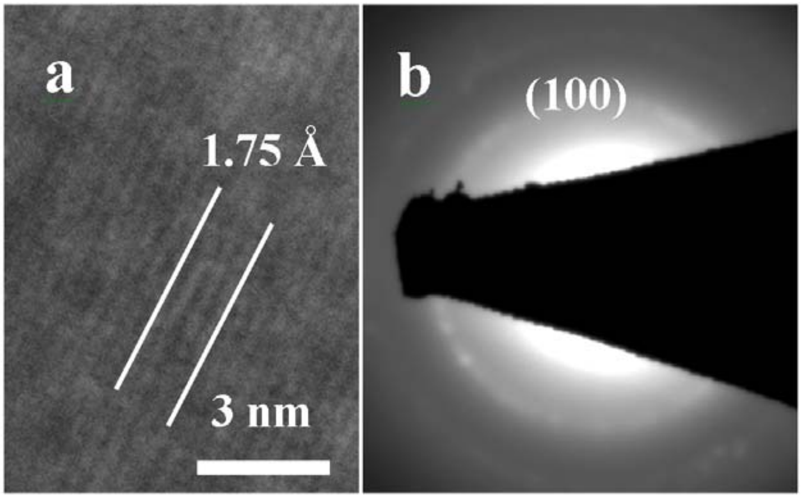

Figure 2.14: TEM image (a) of (100) Te NR and electron diffraction (b) of the Te NCs.

2.6 Summary

In summary, colloidal EuTe NPs have been synthesized for the first time, and the magnetic properties of EuTe NPs have been introduced. This facile room temperature colloidal synthesis helps to overcome the long-existing challenges of synthesizing other rare-earth chalcogenides. The procedure also presents the opportunity of employing

EuTe NPs in magnetic, photovoltaic and other optical applications. Ultra-thin europium oxysulfide nanorods were synthesized by using hot injection with the simple precursor europium oleate. The diameters and aspect ratios of the NRs were finely controlled by the injection rate and the amount of phenanthroline. Colloidal Te NPs with two uniform size distributions have also been synthesized in a one-step green chemistry method at room temperature. The surface ligands allow their isotropic growth, and give rise to net surface charges in methanol suspension.

CHAPTER III

OPTICAL AND MAGNETIC PROPERTIES OF EuTe AND Eu_2O_2S NANOCRYSTALS

3.1 Introduction

The optical and magnetic properties of NCs are closely correlated with the size of the NCs. The absorption peaks of these NCs typically show blue shifts in the wavelengths of visible range as the size of NCs decreases if these NCs absorb visible light. The blue shifts are due to the enhanced quantum effects. For magnetic NCs, as their size decreases, the formation energy of multiple magnetic domains in a magnetic material increases rapidly, and the magnetic material starts to form single-domain magnetic material. For ferromagnetic materials, anisotropy energy increases with a decrease in NC size, which causes a higher coercivity in the magnetization-versus-applied-field measurements.[16] As the size continues to decrease, more energy is required for the parallel-aligned spins to switch either up or down orientations, and, thus, the anisotropy energy decreases. Besides, as the size of NCs decreases, the increased surface-to-core atomic ratio, and increased uncompensated spins cause the change in magnetization and ordering temperature of a magnetic material.[72] With these changes, ferromagnetic NCs become superparamagnetic, and antiferromagnetic NCs behave superantiferromagnetically due to the realignment of magnetic spins in these materials. As a magnetic material behaves superparamagnetically or superantiferromagnetically, its classical ordering transition is typically masked by the enhanced uncompensated moments in the magnetization-versus-temperature measurements.[66, 68] As the magnetic transition is not obvious, the evaluation on the ordering temperature of a magnetic material using an appropriate model becomes necessary. That is because the research helps to understand the intrinsic magnetic properties of the material, and the findings of the research enhance the applicability of the NCs by adjusting the ordering temperature of the NCs to a practical temperature range.[72]

Besides the size-dependent physical properties, as the size of NCs becomes small enough, the increased astoichiometry can also cause many property transitions, such as diamagnetic-to-magnetic, and insulating-to-metallic transitions. These transitions allow one to explore new properties of materials, and, thus, greatly broaden the applications of the materials.

In this chapter, the optical and magnetic properties of EuTe and Eu_2O_2S nanocrystals are analyzed and discussed. The magnetic properties of EuTe nanoparticles were easured by vibrating sample magnetometry with a Quantum Design Physical Property Measurement System, and then studied via Gilles' model, a non-Langevin model. Calculations are carried out to study the enhancement of T_N of EuTe NPs. The size-dependent optical and magnetic properties of Eu_2O_2S nanorods are also investigated.

3.2 Experimental details

3.2.1 Materials and methods

EuTe NPs were synthesized via a colloidal method that was recently reported.[87] 5.5 nm and 7.3 nm EuTe NPs were chosen in this study to investigate how the magnitudes of magnetic moments and ordering temperatures of EuTe crystal vary on the nanoscale compared to bulk EuTe.[87] Eu_2O_2S nanorods were synthesized using the colloidal method as described in Chapter II (Section 2.3). The structure of 5.5 nm EuTe NPs, confirmed by EDS and FTIR, is shown in Figure 3.1. The EuTe and Eu_2O_2S NCs were suspended in methanol for absorption and photoluminescence measurements. For the magnetic measurements, ~10 mg EuTe and Eu_2O_2S NCs were filled into diamagnetic plastic capsules and then placed onto the sample holder for magnetic measurement. The NPs were suspended in anhydrous methanol in moisture-free glove box before and after magnetic measurements.

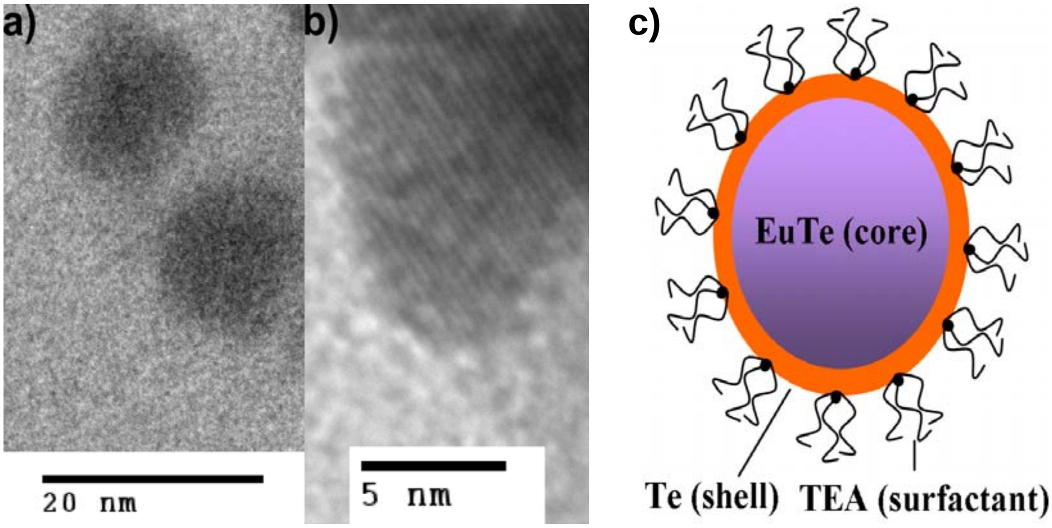

Figure 3.1: (a) TEM image of 5.5 nm EuTe NPs. (b) Higher resolution image of a NP. (c) Schematic of the structure of EuTe NPs, including the oxidized, metallic Te surface coating the EuTe core.

3.2.2 Characterization techniques

The UV-Vis spectra were recorded with a Varian Cary 5000 UV-VIS-NIR spectrophotometer. Photoluminescence spectroscopy measurements were performed on the Eu_2O_2S NRs, suspended in hexane, with a Fluorolog-3 spectrophotofluorometer, using the 254 nm line of a 450 W xenon lamp as the excitation source. Field-cooled and hysteresis magnetic measurements were conducted by vibrating sample magnetometry with a Quantum Design Physical Property Measurement System for EuTe and Eu_2O_2S NCs.

3.3 Results and discussion

3.3.1 EuTe nanoparticles

Figure 3.2 shows the absorption spectra of EuTe NPs and NSs dispersed in methanol. There were two peaks for both EuTe NPs and NSs; the low-energy peak corresponded to $4f^7$–$4f^6$ (^7F_J) 5d (t_{2g}) transition of europium electrons, and the high-energy one, around 200-300 nm, corresponded to the transitions from 4f levels to 5d states and the charge transfer between Eu(II) and Te(II) (Figure 3.2 (Inset)). The strong absorption at 200 nm was due to the intense aborption of methanol as solvent.

The low-energy absorption peak blue shifted from 565 nm (2.2 eV) to 360 nm (3.4 eV) as the NP size decreased from 7.3 nm to 5.5 nm, which could be due to quantum confinement effects. Interestingly, the high energy absorption peak of EuTe nanospindles (NSs) appeared to be much stronger than the corresponding peak for EuTe NPs. This was likely due to a relative blue shift of the high-energy 4f-electron in the zero-dimensional, quantum-confined NPs (at ~220 nm) versus in the one dimensional NSs (at ~250 nm).

The increased length of the EuTe NSs (~20.4 nm) red-shifts their absorption peak relative to the NPs.

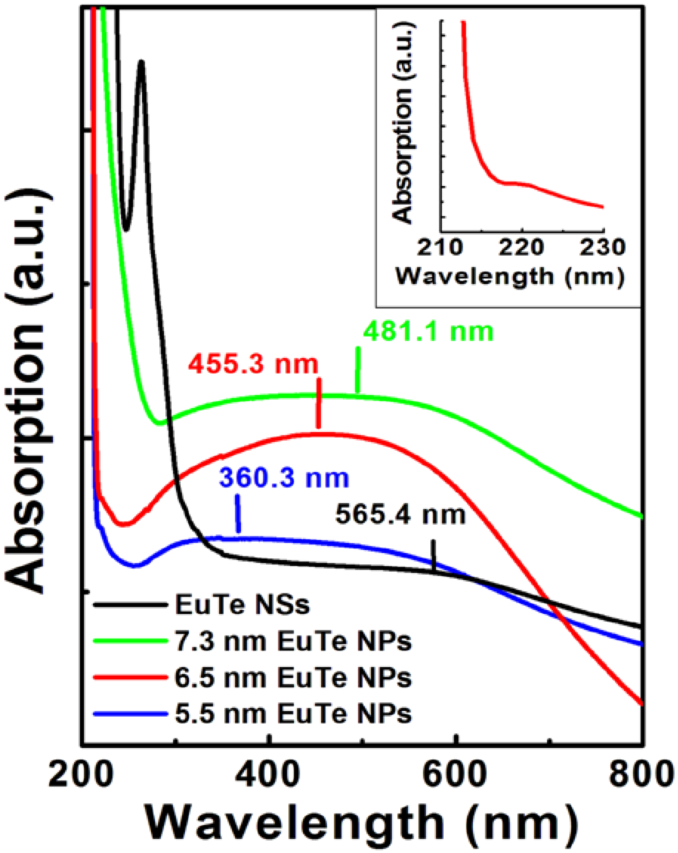

Figure 3.2: Absorption spectra of EuTe NPs and NSs in methanol. Insert) Absorption of 6.5 nm NPs exhibiting transitions from 4f levels to 5d states and the charge transfer between Eu(II) and Te(II).[87]

Field-cooled magnetization and magnetization hysteresis measurements were conducted by vibrating sample magnetometry with a Quantum Design Physical Property Measurement System. To study the thermal variation of the magnetization that originates from the classical and uncompensated spins, we employed 0.1 T as the ambient field for the field-cooled magnetization measurement. No antiferromagnetic-to-paramagnetic transition was observed as the temperature increased from 2 K to 50 K. The absence of a transition suggested the presence of a superantiferromagnetic ordering state, as described by previous report.[87]

To analyze the classical and uncompensated magnetizations of the EuTe NPs, Gilles' non-Langevin model was employed, as shown in Eq. 3.1. The second term on the right of Eq. 3.1 correlates uncompensated moments $\mu_{nc}(T)$ with uncompensated magnetization. $G(x)$ in this expression, is a non-Langevin function, as expressed in Eq. 3.2. For the hysteresis measurement at 2 K, the experimental data and the fitted data, based on Gilles' model for the 5.5 nm EuTe sample, exhibited notable agreement across much of the field range, as shown in Fig. 3.3.

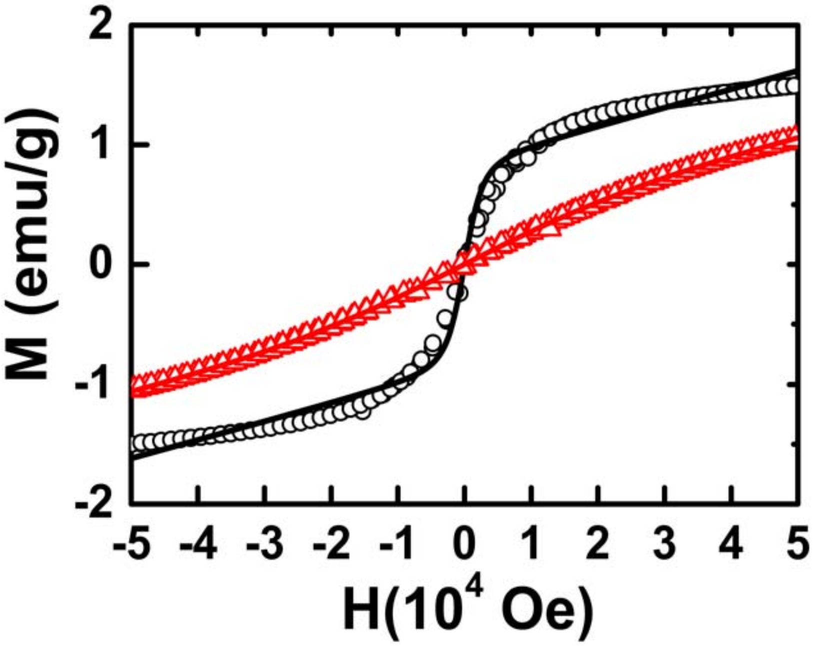

Figure 3.3: Experimental (open symbol) and theoretical (solid line) values of the magnetization as a function of magnetic field for 5.5 nm EuTe NPs at 2 K (black circle and line) and 12 K (red triangle and line).

The mismatch between the data and the fit can be attributed to dominating uncompensated spins at low magnetic fields and dominating superantiferromagnetism at higher magnetic fields. At 12 K, the fitted and experimental hysteresis curves exhibit more substantial agreement than that observed at 2 K.[66, 68]

$$m_{nc}(H,T) = \chi_{AFM}(T)H + \int_{V_{\min}}^{V_{\max}} \frac{dV}{V} f(V)\mu_{nc}(V,T)G(\frac{\mu_{nc}H}{k_B T}) \tag{3.1}$$

$$G(x) = \frac{1}{2}\int_0^{\pi} d\theta \sin\theta \cos\theta \tanh(x\cos\theta) \tag{3.2}$$

The temperature dependence of the uncompensated moments is expressed by Eq. (3), where α is a constant, and $\mu_{nc}(0)$ is the uncompensated moment at T = 0 K.[66] We can employ this expression to extract T_N from our temperature-dependent magnetic data; the intercept of the x-axis of a graph of the uncompensated magnetic moment, $\mu_{nc}(T)$, as a function of temperature is T_N.

Fig. 3.4a shows a graph of the uncompensated moments of 5.5 nm and 7.3 nm NPs as functions of temperature, as calculated using Eq. 3.3.[66] The T_N of 5.5 nm and 7.3 EuTe NPs were determined to be 16.5 K and 27.0 K, respectively.

$$\mu_{nc}(T) = \mu_{nc}(0)(1 - \alpha T^2) \tag{3.3}$$

The observed enhancement of T_N contradicts the typical and expected decrease in the ordering temperature, as reported for other magnetic NPs.[16, 72] Strain-induced lattice distortion can change the nn magnetic exchange interaction, J_1, and the nnn exchange interaction, J_2, resulting in the change in T_N.[24] For example, the Néel temperature of EuTe films sandwiched in PbTe layers increased to ~12.8 K, recognizably higher than T_N = 9.6 K for bulk EuTe.[26] The observed enhancement was attributed to compressive strain in the EuTe film resulting from the lattice mismatch between the EuTe and PbTe crystals.[100] We believe that a similar argument can be made for the core-shell structure of EuTe nanoparticles.

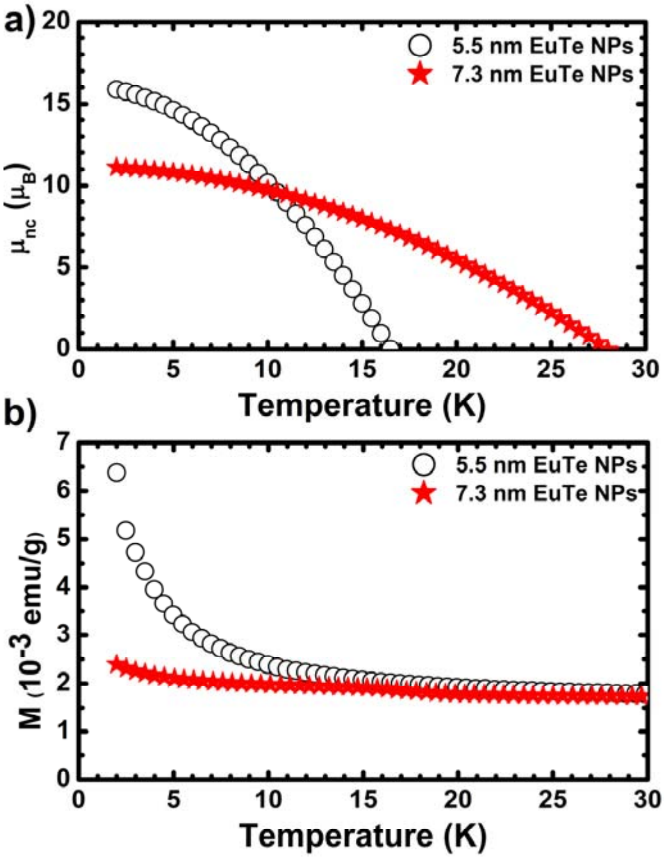

Figure 3.4: (a) A graph of the uncompensated spin moment (mnc) as a function of temperature in a 0.1 T magnetic field. (b) a graph of the field-cooled magnetization as a function of temperature, also within a 0.1 T field. The black, open circles represent 5.5 nm NPs, and the red, solid stars represent 7.3 nm NPs.

As shown in Fig. 3.5, the (100) surface of EuTe (FCC crystal) and the (001) surface of Te (HCP crystal) are illustrated. The (100) plane of EuTe yielded a stronger diffraction signature in the XRD experiments.[87] At the core-shell interface, the mismatch between EuTe and Te is as large as 4.5 % and 17.3 % in x and y direction, respectively. Such a mismatch strongly suggests that the interface EuTe surface must be under compression.

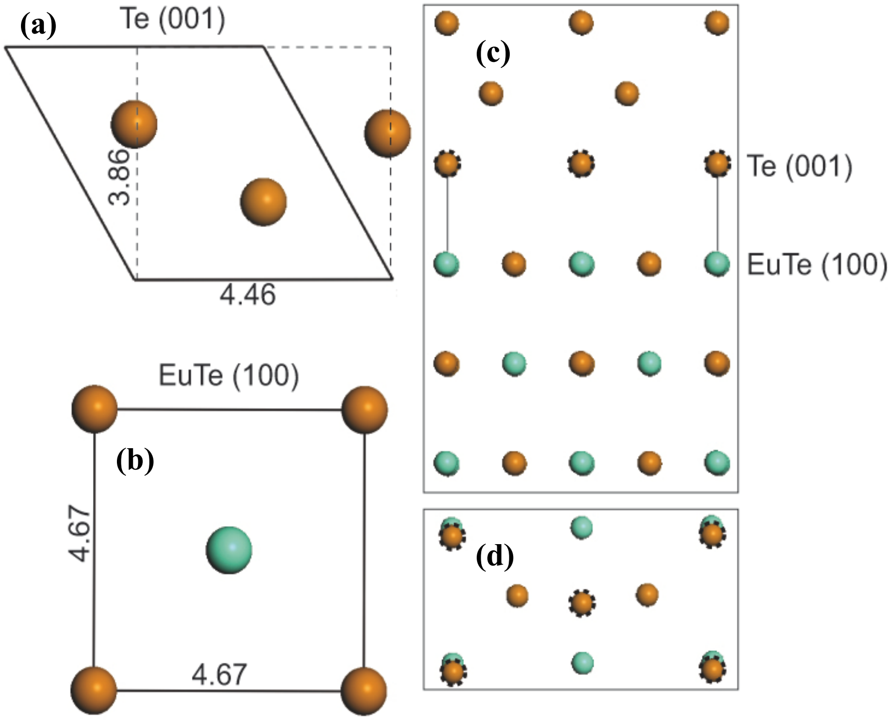

Figure 3.5: Strain-induced lattice distortion due to lattice mismatch between (001) Te and (100) EuTe lattice planes. (a) (001) Te lattice plane, (b) (100) EuTe lattice plane, (c) lattice mismatch between (001) Te and (100) EuTe planes, and (d) plan view of lattice mismatch between (001) Te and (100) EuTe planes.

To explore whether such a compressive strain could yield increased T_N, we sought the magnitude of the nnn exchange constant J_2. An empirical expression relating the exchange constant to the magnitude of the Néel temperature in EuTe is provided in Eq. 5.[36]

From this expression and the T_N, ascertained from Figure 3.4, we calculated the J_2 values to be -0.49 for 5.5 nm NPs and -0.80 for 7.3 nm NPs. Next, we applied Eq. 3.4 and Eq. 3.5 to determine the extant lattice strain for the EuTe core of the two NP diameters, where n = 10.4, and r_0 was the bulk Eu-Eu interatomic distance, and J_0 was the bulk EuTe exchange constant.

$$J(r) = J_0\left(\frac{r}{r_0}\right)^{-n} \tag{3.4}$$

$$T_N = 1.22 - 27.57\left(J_2 / k_B\right) \tag{3.5}$$

Employing $J_0 = J_2$, the compressive lattice strains, induced by the small diameter of the EuTe NPs and the corresponding lattice mismatch between Te and EuTe, were calculated to be 4.2 % for 5.5 nm NPs and 8.7 % for 7.3 nm NPs. These values are remarkable, given that a 5% compressive lattice strain, induced by high applied pressure, was observed to induce an AFM-FM transition for EuTe, with an enhanced Curie temperature of 28 K.[73] Therefore, we reasonably conclude that significant compressive lattice strain can lead to an enhancement of the Néel temperature, shifting the temperature up by 6.7 K for 5.5 nm EuTe NPs and by 17.2 K for 7.3 nm EuTe NPs.

Different from the pressure-induced T_N enhancement, enhancements due to the interface binding between EuTe and Te induces compressive strain within the EuTe crystal and results in a decrease in the surface energy for the EuTe NPs. With reduced surface energy, a larger thermal energy is required for the antiferromagnetic-paramagnetic transition to be realized, which enhances the Néel temperature of EuTe NPs.[72] As shown in Fig. 3.5, at the EuTe/Te interface, Te atoms in the shell passivate the uncompensated bonds of the underlying EuTe crystal by forming additional EuTe-Te bonds. This bonding reduces the surface energy of EuTe NPs. The compressive lattice strain at the EuTe/Te interface and the surface energy reduction, due to the interface binding between EuTe and Te, result in the observed enhancement of T_N for the EuTe NPs.

The Néel temperature can possibly increase or decrease as the NP size is larger than 7.3 nm or smaller than 5.5 nm due to the fact that net compressive lattice strain doesn't monotonously increase or decrease with size.

3.3.2 Eu_2O_2S nanorods

The emission spectra of the NRs are shown in Figure 3.6. The observed peak is possibly due to ^5D_J (J=0)-^5D_J (J=1) or ^5D_J (J=0, 1)-^7F_J (J=0-4) transitions of divalent europium. The peak is markedly broader than the sharp luminescence features of stoichiometric, bulk Eu_2O_2S. Similar PL broadening was observed in room-temperature measurements by Zhao *et al* for colloidal europium oxysulfide nanoplates and NRs, but was absent for bulk Eu_2O_2S.[34-35] They argued that the increased broadness was due to the lower crystal field symmetry on the surface of the NRs with ultra-small diameters; however, astoichiometries in the crystal is equally plausible.[34-35] For our NRs, quantum confinement was observed and enhanced when the diameter of 1D NCs decreased; this was confirmed by the obvious blue shift of the peak from 445 to 410 nm as the diameter of the NRs decreased from 3.5 to 1.0 nm. The less pronounced peaks from 600 to 700 nm are due to $^5D_0$-^7F_J (J=2-4), which is consistent with Zhao et al's report.

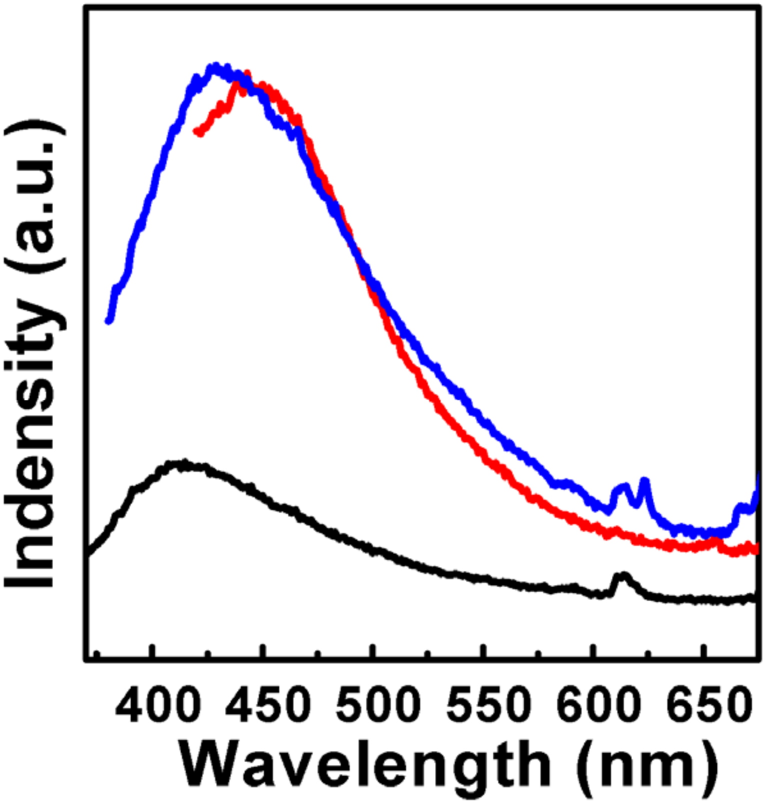

Figure 3.6: Room temperature fluorescence emission spectra of europium oxysulfide NRs with a fixed AR of 5 and different diameters: D=1.0 nm (black), D=1.8 nm (red), and D= 3.5 (blue).

Zero-field-cooled (ZFC) and field-cooled (FC) magnetization measurements as well as magnetization versus applied field measurements on 3.5 nm $Eu_{2+x}O_2S$ NRs with an AR of 5 were conducted using vibrating sample magnetometry, with a Quantum Design physical property measurement system. In the measurements, magnetic moments were observed from the NR samples. The observed magnetic properties are interesting because stoichiometric europium oxysulfide in its bulk form is a typical diamagnetic material. A plausible explanation for the magnetic response is that the small NR diameter giving rise to a high ratio of surface-to-core atoms induces the shift in the stoichiometry, and causes a reorientation of surface and core spins in the NRs, which could give rise to a net magnetization.[101] As shown in Figure 3.7, the ZFC and FC measurements also demonstrates a magnetic transition; the plot of inverse susceptibility (χ^{-1}) *versus* temperature (Inset of Figure 3.8) yields a Curie transition at 15.8 K.

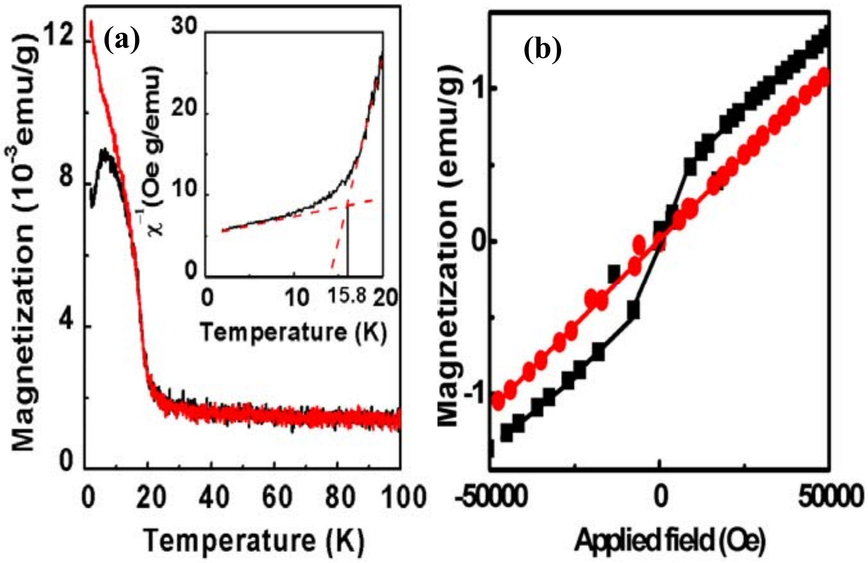

Figure 3.7: ZFC and FC (at 70 Oe) curves of europium oxysulfide NRs (D=3.5 nm and AR=5) from 100 K to 2 K. Inset: field-cooled inverse magnetic susceptibility versus temperature. (D) Magnetization versus applied field curve of europium oxysulfide NRs (D=3.5 nm and AR=5) from -5.0 T to 5.0 T at 2 K (black) and 30 K (red).

The normalized magnetization of the NRs is on the order of 10^{-3} emu/g. No saturation was observed in the magnetization vs. magnetic field data from 2 K to 30 K, as shown in Figure 3.8. The smallness and the unsaturated feature of the magnetization present in the NRs could be due to the small extent of astoichiometry, as confirmed by EDS.

3.4 Summary

In summary, the colloidal EuTe and Eu_2O_2S NCs showed size-dependent optical properties. The enhancement of TN was achieved on antiferromagnetic EuTe NPs by introducing compressive lattice strain at the EuTe/Te interface. Ferromagnetic and superparamagentic properties of the astoichiometric Eu_2O_2S NCs were observed for the NRs for the first time.

CHAPTER IV

GROWTH MECHANISM OF ONE-DIMENSIONAL NANOCRYSTALS: ORIENTED ATTACHMENT AND VAN DER WAALS INTERACTION

4.1 Introduction

In colloidal chemistry, the size and morphology of NCs are closely correlated with the growth mechanism of these NCs. Improved understanding of the growth mechanism leads to better control of the synthesis of the NCs, which, in turn, helps produce high-performance properties of the NCs with controlled size and shape. To achieve improved optical and magnetic properties, fine tuning of the size and shape of NCs has become a main research focus in the nanoscale research community. Recent research efforts have demonstrated that changes in the size and/or the shape of EuX nanocrystals, can result in notable changes in their optical and magnetic characteristics. The predominance of synthetic methods for EuX nanocrystals has focused on spherical or quasi-spherical particles; for example, Hasegawa et al, Regulacio et al, Zhao et al, and He et al have reported a variety of synthetic routes towards the production of spherical EuS, EuSe, and EuTe NCs.[19, 87, 102] Burgeoning interest in the synthesis of one dimensional (1-D) EuX nanostructures, such as EuO nanorods (NRs) and EuTe nanospindles, and EuX nanocrystal ensembles, has been driven by potential magnetic and magneto-optical device applications.[17, 87] Since EuX crystals have FCC crystallinity, the isotropic crystallinity has to be broken to form one-dimensional (1D) nanocrystals. Oriented attachment (OA) growth has become an efficient route to achieve high-quality 1D NCs.

However, we have to take into account another competing growth mechanism as we identify the mechanism of 1D EuX NCs. The competing growth mechanism is called Ostwald ripening (OR) growth mechanism, which is a common growth mechanism in the colloidal synthesis of many NCs. As shown in Equation 1.20 and Equation 1.21, the kinetics for OA and OR growths are different, which helps to distinguish the two mechanisms for a colloidal synthesis of 1D NC.

In the assembly of constituent objects within a colloidal system, Coulomb interactions (CI), van der Waals interactions (vdW), and interactions between high order moments within a distribution of charges, such as charge-dipole and dipole-dipole interactions, among other phenomena, must be taken into account.[103-105] The kinetics of the assembly of small nanoparticles (< 20 nm in diameter) is often controlled by CI and vdW interactions between the constitutents. The OA mechanism is frequently identified as a governing process in the synthesis of various nanostructures ever since the mechanism was first proposed by Penn and Banfield.[106-108] In the OA growth of 1D nanostructures, spherical NPs typically attach at both ends of the growing 1D nanostructure, with CI and vdW interactions competing in the growth. OA growth can be realized through different mechanisms based on different combinations of attaching units, which include primary and secondary NP monomers. Primary monomers are NPs that are used as precursors at the initial stage of the 1D nanostructure synthesis, and secondary monomers are NPs that grow from primary NP monomers and serve as precursors at an intermediate stage of the synthesis.[75] The associated mechanisms of OA growth can be identified through the kinetic reaction constant, which incorporates the aforementioned CI, vdW, and other possible interactions. Analytical expressions for the vdW interactions between the objects with various shapes have been previously derived and applied. However, to our knowledge, an analytical expression for the vdW interaction between an attaching nanoparticle and a growing 1D nanostructure is still lacking.[106-111] To understand and to manipulate the kinetics of the growth of 1D nanostructures, for which OA is a central component to the assembly, a derivation of an analytical expression for the vdW between the attaching nanoparticle and the growing 1D nanostructure is necessary.

In this chapter, the growth mechanism of 2.5 EuS NPs is analyzed by studying the growth kinetics of EuS NPs at different reaction temperatures. We then derive an analytical expression for the vdW between an attaching nanoparticle and a growing nanorod to allow one to study the correlation between vdW and the OA growth of 1D NC in depth. With the derived expression, we evaluated the correlation between the vdW interaction and the important parameters associated with an OA growth of the NR, such as the dimensions and the separation of the attaching NP and the growing NR.

4.2 OA growth of EuS NPs

4.2.1 Materials and methods

In our research, we explored which of these mechanisms, OA or OR, was dominant in the assembly of 2.5 nm europium sulfide nanocrystals into clusters and, eventually, into 1-D nanorods.[109] A simple materials system was employed. That is, 2.5 nm EuS NCs with strong oleate surface ligands were combined with and oleyamine as the solvent. Monodisperse 2.5 nm EuS NCs, as shown in a transmission electron microscopy (TEM, Philips CM 200 at 200 kV) image in Figure 4.1, were synthesized using a recently reported colloidal synthetic method.[4] After synthesis, the NCs were cleaned with acetone for three times, and suspended in oleyamine/hexane mixture for following uses. The as-prepared suspension was then transferred into a glass reactor, and vacuumed under vigorous stirring at 80 °C for 45 min to remove hexane and other low boiling-point solvents. The vacuumed suspension was heated to target temperatures rapidly and under the protection of argon gas provided through Schlenk line. The reaction time was set at 3 hours for all experiments.

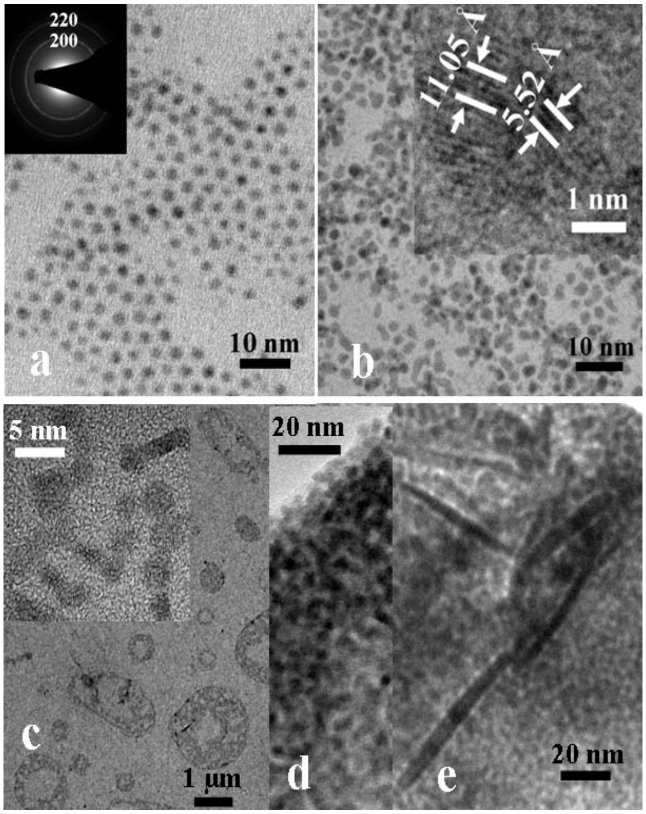

Figure 4.1: TEM image and electron diffraction pattern of (a) 2.5 nm EuS nanoparticle monomers, and TEM images of EuS nanocrystals synthesized at (b) 300 ^{o}C, (c) 310 ^{o}C, (d) 320 ^{o}C and (e) 340 ^{o}C.[109]

4.2.2 Characterization techniques

Fourier transform infrared spectroscopy measurements (FT-IR) were conducted using a Bruker Tensor 27 Fourier Transform Infrared spectrometer. High resolution transmission electron microscopy and selected area electron diffraction (SAED) pattern images were taken using a Philips CM 200 TEM operating at 200 kV.

4.2.3 Results and discussion

We chose four temperatures around which EuS NCs were synthesized and began to assemble into clusters. Among the four temperatures, 300 °C, 310 °C, 320 °C and 340 °C, 300 °C was confirmed to be the nucleation temperature for EuS NC synthesis, and 340 °C was the maximum temperature for oleyamine to stay stable. EuS NCs used in the research were covered by oleate ligand, which was confirmed by the result of FT-IR measurements on the NCs cleaned three times in Figure 4.2.

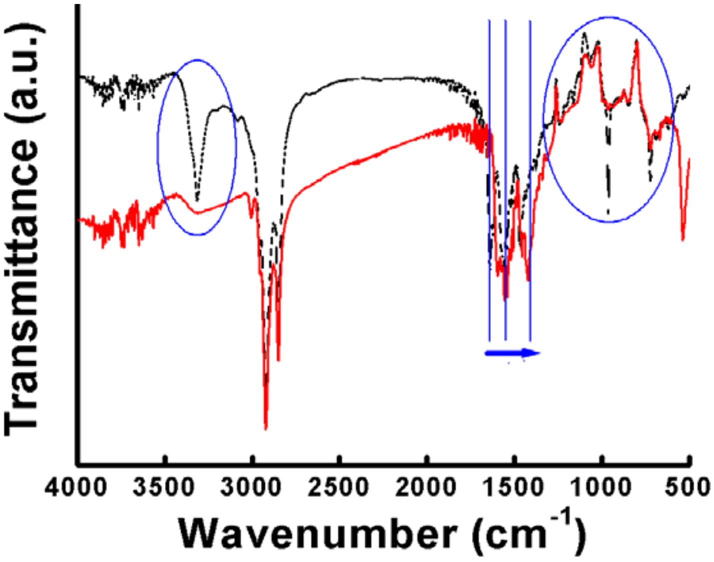

Figure 4.2: FT-IR spectra of 2.5 nm EuS nanoparticle monomers (Black: oleate), and EuS nanocrystals synthesized at 320 °C (Red: oleyamine). The change from oleate to oleyamine is highlighted.[109]

To become soluble, the ligand must be broken and detached from the NCs. The unsolubility of NCs in a solvent increases with the decrease in size at a certain temperature. Therefore, 2.5 nm EuS NCs should show a relatively high solubility in a solvent at room temperature. However, if the NCs are tightly packed by oleate surface ligand, the actual dissolubility would be much lower than that of unligated NCs. Therefore, if the interaction between EuS NCs and the long carbon chain oleyamine molecules is not dominant, the NCs would remain undissolved, and the mechanism would be OA. As shown in Figure 4.1b, dumbbell-shaped structures were formed at 300 °C; although, the size of EuS NCs in these structures remained 2.5 nm. We calculated the lattice spacing of the attachment planes, as shown in the inset of Figure 4.1b, to correspond to the (200) plane, which exhibits a strong electron diffraction pattern as seen in the inset. The persistent, unchanged diameter of the NCs and their associated oriented attachment indicate that the synthesis at 300 °C must be OA.[110]

As the temperature increased to 310 °C, chain-like structures formed; these structures arranged into clusters of diameter between 100-800 nm. The larger clusters appeared as hollow ring-like arrangements, as seen in Figure 4.1c. Similar to that at 300 °C, the size of individual NCs stayed at 2.5 nm; thus, the OA mechanism persisted at 310 °C. However, at this temperature, the EuS NCs interacted with each other more intensively compared with those at 300 °C. Therefore, more EuS NCs would be attached to each other to form chains. Since most ligands were still tightly bonded to the surface of NCs, neighboring charged NCs repelled each other. Consequently, these NCs selectively attached to each other at (200) facets that possessed relatively low ligand concentrations. Among the clusters, smaller ones tended to be solid aggregate, perhaps, due to inter-ligand attraction among the NCs. When these solid clusters interacted with each other, they selectively attached to each other along preferable directions. As a result, the bigger clusters tended to be hollow to minimize their total surface free energy.[42]

As temperature increased to 320 °C, which was the synthetic temperature for the NCs, the average NC diameter increased from 2.5 nm to 3.1 nm. The NCs began attaching to each other in multiple directions, forming even larger aggregations, as evidenced in Figure 4.1d. To assess whether OA or OR could be the underlying mechanism, we calculated the reaction rates based on Equation 1.17 and Equation 1.18 by substituted d_t=3.1 nm, d_o=2.5 nm, and t=180 min into both equations. Both resulting reaction constants were positive, $8.4\times10^{-4}\ \mathrm{min}^{-1}$ for OA and $7.9\times10^{-2}\ \mathrm{min}^{-1}$ for OR. Allowing t to increase and using the same reaction constants, Equation 1.17 tended to reach a maximum at d_t = 6.7 nm, whereas Equation 1.18 yielded a d_t value that monotonously increased with reaction time. OR was readily ruled out as the possible mechanism since a monotonous increase in d_t was not observed in our experiments. This promoted the conclusion that the synthesis at 320 °C corresponded to an OA mechanism. OR might also have occurred due to the enhanced solubility and diffusivity of EuS in oleyamine, but would not have been as dominant in a prolonged reaction. Weakened ligand, higher dissolving and diffusing rates of EuS, and increased thermal momentum of the NCs caused the ligands on EuS NCs to change from oleate to oleyamine. The evolution was confirmed by FT-IR spectrum, as seen in Figure 4.2, as well as the observation that NC aggregation became dominant at this temperature.

After confirming the changes at 320 °C, we anticipated some kinetic change above this temperature. Figure 4.1c shows a characteristic TEM image of the system at 340 °C, which exhibits some NRs among the NC aggregations. The diameters of both the NRs and the NCs were approximately 7.5 nm at t=180 min. Based on a juxtaposition of Equation 1.17 and Equation 1.18, OR mechanism again was ruled out in the long reaction time regime because the dimension for the nanomaterials through OR will not reach a maximum with the given experimental time. Substituting d_t=7.5 nm, d_o=2.5 nm, and t=180 min into Equation 1.17 gives a value for k of $-6.4\times10^{-3}\ \text{min}^{-1}$, which readily ruled out the single-step monomer-monomer OA mechanism. Therefore, secondary EuS NCs must participate in the OA reaction at 340 °C and the kinetic model is thus changed to give a faster growth rate. To calculate k at 330 °C, the experiment at 330 °C was done. At 330 °C, t = 180 min, d_t = 4.8 nm, and k is calculated to be $5.6\times10^{-3}\ \text{min}^{-1}$. Combining the data from the experiment at 320 °C, k at 340 °C is calculated to be $3.5\times10^{-2}\ \text{min}^{-1}$. With reaction time t = 180 min, dt = 7.5 nm and k = 0.035 min-1, a two-step OA reaction mechanism works and the intermediate diameter and reaction time calculated to be 6.4 nm and 177 min, respectively.

Interestingly, NRs also were formed at this temperature. Diffusion-dominated OA mechanism would predict a higher activation energy for high aspect-ratio NRs to form, due to their decreased surface energy. This sample’s aspect ratio (15) is too large for the NRs to form by OA or OR if no other factors, other than diffusion, played a role in the synthesis. This scenario brings attention to other factors, such as a frequency factor in the Arrhenius equation, as shown in Equation 4.1.

$$k = Ae^{-\frac{E_a}{RT}} \tag{4.1}$$

This frequency factor represents the attempt frequency of reagents to cross energy barrier for the reaction to occur. This factor can increase the aspect ratio of 1D nanostructures due to increased electric dipole-dipole interactions. Both increased frequency factor and an increased temperature facilitated the synthesis of EuS NRs.[111]

4.3 OA growth and vdW

4.3.1 Expression Details

Hamaker's derivation of an expression for the vdW force between two spherical particles has been widely used to calculate interactions in colloidal nanoparticle systems, especially when the OA mechanism dominates the interactions among the constituent NP. [106-111] Since vdW between a growing 1D nanostructure and NP monomers is central to the overall kinetics and growth mechanism, we sought an exact analytical expression of the vdW force between a spherical NP and a NR. We adopted Hamaker's particle-particle model as a platform to explore the role of the vdW interaction in the formation of 1D NRs from NP constituents via the OA mechanism. With the new model, we investigated the effects of NP and NR diameter, NP to NR separation, NR aspect ratio (AR), among other parameters, on the interaction.

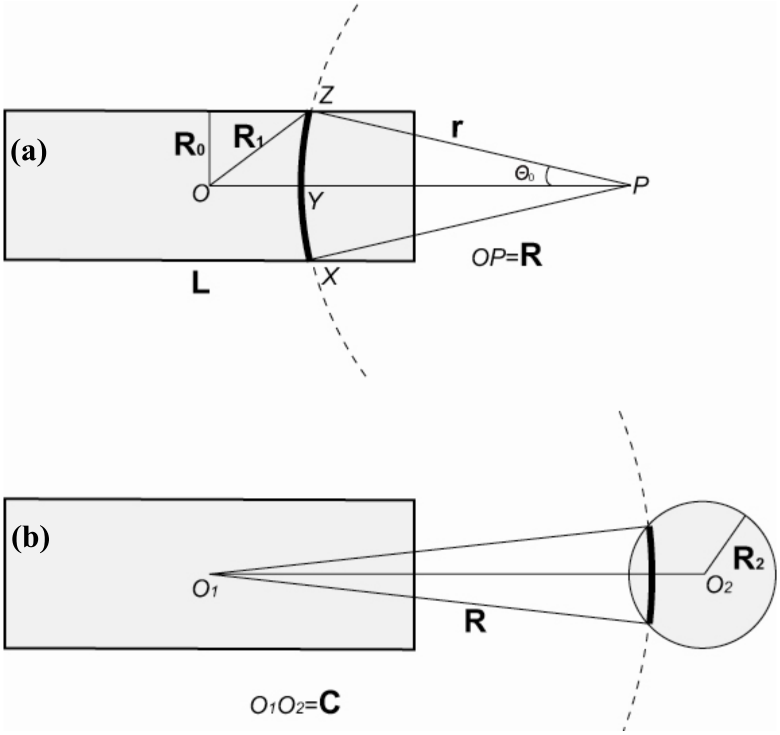

Figure 4.3: (a) Configuration of a cylinder and a sphere for the integration of vdW between a point and a cylinder, and (b) Configuration of a cylinder and a sphere for the integration of vdW over the entire sphere.

The vdW interaction between two spherical particles is given by Equation 4.2, where V_1 and V_2 are the respective volumes of the two particles, r is the distance between the two particles, q is the atomic concentration of the particles, and λ is the vdW constant.[112]

$$E = -\int_{V_1} dv_1 \int_{V_2} dv_2 \frac{q^2 \lambda}{r^6} \tag{4.2}$$

For our calculation, we chose a two-stage integration approach, applied to a solid sphere and a solid cylinder. First, we calculated the vdW between the entire cylinder and a single point within the sphere. Second, we used this solution as the basis to integrate over the entire sphere, yielding the vdW between the two objects. Figure 4.3 illustrates the associated variables of integration for the interaction. Consider a solid cylinder with a radius R_0, length L, and center O; now consider a point P located within the sphere. Point P is located a distance R from the center of the cylinder, O; thus, $OP = R$.

A two-dimensional projection of this configuration is shown in Figure 4.3a. A spherical surface of radius r and centered at P subtends the cylinder. Points X and Z, that in the 2D projection correspond to where the surface of the cylinder is bisected by the spherical surface, centered at P. The distances between O and X and between O and Z are equal to R_1. The three dimensional surface area that is represented by XYZ was calculated from Equation 4.3, where θ_o was related to R_1, R, and r by Equation 4.4. Integrating Equation 4.3 yields Equation 4.5. Another expression involving r, R, and R_1, shown in Equation 4.6, is derived from the triangle ΔOZP. Using Equation 4.6, vdW between P and the entire cylinder is given by Equation 4.7 by integrating from one end of the cylinder to the other. The integral yields Equation 4.8, which will serve as an integration unit in the following stage of this discussion.

$$S(XYZ) = \int_0^{2\pi} d\varphi \int_0^{\theta_0} d\theta r^2 \sin\theta \qquad (4.3)$$

$$R_1^2 = R^2 + r^2 - 2rR\cos\theta_0 \qquad (4.4)$$

$$S(XYZ) = \pi \frac{r}{R}\left[R_1^2 - (R-r)^2\right] \qquad (4.5)$$

$$R_1^2 = R_0^2 + \left(R - \sqrt{r^2 - R_0^2}\right)^2 \tag{4.6}$$

$$E_P = -\int_{R-\frac{L}{2}}^{R+\frac{L}{2}} \frac{\lambda q}{r^6}\pi \frac{r}{R}\left[R_1^2 - (R-r)^2\right]dr = -\int_{R-\frac{L}{2}}^{R+\frac{L}{2}} \frac{2\lambda q\pi}{r^5}\left[r - \sqrt{r^2 - R_0^2}\right]dr \tag{4.7}$$

$$\int_{R-\frac{L}{2}}^{R+\frac{L}{2}} \frac{r - \sqrt{r^2 - R_0^2}}{r^5}dr$$

$$= \left[\sqrt{r^2 - R_0^2}\left(\frac{1}{4r^4} - \frac{1}{8R_0^2 r^2}\right) + \frac{\tan^{-1}\left(\frac{R_0}{\sqrt{r^2 - R_0^2}}\right)}{8R_0^3} - \frac{1}{3r^3}\right]\Bigg|_{R-\frac{L}{2}}^{R+\frac{L}{2}} \tag{4.8}$$

Next, we calculate the vdW interaction between the sphere and the cylinder by integrating across the entire volume of the spherical particle, using Eq. 7 as a unit of integration. This step introduced another configuration between the cylinder and the sphere, as shown in Figure 4.3b. Here, O_1 is the center of the cylinder, and O_2 is the center of the sphere with a radius of R_2. The distance between O_1 and O_2 is C. The result of this integral, shown in Appendix, provides the final platform to assess the vdW interaction for a nanoparticle-nanorod system.

Since the radius and aspect ratio of 1D nanorods are directly related to its optical, magnetic, and electronic properties, varying these values may shed considerable light onto applications of these 1D nanostructures.[113] Since the kinetics and mechanisms of 1D OA growth are closely related to vdW, to understand and manipulate the NP-NR interaction and the subsequent assembly of these 1D nanostructures, we must note how vdW varies as a function of the radii and ARs of the NRs and at what critical separation between the interacting objects the vdW interaction becomes negligible. Since vdW is typically regarded as a short-distance interaction and becomes negligible above a certain separation between the interacting constituents, we first explore the dependence of vdW on the center-to-center distance (*C*) between the NP and the NR. In Figure 4.4, we illustrate the interaction for various diameters of the NP and NR but with the AR for the NR fixed at 10.

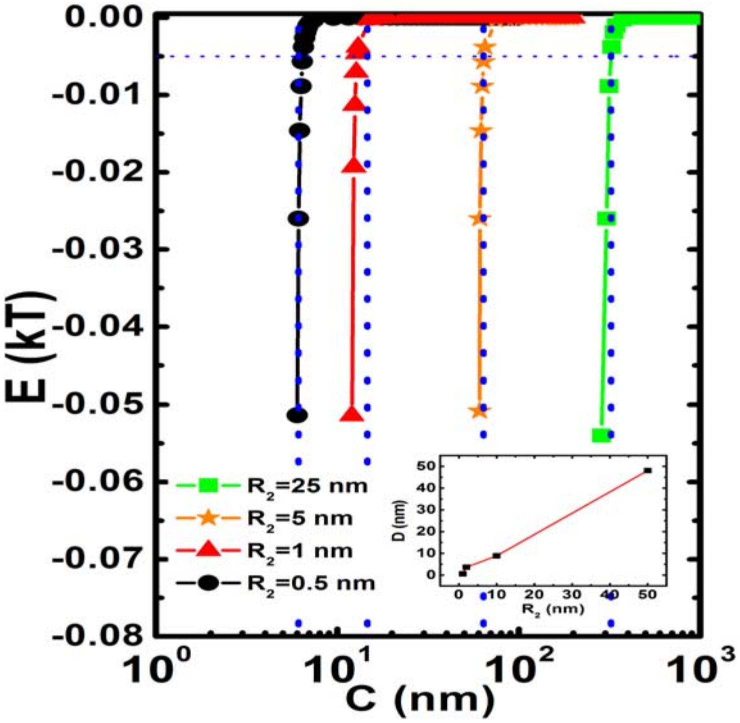

Figure 4.4: Graph of vdW versus C (center-to-center distance between a NP and a NR) for NRs of different diameters. The horizontal dotted line corresponds to 0.5 % kT. Each vertical dotted line corresponds to the critical NP-NR separation distance, Cs, for each NP-NR diameter, beyond which the vdW interaction is negligible. All graphs assume a fixed AR= 10 and T = 300 K. Inset: Plot of D versus R_2

For this calculation, we set the Hamaker constant ($A=\pi^2q^2\lambda$: q = the atomic concentration of the NP and the NR, presumed identical; λ = the pairwise, particle-particle interaction coeficient) for the material to be 10^{-20} J and the ambient temperature to be 300 K. vdW between the NR and the NP decreases as the separation C increases, and the decrease becomes more obvious as the radius of the NP and the NR decreases. As shown in Figure 4.4, as the value of vdW approaches -0.5% kT, the plots show the inflection features where vdW decreases rapidly to zero as C increases and reaches very large values as C decreases. Compared to thermal energy, the contribution of vdW, with values smaller than -0.5% kT, to the kinetics of OA growth is negligible.[114] Therefore, we define the center-center separation with vdW of -0.5% kT as the critical separation (C_c) for all of our calculations. The values of C_c for the 1.0, 2.0, 10.0 and 50.0 nm NPs and NRs are 6.1, 14.6, 63.9 and 323.1 nm, respectively. Therefore, our derivation facilitates the calculation of vdW across all ranges of the separation. Further, we observe the critical features of vdW vs. C plots, for which the dependence of vdW on the separation changes dramatically.

4.3.2 Results and discussion

In a typical OA growth of a NR, the growth occurs uniaxially along one preferred lattice plane, and only the length of the NR increases during OA.[75] Thus, exploring the dependence of vdW on the AR of the NR may provide insight into dynamic anisotropic growth of the NR as addressed by our derived model. To evaluate the correlation between vdW and AR for the OA growth of small NRs, a system comprised of a NP and a NR with a diameter of 2.0 nm is used. We selected 2.0 nm as the target diameter for the NP and NR based on a recently published report on OA growth of ultra-small europium sulfide NPs into NRs.[109] Figure 4.4 illustrates plots of vdW vs. C for NRs of different ARs and at a fixed diameter of 2.0 nm. NRs with ARs at 1, 2, and 10 are representative of the range of OA growth types. The corresponding $C_c s$ for these ARs are 5.80 nm, 6.82 nm, and 14.63 nm, respectively. For these critical values $C_c s$, the critical surface-to-surface separation between the NR and the NP (D) is determined by subtracting $R_2 + L/2$ from C_c. The plots of D vs. R_2 and D vs. AR are shown in the insets of Figure 4.4 and Figure 4.5, respectively.

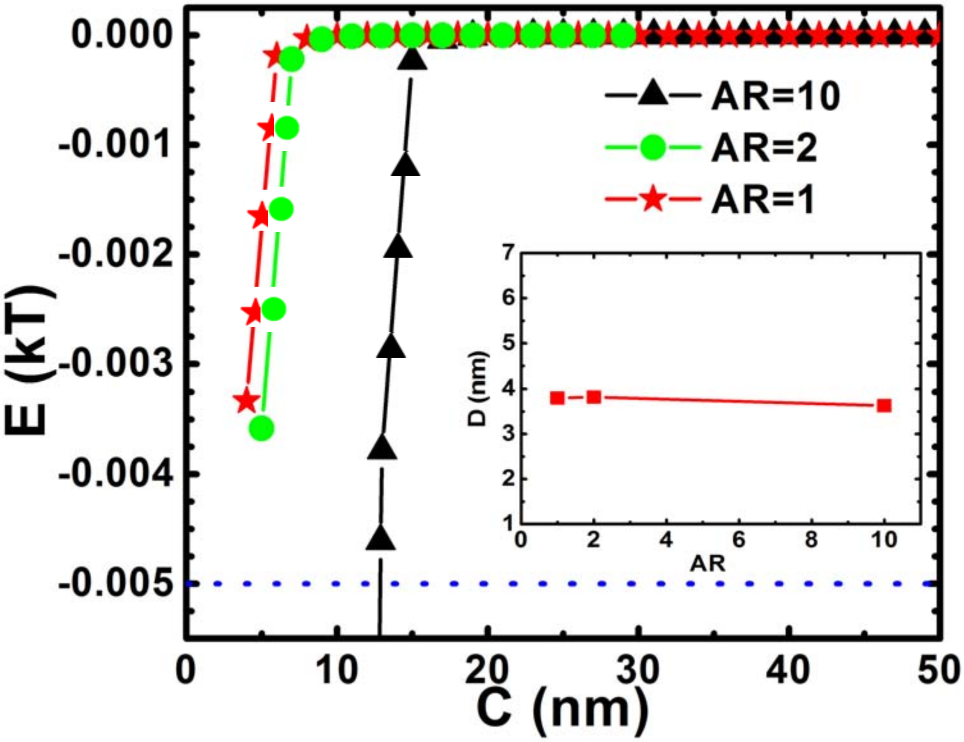

Figure 4.5: Plots of vdW vs. C (center to center) between NPs and NRs with different ARs and fixed diameter of 2 nm. Inset: plot of D vs. AR.

Since vdW is a short-range force that comes from volume integration, D should increase as a function of the diameter of the NP and the NR. Further, as the NR grows longer, vdW between the farthest end of the NR not undergoing OA and the NP undergoing OA becomes vanishingly weaker, which suggests that D should be a very weak function of AR. Figure 4.4 and Figure 4.5 verify this, showing that D increases with increasing of R_2 while D remains nearly constant as AR increases. A linear regression of the D vs. R_2 plot yields an expression for D ($D = -0.45+0.97 R_2$). The plots of D vs. R_2 with varying Hamaker constant (10^{-20} J $\leq$ A$\leq$ 10^{-19} J), are shown in Figure 4.6.

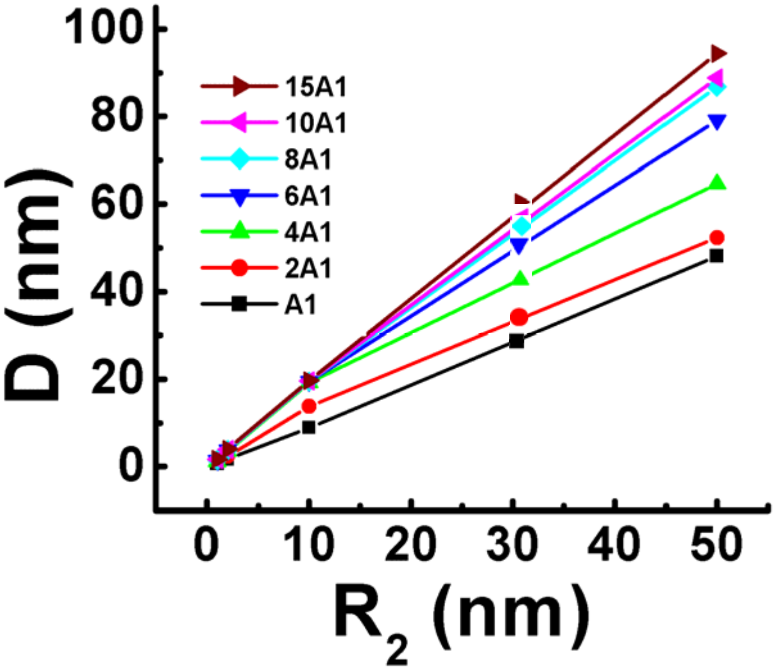

Figure 4.6: Plots of D vs. R_2 at different As and fixed AR of 10. A1=10^{-20} J. The plots give linear expressions between D and R2: $D = x+y R_2$, where the slope S=y.

NPs and NRs with a large diameter would experience a larger attractive force via vdW than would NPs and NRs with a smaller diameter. Therefore, if the vdW interaction is the dominant force that governs OA growth kinetics, larger NRs would grow more rapidly. However, the competition between vdW interactions and other external forces among NPs and NRs, such as Brownian motion cannot be entirely neglected. The effect of Brownian motion on the OA of NPs and NRs may depend on the dimensions of the nanomaterials. Evidence exists for both the promotion and the suppression of nanomaterial growth, depending on the size of the nano-constituents.[75] That the surface-to-surface separation remains constant as AR varies (Figure 4.5 Inset) suggests that the growth kinetics tend to remain constant as the NRs grow if vdW dominates over both CI and Brownian motion effects. However, the dominance of the vdW interaction in the kinetics of OA also can be challenged by other parameters, such as additional precursors, resulting in the change in the concentration of attaching monomers and, thus, leading to increased growth kinetics.

Since the Hamaker constant, A, is a function of the atomic concentration and the pairwise interaction of the two interacting nanoscale constituents, we chose to explore the dependence of the surface-to-surface separation on the Hamaker constant within the range (10^{-20} J $\leq$ A $\leq 1.5\cdot10^{-19}$ J).[115] Figure 4.7 shows the plot of D vs. A with the aspect ratio of the NR fixed at 10. For each radius of the NRs, D increases as A increases, although D increases asymptotically as A increases. For example, above $A=6\times10^{-20}$ J, D for 10 nm NRs reaches its maximum at 19.5 nm. To learn more about how the Hamaker constant influences the growth of the NRs, we plotted the slope (S) of the D vs. A graph as a function of A.

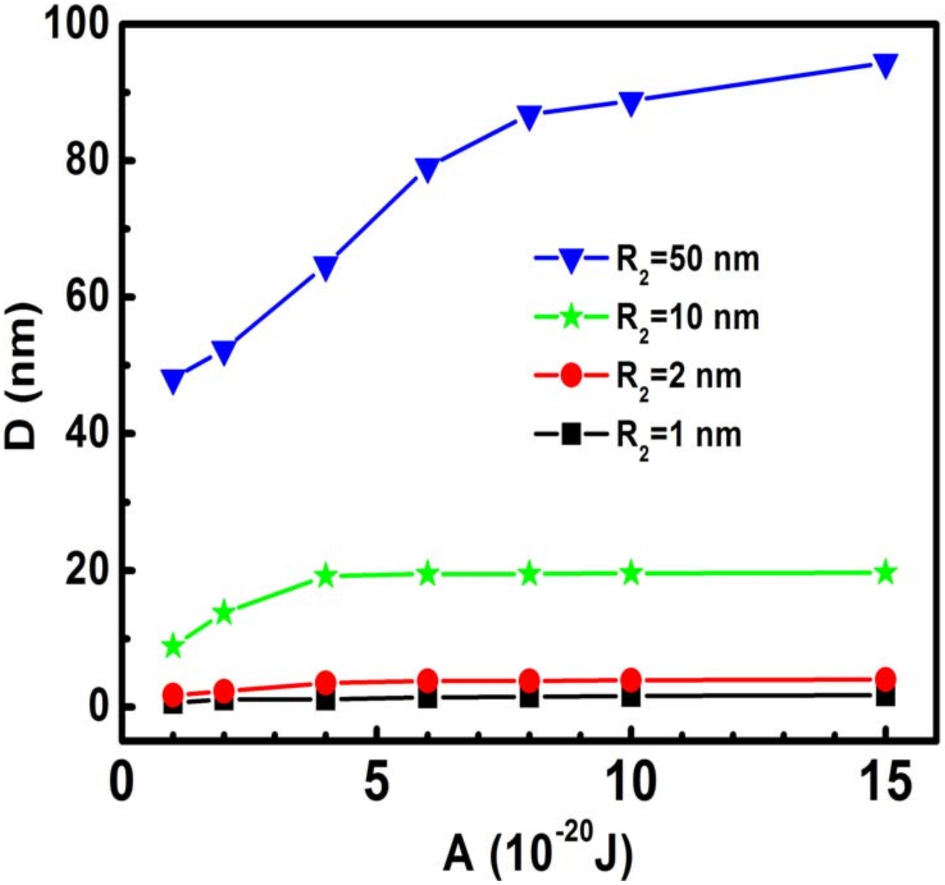

Figure 4.7: Plots of D vs. A with different R_2s and a fixed AR of 10.

Displayed in Figure 4.8, the graph reflects an asymptotic increase that is similar to those of the plots of D vs. A. This finding suggests that the Hamaker constant has limited influence, above a critical value ($A \approx 6.0 \cdot 10^{-20}$ J), over the surface-to-surface separation for NPs and NRs of diameters upwards of 20 nm. This may explain why a change of surfactants and an increase of temperature would not enhance the kinetics of NR growth as substantially as an increase in the concentration and the size of the primary NP monomer precursors.

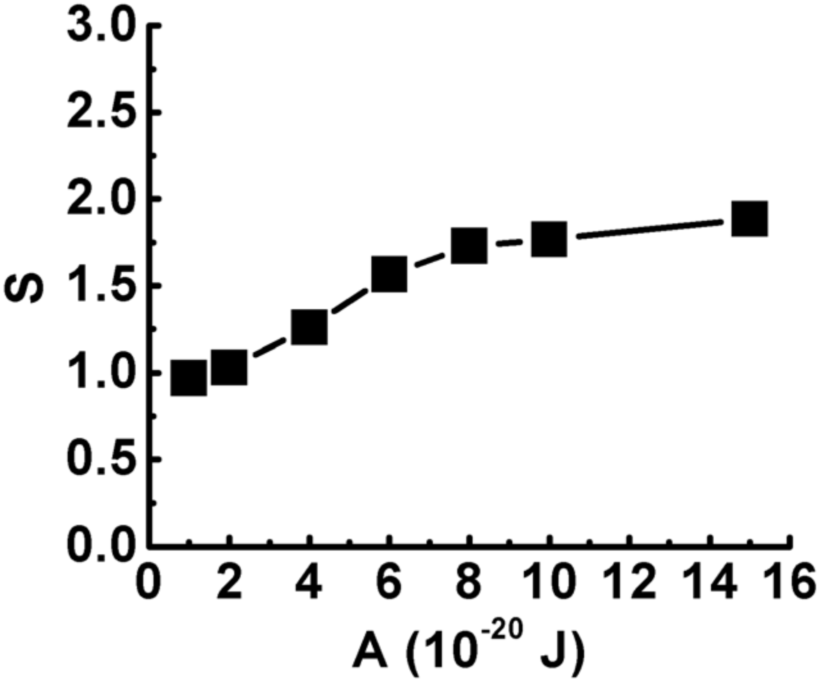

Figure 4.8: Plots of S vs. A with fixed AR based on the expressions D = x+y R_2, where the slope S=y.

However, such an increase in the reaction kinetics of colliding and reacting NP monomers only occurs below a particular concentration limit of monomer precursors. Above the limit, the effect of the increase is offset by a decrease in the growth of the NRs due to random destructive collisions among the NP and NR constituents. Thus, the combination of these phenomena results in stable kinetics for the growth of NRs via OA mechanism. Thus, our analytical expression for the vdW interaction provide a route toward the analysis of nanoscale systems undergoing oriented attachment growth.

4.4 Summary

In summary, clusters of EuS nanocrystals were synthesized through an oriented attachment mechanism by thermally annealing 2.5 nm EuS NCs ligated with oleate. An increase in thermal energy changed both the ligand and reaction constant, which gave rise to a multilevel OA mechanism that produced high aspect-ratio EuS nanorods. These results help improve our understanding on both OA and OR growth mechanisms, and may assist in the synthesis of nanoclusters and NRs of other nanomaterials. An analytical expression for evaluating the van der Waals interaction for a random nanoparticle-nanorod system was derived. The expression facilitates the calculation of the interaction between nanoparticles and nanorods, of different sizes and aspect ratios, in the oriented attachment growth mechanism, and, thus, provides a path towards the solution of what surface-to-surface separation distances between NRs and NPs are relevant in the dynamic growth of NRs. Given the appropriate Hamaker constant and the relevant Coulomb interaction, dipolar, and other particle-particle interactions, the opportunity to evaluate the kinetics and mechanisms of OA growth based on NP monomers, through the incorporation of experimental data, can be realized.

CHAPTER V

ELECTROPHORETIC DEPOSITION OF Te AND Eu_2O_2S NANOCRYSTALS

5.1 Introduction

In Chapters II-IV, the syntheses, optical & magnetic properties, and growth mechanisms of NCs were investigated. By controlling the growth mechanism of NCs, one can finely tune the size and shape of NCs, and a fine tuning of size and shape led to improved properties of NCs. Improved properties of the NCs make these NCs promising candidates in device applications. A necessary step towards the application of the NCs is to assemble the NCs to uniform films using a scalable assembly technique. An efficient assembly technique allows one to deposit NCs with different shapes and morphologies into uniform NC films with thickness control. The method should also be cost-effective. There are a number of deposition techniques allowing one to assemble NCs into films, such as spin-coating, and Langmuir-Blodgett (LB) method, etc.[116-117] Recently, an electrophoretic deposition technique has been frequently regarded as a highly-efficient assembly method and an efficient way to assess the applicability of colloidal NCs.[78],[118] EPD has also shown its capability of directly assembling NCs into devices. For example, at Professor James Dickerson's group at Vanderbilt University, a metal-oxide-semiconductor capacitor device was made using EPD and the device exhibited high-performance charge-storage properties.[122] Once NCs are synthesized, NCs can be deposited onto either cathodes or anodes, depending upon the ligands that the NCs carry. To deposit NCs onto cathodes, the NCs in suspension form have to carry positive charges under an electric field, whereas for a deposition on the anodes to occur the NCs have to be negatively charged. In both cases, the charges of the NCs are induced by the organic ligands on the surface of the NCs. In order for a deposition to occur, a number of other parameters have to be taken into consideration, such as the voltage, subtrate/elecrodes solvent, and concentration of deposited NCs.[80, 119-121]

In Professor James Dickerson's research group, various NCs have been successfully deposited into uniform films via an electrophoretic deposition technique. For example, CdSe quantum dots, carbon nanotubes, and graphene were deposited into uniform thin films using an electrophoretic deposition technique in the group.[76, 81-82, 118-119] Most recently, iron oxide monolayers have been made in the group.[123] All these high-quality depositions have confirmed that electrophoretic deposition is an efficient way of assembling NCs into uniform films and devices.

In this chapter, towards the applications of the colloidal NCs we synthesized, colloidal Te nanoparticles and Eu_2O_2S nanorods, both of which show promising application potentials in various fields and were synthesized in our research, are deposited into thin films through electrophoretic deposition. The thickness of these films is controlled by varying deposition time. In addition, electrophoretic deposition is employed to separate Te nanorods from Te nanoparticle/nanorod mixtures.

5.2 Electrophoretic deposition of Te nanoparticles and Eu_2O_2S nanorods

5.2.1 Materials and methods

Tellurium NPs were synthesized in a one-step fashion at room temperature by using sodium telluride (Na_2Te) as a precursor and oleic acid (OA) as an oxidizing agent in the presence of triethanolamine (TEA) dissolved in ethylene glycol (EG).[56] Since all employed chemicals are environmentally friendly, this synthetic approach can be accomplished by green chemistry. Further, the synthesis yielded two distinct NP size distributions simultaneously: one diameter centered at 1.5 ± 0.5 nm and one centered at 27.5 ± 5 nm. 27.5 nm Te NPs were chosen to make electrophoretic deposition films.

Figure 5.1 shows the computer-based electrophoretic setup. EPD of Te films was conducted using 1 cm x 2 cm electrodes comprised of gold deposited on a Si substrate. Two electrodes were mounted in a parallel-plate configuration with ~4 mm gap. With 10.0 V DC voltage applied, the electrodes were lowered about 1.0 cm into a 15.0 mL solution containing Te nanoparticle suspension in methanol.

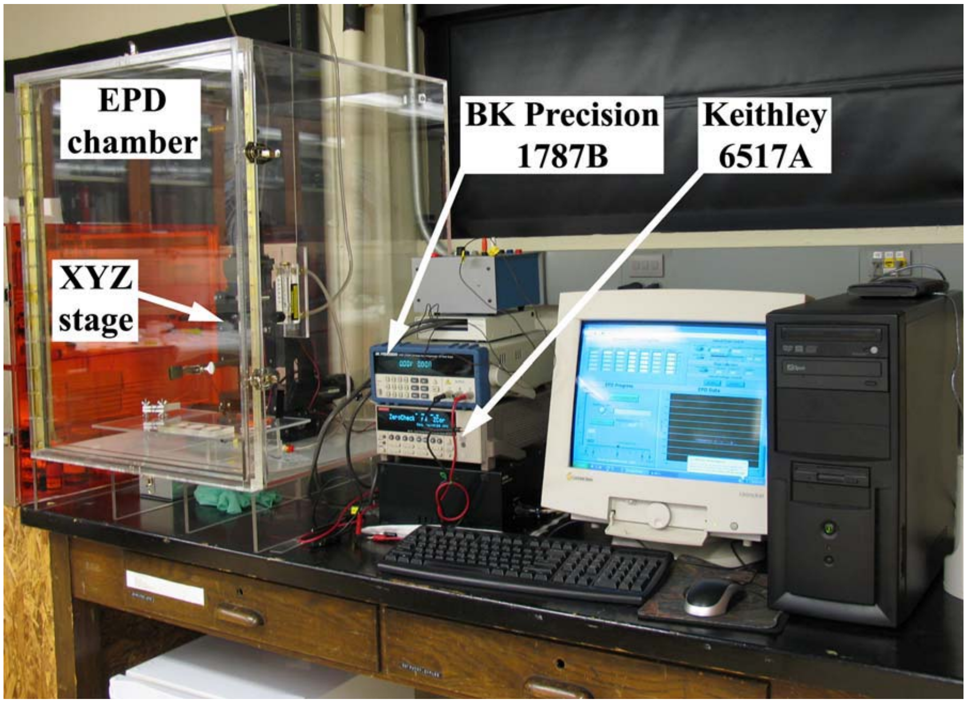

Figure 5.1: Automatic electrophoretic deposition setup connected with a computer. at Professor James Dickerson’s research group at Vanderbilt University.

After ~20.0 min, the electrodes were raised from the solution and the voltage subsequently turned off after another 10.0 min. The cathode possessed a macroscopic film that was visible to the naked eye. Figure 5.2 shows the LabVIEW program designed for the setup.

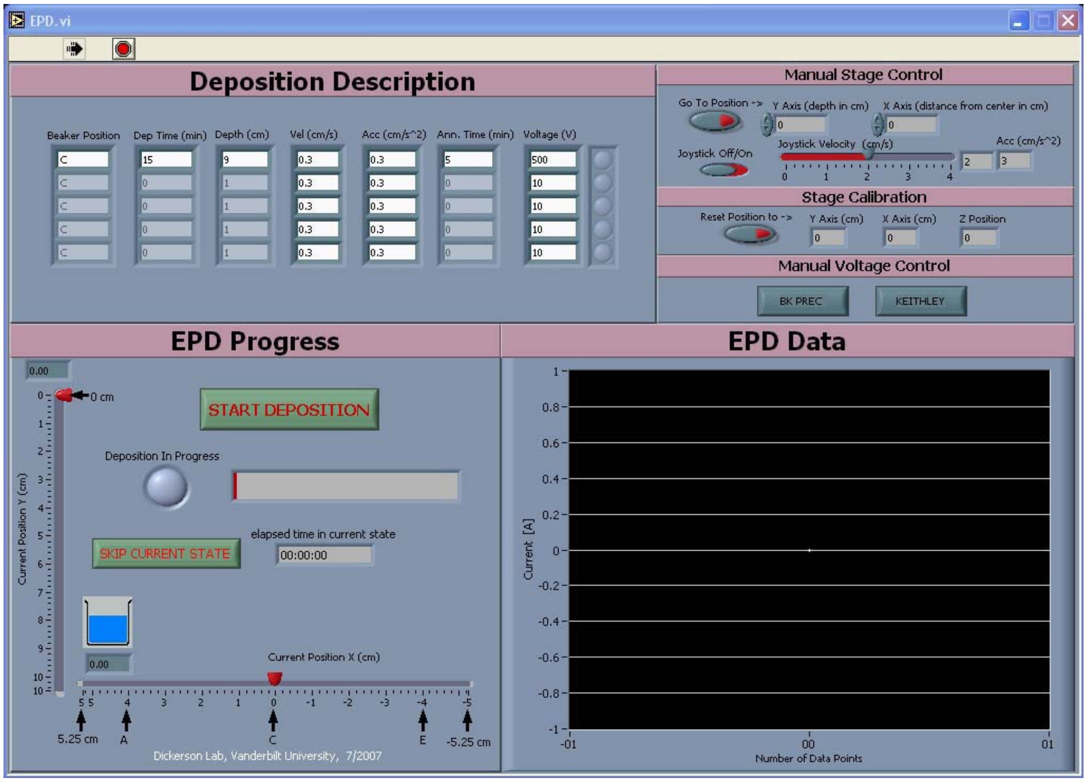

EPD.vi

Deposition Description

Beaker Position	Dep Time (min)	Depth (cm)	Vel (cm/s)	Acc (cm/s^2)	Ann. Time (min)	Voltage (V)
C	15	9	0.3	0.3	5	500
C	0	1	0.3	0.3	0	10
C	0	1	0.3	0.3	0	10
C	0	1	0.3	0.3	0	10
C	0	1	0.3	0.3	0	10

Manual Stage Control

Go To Position -> Y Axis (depth in cm) 0 X Axis (distance from center in cm) 0

Joystick Velocity (cm/s) 2 Acc (cm/s^2) 3

Stage Calibration

Reset Position to -> Y Axis (cm) 0 X Axis (cm) 0 Z Position 0

elapsed time in current state 00:00:00

Figure 5.2: The LabVIEW software designed for electrophoretic deposition at Professor James Dickerson's research group at Vanderbilt University.

5.2.2 Characterization techniques

Atomic force microscopy measurements (AFM) were obtained using a Digital Instruments Nanoscan III Atomic Force Microscope. Scanning electron microscopy (SEM, Hitachi S-4200) was used to study the morphology of the deposited films.

5.2.3 Results and discussion

The current change during the deposition is shown in Figure 5.3. The current decreases as the deposition continues and this is due to the increased resistance as the thickness of Te film increases.

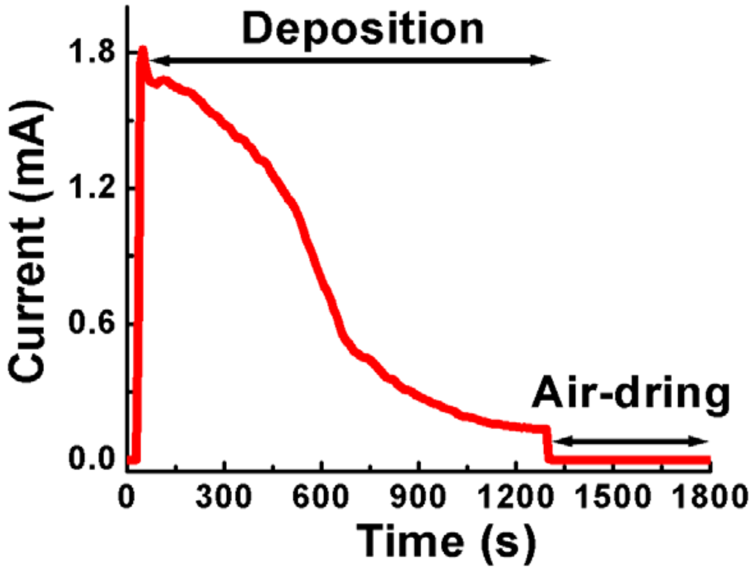

Figure 5.3: Electrophoretic deposition current versus time graph four our 27.5 nm Te nanoparticles. After approximately 22 minutes, the electrodes were extracted from the suspension and were dried in air with the applied voltage maintained.[56]

The anode had no deposited film, indicating that only positively charged particles deposited onto the electrodes. We used methanol as the solvent in our experiments. The Te NPs rendered a positive charge as oxygen single bond of TEA was dissociated by methanol. In the deposition, the net positive charge caused the Te NPs to move along the direction of applied electrical field. By changing the deposition time, films with different thicknesses, ranging from tens of nanometers up to several hundred nanometers, could be produced from the methanolic Te NPs suspensions. Atomic force microscopy (AFM; Figure 5.4a) and scanning electron microscopy (SEM; Figure 5.4b) images of films produced from 27.5 nm Te NPs highlight an intriguing phenomenon that occurred during the deposition.

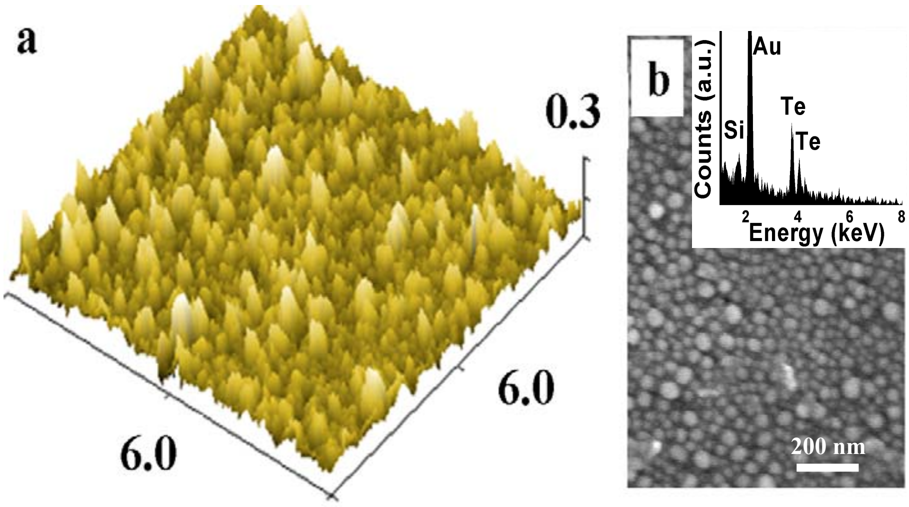

Figure 5.4: (a) AFM image of 27.5 nm Te NP EPD films deposited for 20 min. Scale unit: µm. (b) SEM image of as-deposited 27.5 nm Te NP film. EPD-induced growth of NPs, as large as 50 nm, can be seen.[56]

Energy dispersive X-ray analysis (EDS; Inset of Figure 5.4b) were performed using Hitachi S-4200 Scanning Electron Microscope, which confirmed the presence of Te in as-deposited films. We observed that larger Te NPs, some upwards of 50 nm in diameter (Figure 5.4b), comprised a significant fraction of the EPD film. We attribute this apparent disparity in the nanoparticle diameter, seen in AFM and SEM versus that seen in TEM, to EPD-induced nanoparticle aggregation and growth. Such nanoparticle growth has been reported for other colloidal metallic nanoparticles (Au and Ag nanoparticle films), cast into films by electrophoretic deposition.[124-126] Unlike that reported for the EPD-facilitated growth of Au and Ag NPs, our Te NPs maintained their hexagonal shape during the EPD-induced crystal growth.

The thickness of as-synthesized Te NP film was 220 ± 29 nm, measured by a Veeco Dektak 150 profilometer. Additional AFM images were used to confirm the high-quality surface morphology and uniformity of the Te NP films (see Figure 5.5).

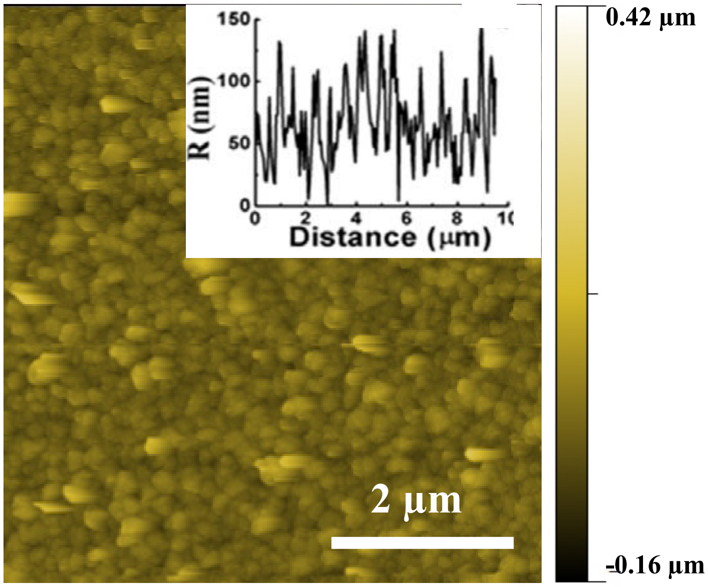

Figure 5.5: 2D AFM image of 27.5 nm Te NP EPD films deposited for 20 min. Inset: Roughness curve of this film, giving a root-mean-square (RMS) roughness of ~34.0 nm.[56]

The fabrication of Te NP films by EPD offers a route toward the facile implementation of colloidal tellurium nanostructures into device architectures.

5.3 Electrophoretic deposition of Eu_2O_2S nanorods

5.3.1 Materials and methods

The Eu_2O_2S nanorods were synthesized in a Schlenk line using a chemical route described in Session 2.3. To explore using Eu_2O_2S NRs as building blocks for the assembly of films by EPD, we cleaned 1.5 g aliquots of NRs with acetone four times, followed by three times of cleanings with centrifugation for 45 min at 3500 rpm. After the cleaning, the NRs were suspended in hexane for the EPD assembly. The EPD was conducted by using a pair of indium-tin-oxide-coated (ITO) glass as electrodes (dimension 1.5 in × 3 in), mounted in a parallel plate configuration with a 5.0 mm separation. These electrodes were inserted into the NR suspension. A 500.0 V DC voltage was applied across the electrodes for 15 minutes. To facilitate the densification of the films, the films were extracted from the suspension after the 15 minutes had elapsed and were kept in air with the deposition voltage maintained for an additional 10 min.

5.3.2 Characterization techniques

Scanning electron microscopy (SEM, Hitachi S-4200) was employed to study the morphology of the deposited films. Atomic force microscopy measurements (AFM) were conducted using a Digital Instruments Nanoscan III Atomic Force Microscope.

5.3.3 Results and discussion

The films were observed to have deposited onto the anodes, which implied that the NRs in the colloidal suspension were negatively charged. A Bruker Tensor 27 Fourier transform infrared spectroscopy (FTIR) system was used to study the surface ligands on the NRs. The FTIR spectrum (see Figure 5.6) showed that the NRs were well-ligated by oleate.

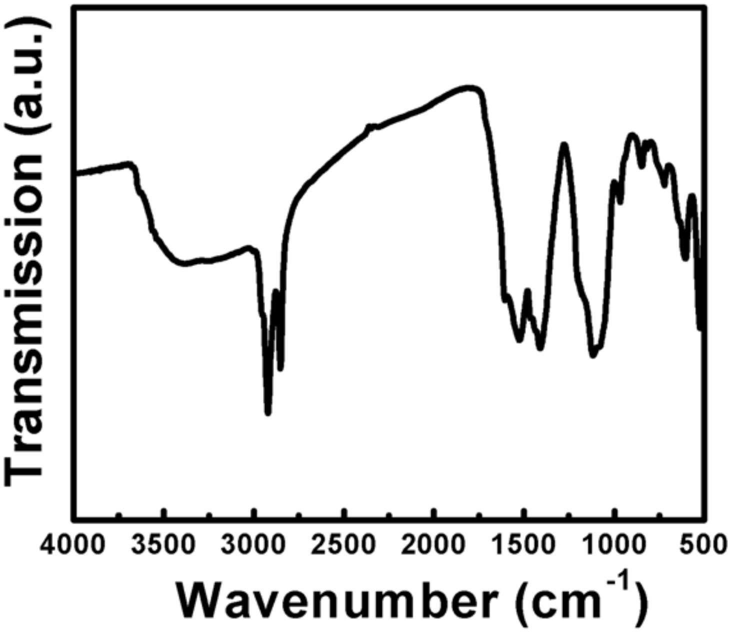

Figure 5.6: FTIR spectrum of $Eu_2O_{2-x}S$ NRs with a diameter of 3.5 nm and an aspect ratio of 5. It confirms that the surface ligand on $Eu_2O_{2-x}S$ NRs is oleate.

Atomic force microscopy (AFM) images, as shown in Figure 5.7a, and scanning electron microscopy (SEM, Hitachi S-4200) images, as shown in Figure 5.7b, were taken to measure the surface roughness and morphology of the film deposited for 10 min, respectively. The SEM image confirmed that the EPD film contained tightly packed NRs with a large-range surface uniformity. The thickness of the film was 675 ± 30 nm, as measured with a Veeco Dektak 150 profilometer.

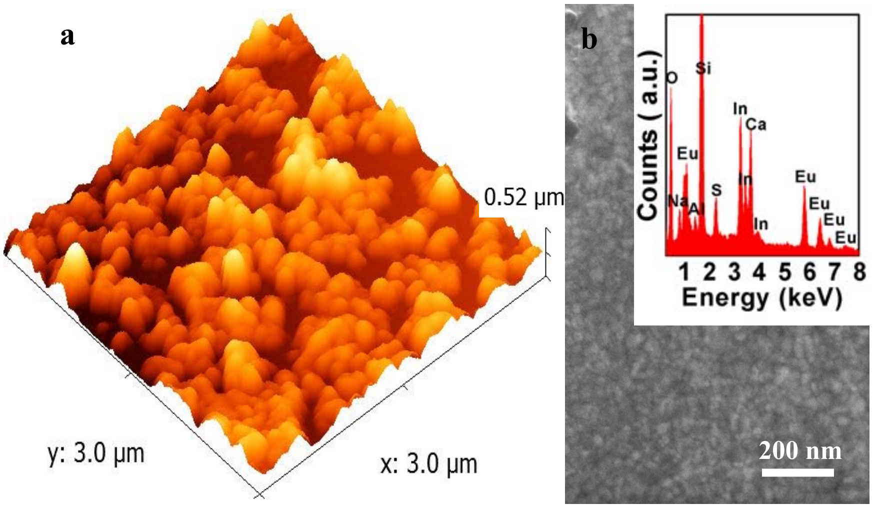

Figure 5.7: (a) AFM image of $Eu_{2+x}O_2S$ NR (D=3.5 nm and AR=4) EPD film deposited for 10 min on ITO substrate with a DC voltage of 500 V. (b) SEM image of as-deposited $Eu_{2+x}O_2S$ NR film. EPD-induced aggregation of NRs, can be seen; the inset shows the EDS spectrum of the $Eu_{2+x}O_2S$ NR film on ITO substrate.

From the AFM image, the RMS roughness of the same film was 33.8 ± 4.5 nm for the film. Compared to the thickness of the film, the roughness suggests that the film has a high homogeneity of film thickness and morphology. Energy dispersive X-ray analysis (EDS), shown in the inset of Figure 5.7b, confirmed the presence of Eu, S, and O from the NR film. By varying the deposition time from 5 min to 45 min, highly uniform and tightly-packed $Eu_{2+x}O_2S$ NR films with different thicknesses, ranging from a few hundred to one thousand nm, were prepared via the same EPD technique (see Figure 5.8). The highly-viable deposition suggests that the synthesized colloidal ultra-thin $Eu_{2+x}O_2S$ NRs can be efficiently assembled for the potential optical and magnetic applications.

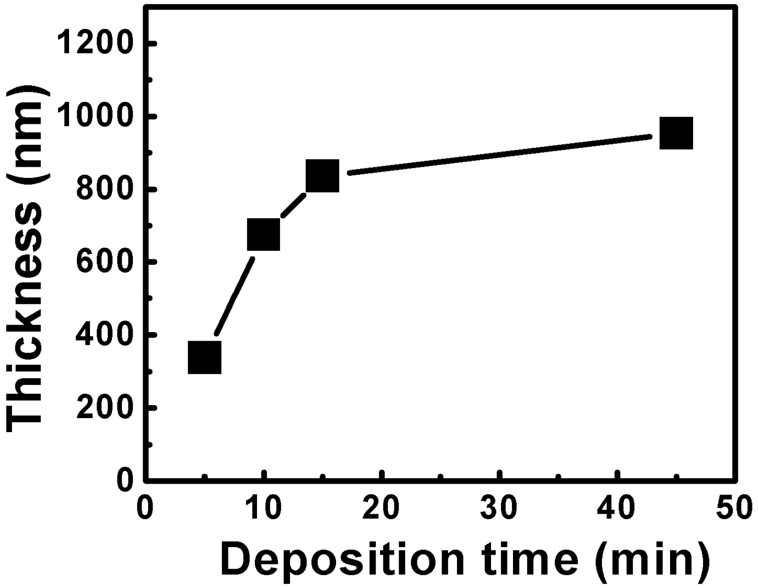

Figure 5.8: The plot of the thickness of $Eu_2O_{2-x}S$ NR electrophoretic deposition film versus deposition time. The diameter of the NRs is 3.5 nm and the aspect ratio of the NRs is 5. The applied voltage was 500 V and the NRs were suspended in hexane during deposition.

5.4 Electrophoretic separation of Te nanorods

5.4.1 Materials and methods

Te nanorods mixed with Te nanoparticles were synthesized through a facile room temperature colloidal method with the presence of triethanolamine surfactant. The synthetic route followed the one we recently reported.[56] With 3.0 mL or less triethanolamine, the nanorod-to-nanoparticle ratio increased with the amount of triethanolamine while with 3.0 mL or more, only nanoparticles formed. Fourier transform infrared spectroscopy measurements confirmed that this surfactant-dependent growth was induced by the selective liganding of OH and C-C-O groups in triethanolamine. In electrophoretic deposition, the Te NP/NR mixture synthesized with 3 mL triethanolamine was employed. The deposition conditions are similar to those for the deposition of 27.5 nm Te NPs (Session 2.4).

5.4.2 Characterization techniques

Scanning electron microscopy (SEM) images were taken using a Hitachi S-4200 microscope to study the morphology of the deposited Te NC films.

5.4.3 Results and discussion

In our EPD of Te NR/NP, only NRs of the NR/NP mixtures suspended in methanol were deposited on Si substrates, as confirmed by Figure 5.9. This selective deposition of Te NCs was possibly facilitated by the different liganding of OH and C-C-O groups attached to the surfaces of Te NPs and NRs.[127-128] With C and O as terminating atoms in C-C-O groups, C-C-O groups possibly had a larger net charge than HO groups. With more C-C-O groups as surface ligands on Te NRs, the Te NRs had a larger net charge compared to Te NPs, and the selective EPD of Te NRs was then probably facilitated by the enhanced mobility of Te NCs with a large net charge. This indicates that EPD is not only an effective technique to deposit NC films, but also an effective separation technique for NCs with different ligands.

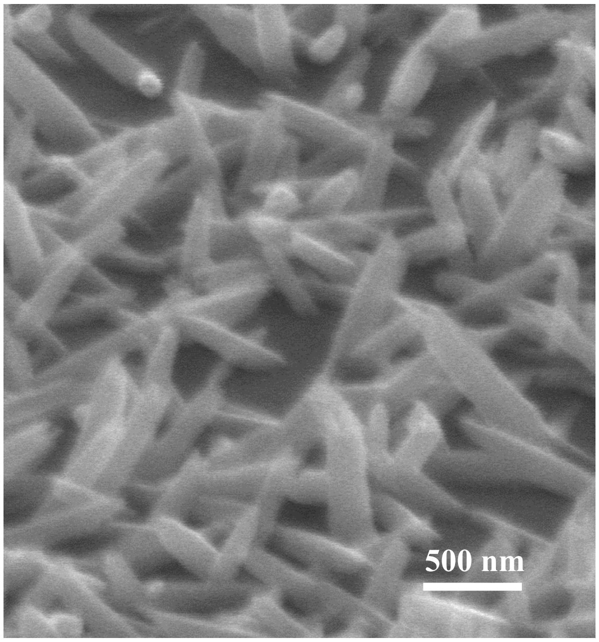

Figure 5.9: SEM image of the EPD film of Te NCs synthesized with 3.0 mL TEA. Insets: TEM image (a) of (100) Te NR and electron diffraction (b) of the Te NCs.

5.5 Summary

In summary, colloidal Te nanoparticles and ultra-thin Eu_2O_2S nanorods were deposited into uniform films via an electrophoretic deposition technique. Electrophoretic deposition allowed the successful deposition of Te and Eu_2O_2S NC films with tunable thicknesses. The method was shown to be an efficient method for the separation of two different nanostructures, such as the separation of Te nanorods and Te nanoparticles. The successful assembly of these colloidal NCs allowed the synthesized NCs to be employed in device applications.

CHAPTER VI

CONCLUSION

In my dissertation research, I aimed to achieve desirable physical properties of materials by finely controlling their size and shape, and then assembling them into uniform films for device applications. To achieve the goal, I focused on ultra-small NCs, and the study covered a broad range of research topics on nanoscale materials, including colloidal synthesis, optical and magnetic properties, growth mechanism, and deposition. First, ultra-small europium compound and tellurium nanocrystals were synthesized. The optical and magnetic properties of these nanocrystals were then measured and analyzed. The growth mechanism of colloidal EuS nanorods was investigated and an electrophoretic deposition technique was employed to assemble the quantum dots and quantum nanorods into uniform films. A summary of the main scientific findings in this work is outlined in the following.

EuTe nanoparticles with different size distributions were synthesized via a two-step colloidal method at room temperature for the first time. By adding phenanthroline, 1D EuTe nanospindles were also synthesized. The facile synthesis of EuTe NCs allows one to study the optical, magnetic, and magneto-optical properties of dimensionless or 1D EuTe crystal at the nanoscale. In the research on EuTe NCs, absorption peaks showed very clear blue shifts as the diameter of EuTe nanoparticles decreased from 7.3 nm to 5.5 nm, which confirmed that the quantum confinement of the material was enhanced as the size decreased. Gilles' non-Langevin model was employed to study the magnetic data taken at National High Magnetic Field Laboratory in Florida. Besides the increased magnetization, significant ordering temperature was observed on the EuTe nanoparticles. For 5.5 nm EuTe nanoparticles, the T_N was 16.5 K, and that for 7.3 nm EuTe nanoparticles was 27.0 K. Compared to the ordering temperature of EuTe in bulk form, i.e. 9.6 K, these enhanced ordering temperatures of the synthesized EuTe nanoparticles are significantly higher. The enhancement of ordering temperature was found to be due to net 3D compressive lattice strain caused by the lattice mismatch between Te and EuTe crystals at the EuTe/Te interface of the EuTe nanoparticles. The result shows that introducing 3D compressive strains is an efficient method to enhance the ordering temperature of an ultra-small magnetic material. The research opens up the opportunity for low-temperature magnetic materials to be employed in device applications.

Ultra-thin Eu_2O_2S nanorods were synthesized through a hot-injection technique. During the synthesis, the S precursor was injected into the Eu precursor with a syringe pump at the reaction temperature. The smallest diameter obtained in the synthesis was 1.5 nm. The PL peaks of the nanorods showed an obvious blue shift as the aspect ratio of the nanorods decreased, which was due to the enhanced quantum confinement. Unexpectedly, the ultra-thin Eu_2O_2S nanorods showed magnetic properties in both magnetization-versus-temperature and magnetization-versus-field measurements. Eu_2O_2S in bulk form does not possess unpaired electron pairs, and, thus, does not exhibit magnetic properties. The observed magnetism was due to the astoichiometry of the nanorods, as confirmed by energy dispersive spectra. Due to the astoichiometry along with the ultra-thin diameter of the nanorods, the electron spins of the material could be rearranged and such a rearrangement of the spins gave rise to magnetic response for the material.

To understand the growth mechanism of ultra-small nanocrystals, 2.5 EuS nanoparticles were synthesized as monomers. After synthesis, the nanoparticles were cleaned for multiple times to remove a portion of oleate surface ligands. The cleaned samples were then reacted at different temperatures. At a temperature below 320 ^{o}C, only primary EuS monomers participated in the growth of the resulted EuS clusters. At a temperature higher than 320 ^{o}C, secondary EuS nanoparticles participated in the growth of larger EuS nanoparticles. The kinetics of all the growths was studied by oriented attachment and Ostwald ripening kinetic models, and the study confirmed that the growth of EuS in this research was a typical oriented attachment growth. Interestingly, at 320 ^{o}C the surface ligand of EuS nanoparticles started to change from oleate to oleylamine. Due to the increased thermal energy as well as the ligand change, EuS nanords started to form at 340 ^{o}C, and, thus, the isotropic crystallinity of FCC EuS crystal was broken.

To study the kinetics of the growth of a nanorod formed by the oriented attachment of individual nanoparticles, an analytical expression for van der Waals interaction between an attaching nanoparticle and a growing nanorod was derived. vdW interaction was calculated with respect to center-to-center distance for nanorods with different diameters and various aspect ratios. The results showed that the magnitude of vdW was largely dependent upon the diameter of the nanoparticle and nanorod. vdW interactoin was almost constant as the aspect ratio of the nanorod increased, which indicates that vdW does not increase much as a nanorod grows longer via oriented attachment.

To move one step forwards the application of the synthesized NCs, an electrophoretic deposition technique was employed to assemble the NCs into films. Te quantum dots and 1D Eu_2O_2S nanorods were successfully assembled into uniform thin films through an electrophoretic deposition technique. The deposited films show very nice uniformity on the thickness as well as small surface roughness. The thickness of the films was tuned between several hundred nm and several μm by changing the deposition time. The high-quality electrophoretic deposition confirmed that the synthesized colloidal NCs were well ligated by organic ligands, and highly-applicable.

Following the research depicted in this dissertation, many interesting research topics can be conducted in the future. For example, the ordering temperature of EuTe could be enhanced further, hopefully above the boiling temperature of nitrogen, and then its magnetic properties may be useful for applications in various areas, such as optical insulator, optical switch and spin filter applications. The magneto-optical properties of EuTe nanoparticles and nanospindles can be remarkable compared to those of bulk EuTe, which is indicated by the size-dependent optical and magnetic properties of EuTe. The transition between magnetism-diamagnetism could be possible for other Eu^{3+} compounds, such as Eu_2O_3 nanocrystals. If such a transition is observed on these materials, they could possibly exhibit magneto-optical properties at room temperature, which would largely improve the applicability of these materials. In the future, hysteresis, field-cooled and zero-field-cooled magnetic measurements could be conducted in National High Magnetic Field Laboratory to measure Eu_2O_2S nanorod films with various thicknesses. Professor James Dickerson's research group has showed recently that particle-particle interaction is important for their magnetic properties in nanoparticle powers and electrophoretic films. The purpose of this research is to study whether that the magnetic properties of the nanorod films can be adjusted by the size of the deposited nanorods as well as the number of layers of the nanorod films as deposited via an electrophoretic deposition technique.

APPENDIX

vdW EXPRESSION

$$
-\frac{2\pi^{2}q^{2}\lambda}{C}\frac{1}{24}\left\{\begin{array}{l}
\frac{1}{R_{0}^{3}}\left(\left(L/2\right)^{3}-3C\left(L/2\right)^{2}-3R_{2}^{2}\left(L/2\right)+3\left(C^{2}+4R_{0}^{2}\right)\left(L/2\right)-12CR_{0}^{2}\right)\\
\left[\begin{array}{l}
\tan^{-1}\left(\frac{R_{0}}{\sqrt{\left(L/2\right)^{2}-2R\left(L/2\right)-R_{0}^{2}+R^{2}}}\right)-\\
i\ln\left(\frac{2R_{0}^{2}\left(\sqrt{\left(L/2\right)^{2}-2R\left(L/2\right)-R_{0}^{2}+R^{2}}-iR_{0}\right)}{\left(\left(L/2\right)^{3}-3C\left(L/2\right)^{2}-3R_{2}^{2}\left(L/2\right)+3\left(C^{2}+4R_{0}^{2}\right)\left(L/2\right)-12CR_{0}^{2}\right)\left(R-\left(L/2\right)\right)}\right)
\end{array}\right]\\
+8\ln\left(2\left(-\left(L/2\right)+R+\sqrt{\left(L/2\right)^{2}-2R\left(L/2\right)-R_{0}^{2}+R^{2}}\right)\right)+\\
\frac{1}{R_{0}^{3}}\left(\left(L/2\right)^{3}+3C\left(L/2\right)^{2}-3R_{2}^{2}\left(L/2\right)+3\left(C^{2}+4R_{0}^{2}\right)\left(L/2\right)+12CR_{0}^{2}\right)\\
\left[\begin{array}{l}
\tan^{-1}\left(\frac{R_{0}}{\sqrt{\left(L/2\right)^{2}+2R\left(L/2\right)-R_{0}^{2}+R^{2}}}\right)-\\
i\ln\left(\frac{2R_{0}^{2}\left(\sqrt{\left(L/2\right)^{2}+2R\left(L/2\right)-R_{0}^{2}+R^{2}}-iR_{0}\right)}{\left(\left(L/2\right)^{3}+3C\left(L/2\right)^{2}-3R_{2}^{2}\left(L/2\right)+3\left(C^{2}+4R_{0}^{2}\right)\left(L/2\right)+12CR_{0}^{2}\right)\left(R+\left(L/2\right)\right)}\right)
\end{array}\right]\\
-8\ln\left(2\left(\left(L/2\right)+R+\sqrt{\left(L/2\right)^{2}+2R\left(L/2\right)-R_{0}^{2}+R^{2}}\right)\right)+\\
\sqrt{\left(L/2\right)^{2}-2R\left(L/2\right)-R_{0}^{2}+R^{2}}\left[\begin{array}{l}
\frac{2\left(\left(\left(L/2\right)-C\right)^{2}-R_{2}^{2}\right)}{\left(\left(L/2\right)-R\right)^{3}}-\frac{R}{R_{0}^{2}}+\\
\frac{5R_{2}^{2}-5\left(L/2\right)^{2}-5C^{2}+6R_{0}^{2}+10\left(L/2\right)C}{R_{0}^{2}\left(\left(L/2\right)-R\right)}+\\
\frac{3C-2\left(L/2\right)}{R_{0}^{2}}+\frac{6\left(C-\left(L/2\right)\right)}{\left(\left(L/2\right)-R\right)^{2}}
\end{array}\right]
\end{array}\right\}\Bigg|_{C-R_{2}}^{C+R_{2}}
$$

$$E = \int_{C-R_2}^{C+R_2} E_p q\pi \frac{R}{C}\left[R_2^2 - (C-R)^2\right] dR$$

$$= -\frac{2\pi^2 q^2 \lambda}{C} \int_{C-R_2}^{C+R_2} \left[R_2^2 - (C-R)^2\right] dR \int_{R-L/2}^{R+L/2} \frac{r - \sqrt{r^2 - R_0^2}}{r^5} dr$$

$$= -\frac{2\pi^2 q^2 \lambda}{C} \int_{C-R_2}^{C+R_2} \left[R_2^2 - (C-R)^2\right] dR \left[\sqrt{r^2 - R_0^2}\left(\frac{1}{4r^4} - \frac{1}{8R_0^2 r^2}\right) + \frac{\tan^{-1}\left(\frac{R_0}{\sqrt{r^2 - R_0^2}}\right)}{8R_0^3} - \frac{1}{3r^3}\right]\Bigg|_{R-L/2}^{R+L/2}$$

$$= -\frac{2\pi^2 q^2 \lambda}{C} \int_{C-R_2}^{C+R_2} \left[R_2^2 - (C-R)^2\right] dR \left\{ \begin{array}{l} \left[\sqrt{(R+L/2)^2 - R_0^2}\left(\frac{1}{4(R+L/2)^4} - \frac{1}{8R_0^2 (R+L/2)^2}\right) + \frac{\tan^{-1}\left(\frac{R_0}{\sqrt{(R+L/2)^2 - R_0^2}}\right)}{8R_0^3} - \frac{1}{3(R+L/2)^3}\right] \\ -\left[\sqrt{(R-L/2)^2 - R_0^2}\left(\frac{1}{4(R-L/2)^4} - \frac{1}{8R_0^2 (R-L/2)^2}\right) + \frac{\tan^{-1}\left(\frac{R_0}{\sqrt{(R-L/2)^2 - R_0^2}}\right)}{8R_0^3} - \frac{1}{3(R-L/2)^3}\right] \end{array} \right\}$$

$$= -\frac{2\pi^2 q^2 \lambda}{C} \frac{1}{24} \left\{ \begin{array}{l} \frac{16(L/2)(3C-2R)}{(L/2)^2 - R^2} + \sqrt{(L/2)^2 + 2R(L/2) - R_0^2 + R^2} \left[\begin{array}{l} -\frac{6((L/2)+C)}{((L/2)+R)^2} + \frac{R}{R_0^2} + \frac{5R_2^2 - 5(L/2)^2 - 5C^2 + 6R_0^2 - 10(L/2)C}{R_0^2((L/2)+R)} \\ -\frac{2(L/2)+3C}{R_0^2} + \frac{2\left(((L/2)+C)^2 - R_2^2\right)}{((L/2)+R)^3} \end{array} \right] \\ + \frac{16(L/2)\left((R-2C)(L/2)^2 + (C^2 - R_2^2)R\right)}{\left((L/2)^2 - R^2\right)^2} + \frac{1}{R_0^3}\left(-(L/2)^3 + 3C(L/2)^2 + 3R_2^2(L/2) - 3(C^2 + 4R_0^2)(L/2) + 12CR_0^2\right) \\ \tan^{-1}\left(\frac{R_0}{\sqrt{(L/2)^2 - 2R(L/2) - R_0^2 + R^2}}\right) + \frac{R\left(-3R_2^2 + 3C^2 + R^2 - 3CR\right)\tan^{-1}\left(\frac{R_0}{\sqrt{(L/2)^2 - 2R(L/2) - R_0^2 + R^2}}\right)}{R_0^3} \\ -\frac{1}{R_0^3}\left((L/2)^3 + 3C(L/2)^2 - 3R_2^2(L/2) + 3(C^2 + 4R_0^2)(L/2) + 12CR_0^2\right)\tan^{-1}\left(\frac{R_0}{\sqrt{(L/2)^2 + 2R(L/2) - R_0^2 + R^2}}\right) \\ -\frac{R\left(-3R_2^2 + 3C^2 + R^2 - 3CR\right)\tan^{-1}\left(\frac{R_0}{\sqrt{(L/2)^2 + 2R(L/2) - R_0^2 + R^2}}\right)}{R_0^3} - 8\ln\left(16\left(R - (L/2)\right)\right) + 8\ln\left(-16\left(R + (L/2)\right)\right) \end{array} \right\}\Bigg|_{C-R_2}^{C+R_2}$$

REFERENCES

1. V. F. Puntes, K. M. Krishnan and A. P. Alivisatos, Science **291** (5511), 2115-2117 (2001).

2. A. M. Smith and S. M. Nie, Accounts Chem Res **43** (2), 190-200 (2010).

3. J. D. Bryan, S. A. Santangelo, S. C. Keveren and D. R. Gamelin, J Am Chem Soc **127** (44), 15568-15574 (2005).

4. A. B. K. Chen, S. G. Kim, Y. D. Wang, W. S. Tung and I. W. Chen, Nat Nanotechnol **6** (4), 237-241 (2011).

5. C. Subramaniam, T. S. Sreeprasad, T. Pradeep, G. V. P. Kumar, C. Narayana, T. Yajima, Y. Sugawara, H. Tanaka, T. Ogawa and J. Chakrabarti, Phys Rev Lett **99** (16) (2007).

6. G. Vicentini, L. B. Zinner, J. Zukerman-Schpector and K. Zinner, Coordin Chem Rev **196**, 353-382 (2000).

7. E. R. Eliel, K. A. H. Vanleeuwen and W. Hogervorst, Phys Rev A **22** (4), 1491-1499 (1980).

8. A. Mauger and C. Godart, Phys Rep **141** (2-3), 51-176 (1986).

9. S. J. Cho, Phys Lett A **A 29** (3), 129-& (1969).

10. P. Wachter, Phys Kondens Mater **7** (1), 1-+ (1968).

11. N. S. Vandamme, S. M. Richard and S. R. Winzer, J Am Ceram Soc **72** (8), 1409-1414 (1989).

12. B. M. Cheng, C. K. Duan and P. A. Tanner, Opt Mater **31** (6), 902-904 (2009).

13. T. Mirkovic, M. A. Hines, P. S. Nair and G. D. Scholes, Chem Mater **17** (13), 3451-3456 (2005).

14. M. L. Redigolo, D. S. Koktysh, S. J. Rosenthal, J. H. Dickerson, Z. Gai, L. Gao and J. Shen, Appl Phys Lett **89** (22) (2006).

15. A. Tanaka, H. Kamikubo, Y. Doi, Y. Hinatsu, M. Kataoka, T. Kawai and Y. Hasegawa, Chem Mater **22** (5), 1776-1781 (2010).

16. F. Zhao, H. L. Sun, G. Su and S. Gao, Small **2** (2), 244-248 (2006).

17. M. J. Bierman, K. M. Van Heuvelen, D. Schmeisser, T. C. Brunold and S. Jin, Adv Mater **19** (18), 2677-+ (2007).

18. W. Chen, X. H. Zhang and Y. N. Huang, Appl Phys Lett **76** (17), 2328-2330 (2000).

19. S. Thongchant, Y. Hasegawa, Y. Wada and S. Yanagida, J Phys Chem B **107** (10), 2193-2196 (2003).

20. S. Thongchant, Y. Hasegawa, K. Tanaka, K. Fujita, K. Hira, Y. Wada and S. Yanagida, Jpn J Appl Phys 2 **42** (7B), L876-L878 (2003).

21. M. L. Redigolo, D. S. Koktysh, K. van Benthem, S. J. Rosenthal and J. H. Dickerson, Mater Chem Phys **115** (2-3), 526-529 (2009).

22. I. N. Goncharenko and I. Mirebeau, Phys Rev Lett **80** (5), 1082-1085 (1998).

23. W. Heiss, G. Prechtl and G. Springholz, Phys Rev B **63** (16) (2001).

24. H. Kepa, G. Springholz, T. M. Giebultowicz, K. I. Goldman, C. F. Majkrzak, P. Kacman, J. Blinowski, S. Holl, H. Krenn and G. Bauer, Phys Rev B **68** (2) (2003).

25. N. S. Gaikwad, V. M. Nikale and C. H. Bhosale, J Phys Chem Solids **64** (5), 723-730 (2003).

26. E. Schierle, E. Weschke, A. Gottberg, W. Sollinger, W. Heiss, G. Springholz and G. Kaindl, Phys Rev Lett **101** (26) (2008).

27. B. Diaz, A. Malachias, P. H. O. Rappl, E. Abramof, V. A. Chitta and A. B. Henriques, J Cryst Growth **312** (19), 2828-2833 (2010).

28. W. Sollinger, W. Heiss, R. T. Lechner, K. Rumpf, P. Granitzer, H. Krenn and G. Springholz, Phys Rev B **81** (15) (2010).

29. A. B. Henriques, G. D. Galgano, E. Abramof, B. Diaz and P. H. O. Rappl, Appl Phys Lett **99** (9) (2011).

30. R. D. Robinson, B. Sadtler, D. O. Demchenko, C. K. Erdonmez, L. W. Wang and A. P. Alivisatos, Science **317** (5836), 355-358 (2007).

31. L. Vayssieres, Adv Mater **15** (5), 464-466 (2003).

32. W. Q. Han, S. S. Fan, Q. Q. Li and Y. D. Hu, Science **277** (5330), 1287-1289 (1997).

33. Y. Qiao, Y. Y. Lin, S. F. Zhang and J. B. Huang, Chem-Eur J **17** (18), 5180-5187 (2011).

34. F. Zhao and S. Gao, J Mater Chem **18** (9), 949-953 (2008).

35. F. Zhao, M. Yuan, W. Zhang and S. Gao, J Am Chem Soc **128** (36), 11758-11759 (2006).

36. L. Manna, D. J. Milliron, A. Meisel, E. C. Scher and A. P. Alivisatos, Nat Mater **2** (6), 382-385 (2003).

37. Y. Yin and A. P. Alivisatos, Nature **437** (7059), 664-670 (2005).

38. H. T. Liu, J. S. Owen and A. P. Alivisatos, J Am Chem Soc **129** (2), 305-312 (2007).

39. L. Dubau, C. Coutanceau, E. Garnier, J. M. Leger and C. Lamy, J Appl Electrochem **33** (5), 419-429 (2003).

40. D. C. Lee, T. Hanrath and B. A. Korgel, Angew Chem Int Edit **44** (23), 3573-3577 (2005).

41. J. E. Murphy, M. C. Beard, A. G. Norman, S. P. Ahrenkiel, J. C. Johnson, P. R. Yu, O. I. Micic, R. J. Ellingson and A. J. Nozik, J Am Chem Soc **128** (10), 3241-3247 (2006).

42. E. V. Shevchenko, D. V. Talapin, A. L. Rogach, A. Kornowski, M. Haase and H. Weller, J Am Chem Soc **124** (46), 13958-13958 (2002).

43. Y. D. Yin, C. K. Erdonmez, A. Cabot, S. Hughes and A. P. Alivisatos, Adv Funct Mater **16** (11), 1389-1399 (2006).

44. D. S. Koktysh, S. Somarajan, W. He, M. A. Harrison, S. A. McGill and J. H. Dickerson, Nanotechnology **21** (41) (2010).

45. B. K. Min and C. M. Friend, Chem Rev **107** (6), 2709-2724 (2007).

46. P. Raveendran, J. Fu and S. L. Wallen, J Am Chem Soc **125** (46), 13940-13941 (2003).

47. X. G. Peng, Chem-Eur J **8** (2), 335-339 (2002).

48. J. H. Yu, J. Joo, H. M. Park, S. I. Baik, Y. W. Kim, S. C. Kim and T. Hyeon, J Am Chem Soc **127** (15), 5662-5670 (2005).

49. I. Gur, N. A. Fromer and A. P. Alivisatos, J Phys Chem B **110** (50), 25543-25546 (2006).

50. P. Podsiadlo, S. Y. Choi, B. Shim, J. Lee, M. Cuddihy and N. A. Kotov, Biomacromolecules **6** (6), 2914-2918 (2005).

51. M. Y. Gao, J. Q. Sun, E. Dulkeith, N. Gaponik, U. Lemmer and J. Feldmann, Langmuir **18** (10), 4098-4102 (2002).

52. X. Wang, L. A. Xu, X. B. Xu, S. Chen and Y. J. Wang, Polym-Plast Technol **50** (5), 533-538 (2011).

53. A. Tao, F. Kim, C. Hess, J. Goldberger, R. R. He, Y. G. Sun, Y. N. Xia and P. D. Yang, Nano Lett **3** (9), 1229-1233 (2003).

54. P. Sarkar and P. S. Nicholson, J Am Ceram Soc **79** (8), 1987-2002 (1996).

55. O. O. Van der Biest and L. J. Vandeperre, Annu Rev Mater Sci **29**, 327-352 (1999).

56. W. D. He, A. Krejci, J. H. Lin, M. E. Osmulski and J. H. Dickerson, Nanoscale **3** (4), 1523-1525 (2011).

57. Gunthero.G, Phys Condens Matter **18** (1), 37-78 (1974).

58. W. D. Callister and D. G. Rethwisch, *Materials science and engineering : an introduction*, 8th ed. (John Wiley & Sons, Hoboken, NJ, 2010).

59. B. D. Cullity, *Introduction to magnetic materials*. (Addison-Wesley Pub. Co., Reading, Mass.,, 1972).

60. D. Jiles, *Introduction to magnetism and magnetic materials*, 1st ed. (Chapman and Hall, London ; New York, 1991).

61. B. D. Cullity and C. D. Graham, *Introduction to magnetic materials*, 2nd ed. (IEEE/Wiley, Hoboken, N.J., 2009).

62. R. K. Pathria, *Statistical mechanics*, 2nd ed. (Butterworth-Heinemann, Oxford ; Boston, 1996).

63. T. Kasuya, Ibm J Res Dev **14** (3), 214-& (1970).

64. R. P. Cowburn and M. E. Welland, Phys Rev B **58** (14), 9217-9226 (1998).

65. R. P. Cowburn, D. K. Koltsov, A. O. Adeyeye, M. E. Welland and D. M. Tricker, Phys Rev Lett **83** (5), 1042-1045 (1999).

66. C. Gilles, P. Bonville, H. Rakoto, J. M. Broto, K. K. W. Wong and S. Mann, J Magn Magn Mater **241** (2-3), 430-440 (2002).

67. M. Tamine, J Phys-Condens Mat **9** (14), 2915-2930 (1997).

68. C. Gilles, P. Bonville, K. K. W. Wong and S. Mann, Eur Phys J B **17** (3), 417-427 (2000).

69. J. A. Potton, G. J. Daniell and D. Melville, J Phys D Appl Phys **17** (8), 1567-1581 (1984).

70. S. H. Kilcoyne and R. Cywinski, J Magn Magn Mater **140**, 1466-1467 (1995).

71. P. Schwob and O. Vogt, Phys Lett **22** (4), 374-& (1966).

72. X. Y. Lang, Z. Wen and Q. Jiang, J Phys Chem C **112** (11), 4055-4060 (2008).

73. X. G. Wan, J. M. Dong and S. Y. Savrasov, Phys Rev B **83** (20) (2011).

74. M. A. El-Sayed, Accounts Chem Res **37** (5), 326-333 (2004).

75. J. Zhang, F. Huang and Z. Lin, Nanoscale **2** (1), 18-34 (2010).

76. S. V. Mahajan, S. A. Hasan, J. Cho, M. S. P. Shaffer, A. R. Boccaccini and J. H. Dickerson, Nanotechnology **19** (19) (2008).

77. S. V. Mahajan, D. W. Kavich, M. L. Redigolo and J. H. Dickerson, J Mater Sci **41** (24), 8160-8165 (2006).

78. S. Somarajan, S. A. Hasan, C. T. Adkins, E. Harth and J. H. Dickerson, J Phys Chem B **112** (1), 23-28 (2008).

79. M. N. Patel, R. D. Williams, R. A. May, H. Uchida, K. J. Stevenson and K. P. Johnston, Chem Mater **20** (19), 6029-6040 (2008).

80. Q. L. Zhang, T. Xu, D. Butterfield, M. J. Misner, D. Y. Ryu, T. Emrick and T. P. Russell, Nano Lett **5** (2), 357-361 (2005).

81. S. A. Hasan, J. L. Rigueur, R. R. Harl, A. J. Krejci, I. Gonzalo-Juan, B. R. Rogers and J. H. Dickerson, Acs Nano **4** (12), 7367-7372 (2010).

82. S. V. Mahajan and J. H. Dickerson, Nanotechnology **21** (14) (2010).

83. L. Y. Chen, H. Xing, Y. M. Shen, J. F. Bai and G. Q. Jiang, J Solid State Chem **182** (6), 1387-1395 (2009).

84. R. S. Selinsky, J. H. Han, E. A. M. Perez, I. A. Guzei and S. Jin, J Am Chem Soc **132** (45), 15997-16005 (2010).

85. Q. Y. Lu, F. Gao and S. Komarneni, Adv Mater **16** (18), 1629-+ (2004).

86. Y. Xu, N. Al-Salim, C. W. Bumby and R. D. Tilley, J Am Chem Soc **131** (44), 15990-+ (2009).

87. W. D. He, S. Somarajan, D. S. Koktysh and J. H. Dickerson, Nanoscale **3** (1), 184-187 (2011).

88. H. Reiss, J Appl Phys **39** (11), 5045-& (1968).

89. J. X. Gao, C. M. Bender and C. J. Murphy, Langmuir **19** (21), 9065-9070 (2003).

90. L. Manna, L. W. Wang, R. Cingolani and A. P. Alivisatos, J Phys Chem B **109** (13), 6183-6192 (2005).

91. J. M. Luther, H. M. Zheng, B. Sadtler and A. P. Alivisatos, J Am Chem Soc **131** (46), 16851-16857 (2009).

92. B. Sadtler, D. O. Demchenko, H. Zheng, S. M. Hughes, M. G. Merkle, U. Dahmen, L. W. Wang and A. P. Alivisatos, J Am Chem Soc **131** (14), 5285-5293 (2009).

93. J. S. Owen, J. Park, P. E. Trudeau and A. P. Alivisatos, J Am Chem Soc **130** (37), 12279-+ (2008).

94. S. Kumar, K. S. Gandhi and R. Kumar, Ind Eng Chem Res **46** (10), 3128-3136 (2007).

95. F. Huang, H. Z. Zhang and J. F. Banfield, Nano Lett **3** (3), 373-378 (2003).

96. H. Yan, S. Cingarapu, K. J. Klabunde, A. Chakrabarti and C. M. Sorensen, Phys Rev Lett **102** (9) (2009).

97. D. K. Smith and B. A. Korgel, Langmuir **24** (3), 644-649 (2008).

98. J. Perez-Juste, L. M. Liz-Marzan, S. Carnie, D. Y. C. Chan and P. Mulvaney, Adv Funct Mater **14** (6), 571-579 (2004).

99. T. Wetz, K. Soulantica, A. Talqui, M. Respaud, E. Snoeck and B. Chaudret, Angew Chem Int Edit **46** (37), 7079-7081 (2007).

100. M. Matsubara, A. Schmehl, J. Mannhart, D. G. Schlom and M. Fiebig, Phys Rev B **81** (21) (2010).

101. Y. H. Wang, W. Wei, D. Maspoch, J. S. Wu, V. P. Dravid and C. A. Mirkin, Nano Lett **8** (11), 3761-3765 (2008).

102. Y. Hasegawa, T. A. Adachi, A. Tanaka, M. Afzaal, P. O'Brien, T. Doi, Y. Hinatsu, K. Fujita, K. Tanaka and T. Kawai, J Am Chem Soc **130** (17), 5710-5715 (2008).

103. R. L. Penn, K. Tanaka and J. Erbs, J Cryst Growth **309** (1), 97-102 (2007).

104. E. V. Shevchenko, D. V. Talapin, N. A. Kotov, S. O'Brien and C. B. Murray, Nature **439** (7072), 55-59 (2006).

105. R. L. Penn, J Phys Chem B **108** (34), 12707-12712 (2004).

106. N. Pradhan, H. F. Xu and X. G. Peng, Nano Lett **6** (4), 720-724 (2006).

107. J. F. Banfield, S. A. Welch, H. Z. Zhang, T. T. Ebert and R. L. Penn, Science **289** (5480), 751-754 (2000).

108. R. L. Penn and J. F. Banfield, Science **281** (5379), 969-971 (1998).

109. W. D. He and J. H. Dickerson, Appl Phys Lett **98** (8) (2011).

110. K. S. Cho, D. V. Talapin, W. Gaschler and C. B. Murray, J Am Chem Soc **127** (19), 7140-7147 (2005).

111. R. D. Gunning, C. O'Sullivan and K. M. Ryan, Phys Chem Chem Phys **12** (39), 12430-12435 (2010).

112. D. V. Talapin, E. V. Shevchenko, C. B. Murray, A. V. Titov and P. Kral, Nano Lett **7** (5), 1213-1219 (2007).

113. E. J. H. Lee, C. Ribeiro, E. Longo and E. R. Leite, J Phys Chem B **109** (44), 20842-20846 (2005).

114. M. Ethayaraja and R. Bandyopadhyaya, Langmuir **23** (11), 6418-6423 (2007).

115. C. O'Sullivan, R. D. Gunning, A. Sanyal, C. A. Barrett, H. Geaney, F. R. Laffir, S. Ahmed and K. M. Ryan, J Am Chem Soc **131** (34), 12250-12257 (2009).

116. X. L. Li, L. Zhang, X. R. Wang, I. Shimoyama, X. M. Sun, W. S. Seo and H. J. Dai, J Am Chem Soc **129** (16), 4890-+ (2007).

117. D. Y. Xia and S. R. J. Brueck, Nano Lett **4** (7), 1295-1299 (2004).

118. S. A. Hasan, D. W. Kavich and J. H. Dickerson, Chem Commun (25), 3723-3725 (2009).

119. S. A. Hasan, D. W. Kavich, S. V. Mahajan and J. H. Dickerson, Thin Solid Films **517** (8), 2665-2669 (2009).

120. M. A. Islam, Y. Q. Xia, D. A. Telesca, M. L. Steigerwald and I. P. Herman, Chem Mater **16** (1), 49-54 (2004).

121. A. L. Rogach, N. A. Kotov, D. S. Koktysh, J. W. Ostrander and G. A. Ragoisha, Chem Mater **12** (9), 2721-2726 (2000).

122. S. V. Mahajan and J. H. Dickerson, Appl Phys Lett **96** (11) (2010).

123. A. J. Krejci, I. Gonzalo-Juan and J. H. Dickerson, Acs Appl Mater Inter **3** (9), 3611-3615 (2011).

124. H. He, W. P. Cai, Y. X. Lin and Z. F. Dai, Langmuir **27** (5), 1551-1555 (2011).

125. S. K. Yang, W. P. Cai, H. W. Zhang, X. X. Xu and H. B. Zeng, J Phys Chem C **113** (44), 19091-19095 (2009).

126. N. Chandrasekharan and P. V. Kamat, Nano Lett **1** (2), 67-70 (2001).

127. N. Saleh, H. J. Kim, T. Phenrat, K. Matyjaszewski, R. D. Tilton and G. V. Lowry, Environ Sci Technol **42** (9), 3349-3355 (2008).

128. S. J. Limmer and G. Z. Cao, Adv Mater **15** (5), 427-431 (2003).